Victorino Franco
Brad Dodrill *Editors*

Magnetic Measurement Techniques for Materials Characterization

Springer

Magnetic Measurement Techniques for Materials Characterization

December 26, 2020

Contents

Chapter 1

Neutron Scattering in Magnetism: Fundamentals and Examples

Javier Campo and Victor Laliena

Aragón Nanoscience and Materials Institute, Spanish National Research Council (CSIC) - University of Zaragoza, C/Pedro Cerbuna 12, 50009 Zaragoza, Spain

Abstract. In this chapter, an up-to-date survey of theoretical concepts and experimental results in the field of the neutron scattering techniques applied to magnetism, and their relevance to experiments in real materials, is presented. Main emphasis of the chapter is to enlarge the use of these techniques among the researchers (physicist, chemists, engineers, etc...) in the area of magnetism and magnetic materials. For that reason we do not enter deeply in topics as, neutron production, neutron optics, detectors, instrumentation, etc... but, we focused the chapter on the neutron scattering applications in such a field.

Along this chapter, together with some basic concept on, quantum mechanics, solid state physics, magnetism, and symmetry, we introduce the main theoretical concepts, peculiarities, and language, of the neutron scattering techniques, and we particularize it to the crystalline matter. In a second part, we briefly introduce the most commonly employed techniques (powder diffraction, single crystal diffraction, polarization analysis, inelastic, SANS, reflectivity, etc...) and how these techniques are applied to understand different magnetic phenomena and magnetic materials, trying to cover a large variety of topics with interest in magnetism. Every time, the examples showed here, show how neutrons can enlighten problems that are quasi impossible to be solved with other techniques.

Victorino Franco and Brad Dodrill (Ed.)
Magnetic Measurement Techniques for Materials Characterization

1.1 Introduction

Since the fifties, when the first experiments using neutrons beams were reported, the neutron scattering techniques are of paramount importance in the study of any type of magnetism and magnetic materials. It is due to the fact that the neutron carries a spin, and therefore a magnetic moment, that can interact, via the dipolar magnetic interaction, with the different sources of magnetism in the matter (unpaired electrons, magnetic nuclei, etc...). In this chapter, it is not intended to deduce from the scattering theory all the equations governing the scattering, magnetic or nuclear, of neutrons by matter, but only the mathematical expressions, and their approximations, necessary to understand the experiments are described.

Different sets of *canonical* experiments, related to different neutron scattering techniques, will be explained bearing in mind that the goal of the chapter is to motivate the readers by showing how the neutron techniques can help in their scientific problems in the area of magnetism.

The chapter is organized as follows. In section (1.2) the fundamentals of thermal neutron scattering theory will be explained, giving only the minimal information to understand the meaning of the formulae and the approximations employed to obtain them. In section (1.3) the scattering theory will be particularized for crystalline matter and in section (1.4) a brief deduction of the scattering of polarized neutrons is given.

In section (1.5) the concepts of magnetic space groups and the formalism of the propagation vector to describe magnetic structures is introduced. Then the powder diffraction techniques, explaining a little bit the Rietveld method, is presented in section (1.6). Applications of single crystal neutron diffraction with unpolarized neutrons are explained in (1.7). In sections (1.8) and (1.9) the use of polarized neutrons in single crystals, by exploring the potentiality of Blume-Maleev equations, is highlighted. The Small Angle Neutron Scattering (SANS) techniques are also often employed to solve important problems in magnetism; physics of magnetic nanoparticles, magnetic clusters, skyrmions, etc... In section (1.10) examples of the use of these techniques in cubic helimagnets to characterize skyrmionic phases will be shown. Some ideas of magnetic inelastic scattering are described in section (1.11) and finally other neutron scattering techniques (Neutron Spin Echo, Neutron Reflectivity and Quasielastic Neutron Scattering), initially developed to study soft matter and that now are more and more employed in magnetism, will be explained in section (1.12).

An introduction to the application of neutron techniques to magnetic materials, with a focus on the physics behind the instrumentation and general data analysis for SANS, reflectivity, and diffraction, has been described in the previous chapter.

The chosen examples in this chapter comprise several materials showing different magnetic behaviors; spin glasses, cubic helimagnets, skyrmions,

Random Fields, solitons, single molecule magnets, organic magnets, multiferroics, battery electrodes, molecular rotors, etc...

Before starting, let us describe briefly the conventions used in this chapter. Although in general it is uncommon in physical literature, we found it convenient to adhere to the crystallographic and spectroscopy conventions, and define the wave number as the inverse of the wavelength and the frequency as the inverse of time period, without the 2π factors that are present in the more common convention. As a drawback, the 2π factors appear in the exponential factors of the Fourier transforms, but they disappear from many expressions, as for instance from the normalization factors of the Fourier transform. The symbol h denotes the Planck constant[1], $h \approx 6.626 \times 10^{-34}$ Js, and, as usual, $\hbar = h/2\pi$. Energy and momentum are related to frequency and wave number by $E = h\nu$ and $p = hk$, respectively.

1.2 Fundamentals of Neutron Scattering

1.2.1 Properties of neutrons

The neutron is a baryon, an elementary particle formed by three quarks bound by the strong interaction. Its mass, $m = 1.67{\times}10^{-27}$ kg $= 939.6$ MeV/c^2, is almost equal to the proton mass, and it has an intrinsic angular momentum, or spin, of magnitude $\hbar/2$. The neutrons are thus fermions and obey the Fermi-Dirac statistics. Neutrons are stable within the nuclei, but free neutrons are unstable, decaying via the weak interaction into a proton, an electron, and an antineutrino, with a mean life of $\sim$881 s. Although it is a neutral particle, its constituent quarks are charged and thus the neutron interacts electromagnetically. Its dipolar electric moment does vanish, or, if it does not, it is extremely small: at the time of writing, the latest experimental result is quoted as $(0.0 \pm 1.1_{\rm stat} \pm 0.2_{\rm sys}) \times 10^{-26}\ |e| \cdot$ cm, where the subscripts *stat* and *sys* stand for the statistical and systematic contributions to the uncertainty, and $e < 0$ is the electron charge [1]. Therefore, the electromagnetic interactions of neutrons are dominated by its dipolar magnetic moment, described by the quantum operator

$$\vec{\mu}_{\rm n} = -\gamma \mu_{\rm N} \frac{1}{2} \vec{\sigma}, \tag{1.1}$$

where $\mu_{\rm N} \approx 5.05 \times 10^{-27}$J/T is the nuclear magneton, $\gamma = 3.826$ is the neutron *g-factor*, and $\vec{\sigma}$ are the Pauli matrices acting on the neutron spin space.

Neutrons are produced in nuclear reactions and as a product of the fission of heavy nucleus, such ^{252}Cf, ^{235}U, etc... It is difficult to have intense

[1] Occasionally, the symbol h will be used to denote one of the Miller indices, but the context will resolve any ambiguity

neutron sources. At present, such intense sources are of two types: *nuclear reactors*, in which the neutrons are a by-product of the fission of the nuclear fuel, and *spallation sources*, in which neutrons are produced when a beam of high energy protons, accelerated by linear accelerators (LINAC), impacts on a heavy metal target.

According to their energy, in meV, neutrons are customarily classified into cold (0.1–10), thermal (10–100), hot (100–500), and epithermal (>500). The rest energy of the neutron is many orders of magnitude higher than the kinetic energy of these kind of neutrons, which are thus non-relativistic particles, with energy given by $E = h^2k^2/2m$, where $k = 1/\lambda$ is the wave-number and λ the wavelength. This has a very interesting consequence for the study of condensed matter systems, since the wavelength of neutrons with energy of the order of meV, which correspond to the excitation energies of many systems, is in the range of the Å, which corresponds to the inter-particle distances in the systems. In comparison, the energy of the X-rays with such wavelengths is in the range of the keV, orders of magnitude higher than the excitation energies of condensed matter systems.

Being a spin 1/2 particle, the quantum state of a free neutron is completely characterized by the three components of its wave-vector, $\vec{k}$, which form a continuous set, and a two component spinor which characterizes the spin state, or *polarization state* of the neutron, denoted by $|\sigma\rangle$. Each spinor is the eigenstate of the projection of the spin operator $\vec{\sigma}$ onto the direction determined by the expectation value of the spin operator in this polarization state, $\langle\sigma|\,\vec{\sigma}\,|\sigma\rangle$, which is a unit vector. The polarization state of the neutron is completely characterized by this unit vector which is called the polarization vector of the neutron. In a beam, different neutrons may be in different polarization states. The polarization vector of the beam, $\vec{P}$, is defined as the average of the polarization vectors of all neutrons. Oviously, its modulus satisfies $P \leq 1$. The polarization states of the beam is statistically described by a 2×2 *density matrix* operator,

$$\varrho = \frac{1}{N} \sum_n |\sigma_n\rangle \langle\sigma_n| \,, \tag{1.2}$$

where n labels the neutrons in the beam, N is the number of neutrons, and $|\sigma_n\rangle$ stands for the normalized spin wave function (spinor) of the n-th neutron. The density matrix is hermitian and satisfies $\mathrm{Tr}\,\varrho = 1$ and $\mathrm{Tr}(\varrho\vec{\sigma}) = \vec{P}$. The only 2×2 hermitian matrix that satisfies the two conditions is

$$\varrho = \frac{1}{2}\left(\mathrm{I}_2 + \vec{P}\cdot\vec{\sigma}\right), \tag{1.3}$$

where I_2 is the two dimensional unit matrix. The probability of finding a neutron of the beam in some arbitrary polarization state, $|\sigma\rangle$, is given by the expectation value of the density matrix in this state, $\langle\sigma|\,\varrho\,|\sigma\rangle$, as can be readily checked. Notice that the expectation values on *all* possible states,

$|\sigma\rangle$, fully determines the density matrix. The eigenvectors of ϱ are those of $\vec{P}\cdot\vec{\sigma}$, and its two eigenvalues are given by $(1\pm P)/2$. A beam with $\vec{P}=0$ is called an *unpolarized* beam. In it, all polarization states have the same probability.

Notice finally that an orthonormal basis on the neutron spin space is always associated to a given direction, defined by some unit vector $\hat{u}$. Therefore, if the first vector of the basis is the eigenvector of $\hat{u}\cdot\vec{\sigma}$ with positive eigenvalue, the second vector is the eigenvector with negative eigenvalue. Hence, choosing an orthonormal basis in spin space is tantamount to choosing a *quantization* axis, and the vectors of the basis are the eigenstates of the projection of the spin operator onto the quantization axis. If we choose the quantization axis along the beam polarization direction, the vectors of the basis are the eigenstates of the density matrix.

1.2.2 The scattering problem

In a scattering experiment a probe, in our case a neutron beam, impinges a target and the resulting scattered beam is detected at a large distance from the target. The spatial and energy distributions of the scattered neutrons provides a considerable amount of physical information about the target. The incoming neutron is described by a plane wave with wave-vector $\vec{k}_i$ and a spin state $|\sigma_i\rangle$, which is one of the eigenstates of the incident beam density matrix, ϱ_i. If the beam is unpolarized, any orthonormal basis in spin space can be taken. If the state of target before the interaction is $|\varphi_i\rangle$, the initial state of the composite neutron-target system is written as $|\vec{k}_i\sigma_i;\varphi_i\rangle$. A long time after the scattering took place there will be a certain probability that the composite system is found in the state $|\vec{k}_f\sigma_f;\varphi_f\rangle$. The spin state of the scattered neutron can be referred to a quantization axis different from that of the incoming beam, that is, the orthonormal basis $\{|\sigma_f\rangle\}$, need not be the same as the orthonormal basis $\{|\sigma_i\rangle\}$.

In the scattering experiment the initial neutron beam is prepared according to some convenient specification and the scattered neutrons are detected by detectors conveniently distributed around the target. The *differential scattering cross section* is defined as the number of neutrons scattered in the direction $\hat{k}_f$ per unit time, solid angle, $d\Omega_{\hat{k}_f}$, and energy, dE_f, normalized by the neutron flux, which is the number of incident neutrons per unit of time and beam cross section area [2]. If $\mathcal{H}_{\rm int}$ is the interaction Hamiltonian operator for the neutron and the target system, the differential scattering cross section in the lowest order pertubation theory is given by

$$\left(\frac{d^2\sigma}{d\Omega_{\hat{k}_f}dE_f}\right)_{\sigma_f}=\frac{k_f}{k_i}\left(\frac{2\pi m}{h^2}\right)^2|\,\langle\vec{k}_f\sigma_f;\varphi_f|\,\mathcal{H}_{\rm int}\,|\vec{k}_i\sigma_i;\varphi_i\rangle\,|^2\delta(E_{\varphi_i}-E_{\varphi_f}+h\nu), \tag{1.4}$$

where E_{φ_i} and E_{φ_f} are the energies of the target before and after the interaction, and $h\nu = E_i - E_f$ is the difference between the energies of the incident and scattered neutron. Although the above formula cannot be rigorously derived in a few lines, since it requires the application of scattering theory [2], the origins of each ingredient entering (1.4) can be easily understood. The Dirac delta function, δ, enforces the conservation of energy in the whole neutron-target system a long time after the interaction took place, when the interaction energy is negligible. The matrix element of $\mathcal{H}_{\rm int}$ is the lowest order perturbation theory approximation to the probability amplitude that the composite neutron-target system is found in the state $|\vec{k}_f\sigma_f;\varphi_f\rangle$ after the interaction took place. Its modulus squared divided by h gives the probability per unit time of finding this final state (compare for instance with the *Fermi Golden rule* [3]). The density of final neutron states (per unit energy and per unit solid angle) is mk_f/h^2, what accounts for the k_f factor and one m/h^2 factor. And the incident neutron flux is proportional to the neutron velocity, hk_i/m, what introduces the k_i in the denominator and another m/h factor.

The initial target pure state, $|\varphi_i\rangle$, is unknown. It is assumed that the target is in equilibrium, so that its quantum state is actually mixed, given by the density matrix corresponding to the Boltzmann distribution. This means that we have to average the right hand side of expression (1.4) over the initial target states, $|\varphi_i\rangle$, with the Boltzmann weight $P_{\varphi_i} = \exp(-E_{\varphi_i}/k_{\rm B}T)/\mathcal{Z}$, where T is the temperature, $k_{\rm B}$ the Boltzmann constant, and $\mathcal{Z}$ the canonical partition function that ensures the normalization $\sum_{\varphi_i} P_{\varphi_i} = 1$. The final state of the target, $|\varphi_f\rangle$, is not observed, so that we have to sum over all of them. Analogously, we have to average over the polarization state of the incident neutron, $|\sigma_i\rangle$, which has a probability $p_{\sigma_i} = \langle\sigma_i|\,\varrho_i\,|\sigma_i\rangle$, and, if the polarization state of the scattered neutron is not observed, we have to sum over $|\sigma_f\rangle$. To be general, we assume here that it is observed. Finally, there are properties of the target that influence the scattering result that are usually not under control. An example is the isotopic distribution of the nuclei. These properties have to be treated as a disorder and we have to average over them with the proper disorder distribution. We denote this average by a horizontal bar over the quantities that are averaged. Taking all this into account, (1.4) becomes

$$\left(\frac{d^2\sigma}{d\Omega_{\hat{k}_f}dE_f}\right)_{\sigma_f} = \frac{k_f}{k_i}\left(\frac{2\pi m}{h^2}\right)^2 \times \sum_{\sigma_i\varphi_i\varphi_f} p_{\sigma_i}P_{\varphi_i}\overline{|\langle\vec{k}_f\sigma_f;\varphi_f|\,\mathcal{H}_{\rm int}\,|\vec{k}_i\sigma_i;\varphi_i\rangle|^2}\delta(E_{\varphi_i}-E_{\varphi_f}+h\nu). \tag{1.5}$$

Neutron interactions at low energy do not depend on neutron momentum. Hence, the interaction Hamiltonian contains no derivative with respect to the neutron coordinates. Since the neutron wave functions are

plane waves, the matrix elements entering the cross section can be partially evaluated as

$$\langle \vec{k}_f \sigma_f; \varphi_f | \, \mathcal{H}_{\rm int} \, | \vec{k}_i \sigma_i; \varphi_i \rangle = \int d^3 r \, \mathrm{e}^{\mathrm{i}2\pi \vec{q}\cdot\vec{r}} \, \langle \sigma_f | \, \langle \varphi_f | \, \mathcal{H}_{\rm int}(\vec{r}; \ldots) \, | \varphi_i \rangle \, | \sigma_i \rangle \,, \quad (1.6)$$

where $\vec{r}$ is the neutron position, and the ellipsis stand for the target degrees of freedom on which the interaction hamiltonian depends: the position and momentum operators of the i-th target particle, $\vec{r}_i$ and $\vec{p}_i$, respectively, and any other operators, like the spin of the i-the particle, I_i. We have introduced the *scattering vector*, $\vec{q} = \vec{k}_i - \vec{k}_f$, which is proportional to the momentum transfer vector.

It is convenient to define the *amplitude* operator

$$\mathcal{A}_{\vec{q}} = \frac{2\pi m}{h^2} \int d^3 r \, \mathrm{e}^{\mathrm{i}2\pi \vec{q}\cdot\vec{r}} \, \mathcal{H}_{\rm int}(\vec{r}; \vec{r}_1 \vec{p}_1 I_1; \ldots, \vec{r}_{N_{\rm P}} \vec{p}_{N_{\rm P}} I_{N_{\rm P}}), \quad (1.7)$$

which is a matrix in the neutron spin degrees of freedom and an operator in the Hilbert space of the target. It has the dimensions of a length. In terms of $\mathcal{A}_{\vec{q}}$, the cross section reads:

$$\left(\frac{d^2\sigma}{d\Omega_{\hat{k}_f} dE_f} \right)_{\sigma_f} = \frac{k_f}{k_i} \sum_{\sigma_i \varphi_i \varphi_f} p_{\sigma_i} P_{\varphi_i} \times \overline{\langle \varphi_i | \, \langle \sigma_i | \, \mathcal{A}^\dagger_{\vec{q}} | \sigma_f \rangle \, | \varphi_f \rangle \, \langle \varphi_f | \, \langle \sigma_f | \, \mathcal{A}_{\vec{q}} \, | \sigma_i \rangle \, | \varphi_i \rangle \, \delta(E_{\varphi_i} - E_{\varphi_f} + h\nu)} \,. \quad (1.8)$$

We can write an interesting expression for the cross section by inserting in (1.8) the Fourier representation of the Dirac delta function

$$\delta(E_{\varphi_i} - E_{\varphi_f} + h\nu) = \frac{1}{h} \int_{-\infty}^{\infty} dt \; \mathrm{e}^{-\mathrm{i}2\pi (E_{\varphi_i} - E_{\varphi_f} + h\nu)t/h}, \quad (1.9)$$

and using the relations $\mathrm{e}^{-\mathrm{i}E_{\varphi_i} t/\hbar} \, |\varphi_i\rangle = \mathcal{U}(t) \, |\varphi_i\rangle$, $\langle \varphi_f | \, \mathrm{e}^{\mathrm{i}E_{\varphi_f} t/\hbar} = \langle \varphi_f | \, \mathcal{U}^\dagger(t)$, and

$$\mathcal{U}^\dagger(t) \, \mathcal{A}_{\vec{q}} \, \mathcal{U}(t) = \mathcal{A}_{\vec{q}}(t), \quad (1.10)$$

where $\mathcal{U}(t)$ is the time evolution operator of the target in the Schrödinger picture and $\mathcal{A}_{\vec{q}}(t)$ is the Heisenberg operator that coincides with $\mathcal{A}_{\vec{q}}$ at $t = 0$. Using the notation $\langle \mathcal{O} \rangle$ for the thermal quantum average of any operator $\mathcal{O}$,

$$\langle \mathcal{O} \rangle = \sum_{\varphi} P_\varphi \, \langle \varphi | \, \mathcal{O} \, | \varphi \rangle \,, \quad (1.11)$$

we get

$$\left(\frac{d^2\sigma}{d\Omega_{\hat{k}_f} dE_f} \right)_{\sigma_f} = \frac{k_f}{k_i} \int_{-\infty}^{\infty} \frac{dt}{h} \mathrm{e}^{-\mathrm{i}2\pi\nu t} \sum_{\sigma_i} p_{\sigma_i} \overline{\left\langle \langle \sigma_i | \, \mathcal{A}^\dagger_{\vec{q}}(0) \, | \sigma_f \rangle \, \langle \sigma_f | \, \mathcal{A}_{\vec{q}}(t) \, | \sigma_i \rangle \right\rangle}. \quad (1.12)$$

The sum over σ_i gives the density matrix of the incident beam, ϱ_i, so that the above equation can be written as

$$\left(\frac{d^2\sigma}{d\Omega_{\hat{k}_f} dE_f}\right)_{\sigma_f} = \frac{k_f}{k_i} \int_{-\infty}^{\infty} \frac{dt}{h} \mathrm{e}^{-\mathrm{i}2\pi\nu t} \,\mathrm{Tr}\, \overline{\left\langle \mathcal{A}^\dagger_{\vec{q}}(0)\, \mathcal{P}_{\sigma_f}\, \mathcal{A}_{\vec{q}}(t)\, \varrho_i \right\rangle}, \tag{1.13}$$

where $\mathcal{P}_{\sigma_f} = |\sigma_f\rangle \langle\sigma_f|$ is the projector onto the neutron final spin state, and Tr stands for the trace in neutron spin space.

We see that the cross section contains a big amount of information about the target. The interaction Hamiltonian and $\mathcal{A}_{\vec{q}}$ depend on the degrees of freedom (coordinates, spin, etc.) of the target particles. Equation (1.13) shows that the scattering cross section is related to the Fourier transform of the time correlation function of the target degrees of freedom involved in the interaction with the neutron.

We find it convenient to use the following notation for the Fourier transform of the time correlation function of two operators A and B acting on the target Hilbert space:

$$\langle AB \rangle_\nu = \int_{-\infty}^{\infty} \frac{dt}{h} \mathrm{e}^{-\mathrm{i}2\pi\nu t} \langle A(0)B(t)\rangle \,, \tag{1.14}$$

so that we have the compact expression:

$$\left(\frac{d^2\sigma}{d\Omega_{\hat{k}_f} dE_f}\right)_{\sigma_f} = \frac{k_f}{k_i} \,\mathrm{Tr}\, \overline{\left\langle \mathcal{A}^\dagger_{\vec{q}} \mathcal{P}_{\sigma_f}\, \mathcal{A}_{\vec{q}}\, \varrho_i \right\rangle}_\nu. \tag{1.15}$$

The sum over a complete set of orthonormal final polarization states gives the intensity of the scattered beam, relative to that of the incoming beam, propagating along $\hat{k}_f$ with energy between E_f and $E_f + dE_f$. Taking into account that $\sum_{\sigma_f} \mathcal{P}_{\sigma_f} = \mathrm{I}_2$, this intensity is given by

$$I_{\vec{q}\nu} = \frac{k_f}{k_i} \,\mathrm{Tr}\, \overline{\left\langle \mathcal{A}^\dagger_{\vec{q}} \mathcal{A}_{\vec{q}}\, \varrho_i \right\rangle}_\nu. \tag{1.16}$$

The density matrix of the scattered beam, ϱ_f, can be obtained from equation (1.12), and from it the polarization vector of the scattered beam, which is given by

$$\vec{P}_f = \frac{1}{I_{\vec{q}\nu}} \,\mathrm{Tr}\, \overline{\left\langle \mathcal{A}^\dagger_{\vec{q}} \vec{\sigma}\, \mathcal{A}_{\vec{q}}\, \varrho_i \right\rangle}_\nu. \tag{1.17}$$

For $t \to \infty$ the correlation between two operators disappears, and we have

$$\lim_{t\to\infty} \langle \mathbb{A}(0)\mathbb{B}(t)\rangle = \lim_{t\to\infty} \langle \mathbb{A}(0)\rangle \langle \mathbb{B}(t)\rangle = \langle \mathbb{A}\rangle \langle \mathbb{B}\rangle \,, \tag{1.18}$$

where we used the invariance of the system under time translation and the fact the Heisenberg operators coincide with the Schrödinger operators at

$t = 0$. If the product $\langle \mathbb{A} \rangle \langle \mathbb{B} \rangle$ does not vanish, then $\langle \mathbb{A}\mathbb{B} \rangle_\nu$ is singular, since the integrand of the right-hand-side of (1.14) does not vanish for $t \to \infty$. We may isolate the singularity by substracting $\langle \mathbb{A} \rangle \langle \mathbb{B} \rangle$ from the integrand, what makes the integral convergent (non-singular), and adding the remaining part, which is

$$\int_{-\infty}^{\infty} \frac{dt}{h} \mathrm{e}^{-\mathrm{i}2\pi\nu t} \langle \mathbb{A} \rangle \langle \mathbb{B} \rangle = \delta(h\nu) \langle \mathbb{A} \rangle \langle \mathbb{B} \rangle , \tag{1.19}$$

so that we have

$$\langle \mathbb{A}\mathbb{B} \rangle_\nu = \int_{-\infty}^{\infty} \frac{dt}{h} \mathrm{e}^{-\mathrm{i}2\pi\nu t} \left[\langle \mathbb{A}(0)\mathbb{B}(t) \rangle - \langle \mathbb{A} \rangle \langle \mathbb{B} \rangle \right] + \delta(h\nu) \langle \mathbb{A} \rangle \langle \mathbb{B} \rangle . \tag{1.20}$$

Applying equation (1.20) to (1.15), we separate the scattering into *elastic* and *inelastic*:

$$\left(\frac{d^2\sigma}{d\Omega_{\hat{k}_f} dE_f} \right)_{\sigma_f} = \left(\frac{d^2\sigma^{(\mathrm{e})}}{d\Omega_{\hat{k}_f} dE_f} \right)_{\sigma_f} + \left(\frac{d^2\sigma^{(\mathrm{i})}}{d\Omega_{\hat{k}_f} dE_f} \right)_{\sigma_f} \tag{1.21}$$

where

$$\left(\frac{d^2\sigma^{(\mathrm{e})}}{d\Omega_{\hat{k}_f} dE_f} \right)_{\sigma_f} = \delta(E_i - E_f) \langle \sigma_f | \overline{\langle \mathcal{A}_{\vec{q}} \rangle \, \varrho_i \, \langle \mathcal{A}^\dagger_{\vec{q}} \rangle} \, | \sigma_f \rangle . \tag{1.22}$$

is the *elastic scattering cross section* and

$$\left(\frac{d^2\sigma^{(\mathrm{i})}}{d\Omega_{\hat{k}_f} dE_f} \right)_{\sigma_f} = \frac{k_f}{k_i} \, \mathrm{Tr} \, \overline{\left\langle (\mathcal{A}^\dagger_{\vec{q}} - \langle \mathcal{A}^\dagger_{\vec{q}} \rangle) \mathcal{P}_{\sigma_f} \, (\mathcal{A}_{\vec{q}} - \langle \mathcal{A}_{\vec{q}} \rangle) \, \varrho_i \right\rangle_\nu} . \tag{1.23}$$

is the *inelastic scattering cross section*. We used the properties of the trace operation to write the elastic cross section in the form of equation (1.22).

It is customary to present the integrated elastic cross section by integrating (1.22) over dE_f:

$$\left(\frac{d\sigma^{(\mathrm{e})}}{d\Omega_{\hat{k}_f}} \right)_{\sigma_f} = \langle \sigma_f | \overline{\langle \mathcal{A}_{\vec{q}} \rangle \, \varrho_i \, \langle \mathcal{A}^\dagger_{\vec{q}} \rangle} \, | \sigma_f \rangle . \tag{1.24}$$

One has to bear in mind that $k_f = k_i$ in the above equation.

The probability of finding a neutron in the scattered beam with polarization state σ_f is given by $\langle \sigma_f | \, \varrho_f \, | \sigma_f \rangle$, where ϱ_f is the spin density matrix of the scattered beam. From equation (1.24) we see that for the elastic scattered beam ϱ_f is given by

$$\varrho_f = \frac{1}{I_{\vec{q}}} \overline{\langle \mathcal{A}_{\vec{q}} \rangle \varrho_i \langle \mathcal{A}^\dagger_{\vec{q}} \rangle}, \tag{1.25}$$

where

$$I_{\vec{q}} = \sum_{\sigma_f} \langle \sigma_f | \, \overline{\langle \mathcal{A}_{\vec{q}} \rangle \, \varrho_i \, \langle \mathcal{A}^\dagger_{\vec{q}'} \rangle} \, | \sigma_f \rangle \tag{1.26}$$

is proportional to the intensity of the elastically scattered beam in the $\hat{k}_f$ direction. Therefore, the polarization vector of the elastically scattered beam is given by

$$\vec{P}_f = \frac{1}{I_{\vec{q}}} \, \mathrm{Tr} \left(\overline{\langle \mathcal{A}_{\vec{q}} \rangle \varrho_i \langle \mathcal{A}^\dagger_{\vec{q}'} \rangle} \, \vec{\sigma} \right). \tag{1.27}$$

Let us stress that ϱ_f and $\vec{P}_f$ depend on the direction at which the scattered beam is observed, given by $\hat{k}_f$. The above equations will be used later in the introduction to polarization analysis.

1.2.3 Neutron interactions at low energy

Let us study the interaction Hamiltonian of low energy neutrons with matter. A free neutron interacts with an atom through two kind of processes: the nuclear interaction with the nucleus, and the electromagnetic interaction of the neutron magnetic moment with the charge of the nucleus and the electrons.

The nuclear force is very complex and strong, so that it cannot be treated perturbatively in general. However, it is also extremely short ranged, its range being orders of magnitude shorter than the wavelength of slow neutrons (with energies smaller than a few eV). Therefore, slow neutrons are effectively scattered off a point like nucleus, and in this case the scattering is essentially isotropic: only the s-wave gives a substantial contribution to the amplitude of the scattered wave, which therefore is given by

$$\psi_{\mathrm{S}}(\vec{r}) = -\frac{b}{r} \, \mathrm{e}^{\mathrm{i}2\pi k r}, \tag{1.28}$$

where k is the neutron wave-number, $\vec{r}$ is the vector position of the neutron relative to the nucleus, and b is the so called *scattering length*, which in general is a complex number. The minus sign is conventionally chosen so that the real part of b is positive for a repulsive force. The imaginary part of b is only significant in the vicinity of capture resonances, that is, for nuclei that strongly absorb slow neutrons. All the complexity of the nuclear force is embodied in the scattering length, which can be obtained from measurements. This allows us to construct an effective potential, the Fermi *pseudopotential* [4], which gives the exact result for scattering in the lowest order of perturbation theory (the first Born approximation):

$$V_{\mathrm{F}}(\vec{r}) = \frac{h^2}{2\pi m} \, b \, \delta(\vec{r}), \tag{1.29}$$

where m is the neutron mass and $\delta(\vec{r})$ the Dirac delta function. Indeed, an elementary application of perturbation theory gives (1.28) and $\sigma \sim |b|^2$ from the potential (1.29).

It is worthwhile to stress that (1.29) is not the complicated true nuclear interaction Hamiltonian, which is strong and non central. The Fermi pseudo-potential is a simple way to describe effectively the scattering of slow neutrons with a single parameter, b. The scattering lengths may be in principle computed from the nuclear interaction Hamiltonian, but this is a formidable problem. Fortunately, they are available from measurements.

The fact that the size of the atom is ~ 1 Å $= 10^{-10}$ m, the size of the nuclei is $\sim 10^{-14}$ m, and the short range of the neutron-nuclei interaction has as immediate consequence the high penetration power of neutrons in matter, except if there are absorbing isotopes. We can say that *from the point of view of neutrons, the matter is empty*, because they only *see* the nuclei which are $\sim 10^4$ times smaller than the atoms. This consequence facilitates the experiments with neutron beams using very complex sample environments, which are easily traversed by the neutrons. We will explain later that neutrons are also able to *see* the unpaired electrons at the atoms.

The nuclear interactions depend strongly on the spin of the nucleus and the neutron, and the above discussion holds for given total spin states of the neutron-nucleus system. That is, b in the above equations depends on the total spin of the neutron-nucleus system, which can take two values: $J^{\pm} = I \pm 1/2$, where I is the total spin of the nucleus[2]. Therefore, we have actually two scattering lengths, b^+ and b^-, corresponding to the two composite states with total spin J^+ and J^-, respectively. This dependence on the total spin can be taken into account by introducing a *scattering amplitude operator*, $\mathbb{B}$, which, due to the rotational symmetry, can be written as [5]

$$\mathbb{B} = A + B\frac{1}{2}\vec{\sigma}\cdot\vec{\mathcal{I}}, \tag{1.30}$$

where the components of matrix vector $\vec{\sigma}$ are the Pauli matrices that act on the neutron spin degrees of freedom, $\vec{\mathcal{I}}$ is the nucleus spin operator, and

$$A = \frac{1}{2I+1}[(I+1)b^+ + Ib^-], \qquad B = \frac{2}{2I+1}(b^+ - b^-). \tag{1.31}$$

Thus, we have to substitute the complex number b in (1.29) by the operator in spin space $\mathbb{B}$. If the target contains N nucleus, labelled by the index n and located at $\vec{R}_n$, the nuclear interaction Hamiltonian is

$$\mathcal{H}_{\text{int}}^{(\text{n})} = \frac{h^2}{2\pi m}\sum_{n=1}^{N}\mathbb{B}_n\delta(\vec{r}-\vec{R}_n), \tag{1.32}$$

[2]Note that since we are dealing with s-wave scattering, the total spin of the system is conserved.

with $\mathbb{B}_n$ given by (1.30).

The electromagnetic interactions are long ranged but very weak, and thus can be treated perturbatively in the Born approximation. In the scales involved in the problem, the neutron can be considered electromagnetically as a neutral point particle with a magnetic moment. Any other residual electromagnetic interaction originating from the internal structure of the neutron (higher order multipoles) is much smaller than the magnetic dipolar interaction. Since the nuclear magneton is two orders of magnitude smaller than the Bohr magneton, the interaction of the neutron magnetic moment with the nucleus is about two orders of magnitude weaker that the interactions with the electrons. The neutron-atom electromagnetic interaction is thus dominated by the interaction of the neutron magnetic moment with the electrons [6–8]. Generically, the electromagnetic interaction is introduced by substituting the momentum operator of the particle, $\vec{p}$, by $\vec{p}-q\vec{A}(\vec{r})$, where q is the electric charge of the particle and $\vec{A}(\vec{r})$ is the electromagnetic vector potential at the position of the particle. To this we have to add the dipole-dipole interaction between the intrinsic magnetic moments of the electron and the neutron, which is of relativistic origin, and is derived from the Dirac equation [8]. The dipole-dipole interaction potential can be written alternatively as the energy of the electron intrinsic magnetic moment in the magnetic field created by the intrinsic magnetic moment of the neutron, or as the energy of the neutron magnetic moment in the magnetic field created by the intrinsic magnetic moment of the electron. We will use the former form.

The vector potential at a point $\vec{r}_j$ by the magnetic moment of the neutron $\vec{\mu}_{\rm n}$, located at point $\vec{r}$, is

$$\vec{A}_{\rm n}(\vec{r}_j-\vec{r}\,)=\frac{\mu_0}{4\pi}\nabla_j\times\frac{\vec{\mu}_{\rm n}}{|\vec{r}_j-\vec{r}\,|}. \tag{1.33}$$

It originates a magnetic field

$$\vec{B}_{\rm n}(\vec{r}_j-\vec{r}\,)=\frac{\mu_0}{4\pi}\nabla_j\times\left(\nabla_j\times\frac{\vec{\mu}_{\rm n}}{|\vec{r}_j-\vec{r}\,|}\right)=\frac{\mu_0}{4\pi}\nabla\times\left(\nabla\times\frac{\vec{\mu}_{\rm n}}{|\vec{r}_j-\vec{r}\,|}\right), \tag{1.34}$$

where ∇ and ∇_j stand for the gradient with respect to $\vec{r}$ and $\vec{r}_j$, respectively, and $\mu_0=4\pi\times10^{-7}$H/m is the vacuum permeability.

Let us write the Hamiltonian, $\mathcal{H}$, of the system composed of a free neutron of momentum $\vec{k}$ and position $\vec{r}$ and a system of $N_{\rm e}$ electrons and $N_{\rm n}$ nuclei. Let us denote by $\vec{p}_j$ and $\vec{r}_j$ the j-th electron momentum and position, respectively, and by $\vec{R}_n$, $\vec{P}_n$, and M_n the n-th nucleus momentum, position,

and mass, respectively. We have

$$\mathcal{H} = \sum_{n=1}^{N_\mathrm{n}} \frac{1}{2M_n} P_n^2 + \sum_{j=1}^{N_\mathrm{e}} \frac{1}{2m_\mathrm{e}} \left[\vec{p}_j - e\vec{A}(\vec{r}_j)\right]^2 + U_\mathrm{s}(\vec{r}_j, \vec{R}_n) + \frac{1}{2m} k^2 + \mathcal{H}_\mathrm{int}^{(\mathrm{n})} - \sum_{j=1}^{N_\mathrm{e}} \vec{\mu}_j \cdot \vec{B}_\mathrm{n}(\vec{r}_j - \vec{r}), \tag{1.35}$$

where U_S contains the interaction of the electron-nuclei system, $\vec{\mu}_j$ is the magnetic moment operator of the j-th electron, and $\vec{A}(\vec{r}_j)$ is the total vector potential at the position of the j-th electron, and is a superposition of the internal vector potential of the electron-nuclei system, $\vec{A}_\mathrm{S}$, any applied external field, $\vec{A}_\mathrm{ext}$, and the vector potential due to the neutron, $\vec{A}_\mathrm{n}$:

$$\vec{A}(\vec{r}_j) = \vec{A}_\mathrm{S}(\vec{r}_j) + \vec{A}_\mathrm{ext}(\vec{r}_j) + \vec{A}_\mathrm{n}(\vec{r}_j - \vec{r}). \tag{1.36}$$

Notice that the vector potential is absent from the neutron kinetic energy term since it is a neutral particle, and, as discussed before, it is neglected in the nuclei terms. The last term in (1.35) is the dipole-dipole interaction between the electrons and the neutron. One has to bear in mind, when dealing with (1.35), that momentum and position of the same particle do not commute: they are operators that satisfy canonical commutation relations.

Let us write $\mathcal{H}$ in the form

$$\mathcal{H} = \mathcal{H}_\mathrm{S} + \frac{1}{2m} k^2 + \mathcal{H}_\mathrm{int}^{(\mathrm{n})} + \mathcal{H}_\mathrm{int}^{(\mathrm{m})} \tag{1.37}$$

where $\mathcal{H}_\mathrm{S}$ is the Hamiltonian of the electrons-nuclei system in absence of any neutron, and

$$\mathcal{H}_\mathrm{int}^{(\mathrm{m})} = \frac{\mu_0 \mu_\mathrm{B}}{2\pi} \vec{\mu}_\mathrm{n} \cdot \sum_{j=1}^{N_\mathrm{e}} \left[-\frac{1}{\hbar} \frac{\vec{r}_j - \vec{r}}{|\vec{r}_j - \vec{r}|^3} \times \vec{p}_j + \nabla \times \left(\nabla \times \frac{\vec{s}_j}{|\vec{r}_j - \vec{r}|} \right) \right] \tag{1.38}$$

is the *magnetic interaction* Hamiltonian, neglecting the terms quadratic in $\vec{A}$, which are quadratic in e and thus two orders of magnitude smaller than the linear terms. In deriving $\mathcal{H}_\mathrm{int}^{(\mathrm{m})}$ we have used $\vec{p}_j = -\mathrm{i}\hbar\nabla_j$ and $\nabla_j \cdot \vec{A}_n = 0$. As usual, $\mu_\mathrm{B} = -e\hbar/2m_\mathrm{e} \approx 9.27 \times 10^{-24}\mathrm{J/T}$ is the Bohr magneton and we set $\vec{\mu}_j = -2\mu_\mathrm{B}\vec{s}_j$, where $\vec{s}_j$ is the spin operator of the j-th electron in units of $\hbar$, whose eigenvalues are $\pm 1/2$. We will see that the first and second terms within the square brackets of (1.38) give the magnetic scattering due to orbital and spin magnetic moments, respectively.

1.2.4 Nuclear Scattering

For nuclear scattering (1.32), the $\mathcal{A}_{\vec{q}}$ operator (1.7) takes the simple form

$$\mathcal{A}_{\vec{q}}^{(\mathrm{n})} = \sum_{n=1}^{N_\mathrm{n}} \left(A_n + \frac{1}{2} B_n \vec{\mathcal{I}}_n \cdot \vec{\sigma} \right) \mathrm{e}^{\mathrm{i}2\pi\vec{q}\cdot\vec{R}_n}. \tag{1.39}$$

We will consider here the case of real A_n and B_n (no absorption). We have to compute the time correlation function entering the right-hand side of (1.13)

$$\mathrm{Tr}\ \overline{\langle \mathcal{A}^{(\mathrm{n})\,\dagger}_{\vec{q}}(0)\,\mathcal{P}_{\sigma_f}\,\mathcal{A}^{(\mathrm{n})}_{\vec{q}}(t)\,\varrho_i\rangle}, \tag{1.40}$$

The result is obtained straightforwardly after introducing the physically reasonable assumptions enumerated in the following list.

1. The nuclear spin dynamics are very weakly correlated to the nuclear motion, so that the correlation

$$\left\langle \mathcal{I}^{\alpha}_{n}(0)\mathcal{I}^{\beta}_{n'}(t)\mathrm{e}^{-\mathrm{i}2\pi\vec{q}\cdot\vec{R}_{n'}(0)}\mathrm{e}^{\mathrm{i}2\pi\vec{q}\cdot\vec{R}_{n}(t)}\right\rangle \tag{1.41}$$

   factorizes as

$$\left\langle \mathcal{I}^{\alpha}_{n}(0)\mathcal{I}^{\beta}_{n'}(t)\right\rangle\left\langle \mathrm{e}^{-\mathrm{i}2\pi\vec{q}\cdot\vec{R}_{n'}(0)}\mathrm{e}^{\mathrm{i}2\pi\vec{q}\cdot\vec{R}_{n}(t)}\right\rangle. \tag{1.42}$$

2. The nuclei are not polarized, so that $\langle\vec{\mathcal{I}}\rangle = 0$.

3. The spins of different nuclei are also weakly coupled and therefore essentially uncorrelated, so that $\langle \mathcal{I}^{\alpha}_{n}(t)\mathcal{I}^{\beta}_{n'}(0)\rangle = \langle \mathcal{I}^{\alpha}_{n}(t)\mathcal{I}^{\beta}_{n}(0)\rangle\,\delta_{nn'}$.

4. The dynamics of the nuclear spins are much slower than the orbital dynamics, since the interactions of the nuclear spins are in general very weak. We then neglect the time dependence of $\langle \mathcal{I}^{\alpha}_{n}(t)\mathcal{I}^{\beta}_{n}(0)\rangle$.

5. The nuclear spin motion is nearly random, and therefore

$$\langle \mathcal{I}^{\alpha}_{n}\mathcal{I}^{\beta}_{n}\rangle = \frac{1}{3}\langle\vec{\mathcal{I}}^2\rangle\delta_{\alpha\beta} = \frac{1}{3}I_n(I_n+1)\delta_{\alpha\beta}. \tag{1.43}$$

6. The isotopic probability distributions of nuclei n and n' are independent, which means

$$\overline{A_nA_{n'}} = \overline{A}_n\,\overline{A}_{n'}\,(1-\delta_{nn'}) + \overline{A^2_n}\,\delta_{nn'} = \overline{A}_n\,\overline{A}_{n'} + (\overline{A^2_n} - \overline{A}^2_n)\delta_{nn'}. \tag{1.44}$$

From these assumptions we have

$$\sum_{\alpha,\beta}\frac{1}{4}\overline{B_nB_{n'}\langle \mathcal{I}^{\alpha}_{n}(t)\mathcal{I}^{\beta}_{n'}(0)\rangle}\,\mathrm{Tr}(\sigma_\alpha\mathcal{P}_{\sigma_f}\sigma_\beta\varrho_i) = \frac{1}{4}\overline{B^2_nI_n(I_n+1)}\,\delta_{nn'}\,\langle\sigma_f|\,\varrho_i\,|\sigma_f\rangle\,, \tag{1.45}$$

where we used $\sum_{\alpha\beta}\delta_{\alpha\beta}\sigma_\alpha\varrho_i\sigma_\beta = 3\varrho_i$.

It is convenient to define the *coherent* and *incoherent* scattering length as, respectively, $b_{\mathrm{coh},n} = b_n = \overline{A}_n$ and

$$b_{\mathrm{inc},n} = \left[(\overline{A^2_n} - \overline{A}^2_n) + (1/4)\overline{B^2_nI_n(I_n+1)}\right]^{1/2}. \tag{1.46}$$

The average is over isotope abundance in the target.

Taking into account the above considerations, it is straightforward to obtain

$$\begin{aligned}\mathrm{Tr}\ \overline{\langle \mathcal{A}_{\vec{q}}^{(\mathrm{n})\,\dagger}(0)\mathcal{P}_{\sigma_f}\mathcal{A}_{\vec{q}}^{(\mathrm{n})}(t)\varrho_i\rangle} = \\ \sum_{nn'}(b_n b_{n'} + b_{\mathrm{inc},n}^2\delta_{nn'})\langle \mathrm{e}^{-\mathrm{i}2\pi\vec{q}\cdot\vec{R}_{n'}(0)}\mathrm{e}^{\mathrm{i}2\pi\vec{q}\cdot\vec{R}_n(t)}\rangle \langle\sigma_f|\,\varrho_i\,|\sigma_f\rangle\,.\end{aligned} \tag{1.47}$$

By definition, the density matrix of a beam is the matrix whose expectation value in a spin state gives the probability of such state in the beam. Equation (1.47) shows that, in the case of nuclear scattering by unpolarized nuclei, the density matrix of the scattered beam is the same as the density matrix of the incident beam, so that there is no change in polarization. Since polarization is uninteresting at this point, in the remaining of this section we will sum over the polarization states of the scattered neutrons.

Equation (1.47) allows us to separate the nuclear scattering cross section into coherent and incoherent components

$$\frac{d^2\sigma^{(\mathrm{n})}}{d\Omega_{\hat{k}_f}dE_f} = \frac{d^2\sigma_{\mathrm{coh}}^{(\mathrm{n})}}{d\Omega_{\hat{k}_f}dE_f} + \frac{d^2\sigma_{\mathrm{inc}}^{(\mathrm{n})}}{d\Omega_{\hat{k}_f}dE_f}, \tag{1.48}$$

where

$$\frac{d^2\sigma_{\mathrm{coh}}^{(\mathrm{n})}}{d\Omega_{\hat{k}_f}dE_f} = \frac{k_f}{k_i}\sum_{nn'} b_n b_{n'}\langle \mathrm{e}^{-\mathrm{i}2\pi\vec{q}\cdot\vec{R}_n(0)}\mathrm{e}^{\mathrm{i}2\pi\vec{q}\cdot\vec{R}_{n'}(t)}\rangle_\nu \tag{1.49}$$

is the *coherent nuclear scattering cross section*, and

$$\frac{d^2\sigma_{\mathrm{inc}}^{(\mathrm{n})}}{d\Omega_{\hat{k}_f}dE_f} = \frac{k_f}{k_i}\sum_{n} b_{\mathrm{inc},n}^2\langle \mathrm{e}^{-\mathrm{i}2\pi\vec{q}\cdot\vec{R}_n(0)}\mathrm{e}^{\mathrm{i}2\pi\vec{q}\cdot\vec{R}_n(t)}\rangle_\nu \tag{1.50}$$

is the *incoherent nuclear scattering cross section*. Remember that $\langle \mathbb{AB}\rangle_\nu$ is defined in equation (1.14). Notice that, in spite of the appearance due to the condensed notation, the two operators within brackets in equation (1.50) are not inverse, since they are taken at different times.

Notice the big difference between coherent and incoherent scattering. The former gives the Fourier transform of the time correlation function between pairs of nucleus [9]. Indeed, in the case of a *monoatomic* target, it is usual to write the scattering cross section as

$$\frac{d^2\sigma}{d\Omega_{\hat{k}_f}dE_f} = \frac{\sigma_{\mathrm{coh}}}{4\pi}\frac{k_f}{k_i}N_{\mathrm{n}}\,S_{\mathrm{coh}}(\vec{q},\nu) + \frac{\sigma_{\mathrm{inc}}}{4\pi}\frac{k_f}{k_i}N_{\mathrm{n}}\,S_{\mathrm{inc}}(\vec{q},\nu) \tag{1.51}$$

where $\sigma_{\mathrm{coh}} = 4\pi b_{\mathrm{coh}}^2$, $\sigma_{\mathrm{inc}} = 4\pi b_{\mathrm{inc}}^2$, and S_{coh} and S_{inc} are called the coherent

and incoherent *scattering functions*[3], given, respectively, by

$$S_{\rm coh}(\vec{q},\nu)=\frac{1}{N_{\rm n}}\sum_{nn'}\langle {\rm e}^{-{\rm i}2\pi\vec{q}\cdot\vec{R}_n(0)}{\rm e}^{{\rm i}2\pi\vec{q}\cdot\vec{R}_{n'}(t)}\rangle_\nu \tag{1.52}$$

and

$$S_{\rm inc}(\vec{q},\nu)=\frac{1}{N_{\rm n}}\sum_{n}\langle {\rm e}^{-{\rm i}2\pi\vec{q}\cdot\vec{R}_n(0)}{\rm e}^{{\rm i}2\pi\vec{q}\cdot\vec{R}_{n}(t)}\rangle_\nu. \tag{1.53}$$

The coherent scattering function is the Fourier transform of the *time-dependent pair-correlation function* $G(\vec{r},t)$ [9],

$$S_{\rm coh}(\vec{q},\nu)=\int\frac{dt}{h}{\rm e}^{-{\rm i}2\pi\nu t}\int d^3r\,{\rm e}^{{\rm i}2\pi\vec{q}\cdot\vec{r}}\,G(\vec{r},t), \tag{1.54}$$

which is defined by[4]

$$G(\vec{r},t)=\frac{1}{N_{\rm n}}\sum_{nn'}\int d^3r'\langle\delta[\vec{r}-\vec{r}'-\vec{R}_n(0)]\delta[\vec{r}'-\vec{R}_{n'}(t)]\rangle. \tag{1.55}$$

Analogously, the incoherent scattering function is the Fourier transform of the time-dependent self-correlation function $G_{\rm s}(\vec{r},t)$ [9]

$$S_{\rm inc}(\vec{q},\nu)=\int\frac{dt}{h}{\rm e}^{-{\rm i}2\pi\nu t}\int d^3r\,{\rm e}^{{\rm i}2\pi\vec{q}\cdot\vec{r}}\,G_{\rm s}(\vec{r},t), \tag{1.56}$$

where

$$G_{\rm s}(\vec{r},t)=\frac{1}{N_{\rm n}}\sum_{n}\int d^3r'\langle\delta[\vec{r}-\vec{r}'-\vec{R}_n(0)]\delta[\vec{r}'-\vec{R}_{n}(t)]\rangle. \tag{1.57}$$

It is also convenient to define the *intermediate functions* as

$$I_{\rm coh}(\vec{q},t)=\int d^3r\,{\rm e}^{{\rm i}2\pi\vec{q}\cdot\vec{r}}\,G(\vec{r},t) \tag{1.58}$$

$$I_{\rm inc}(\vec{q},t)=\int d^3r\,{\rm e}^{{\rm i}2\pi\vec{q}\cdot\vec{r}}\,G_{\rm s}(\vec{r},t) \tag{1.59}$$

These ideas are not specific to monoatomic targets, not even to nuclear scattering. It is a general feature that coherent scattering provides information about the time-dependent correlations between pairs of degrees of freedom in the target, while incoherent scattering provides information about the time self-correlation function of single degrees of freedom in the target.

[3] The scattering function is also called response function, dynamic scattering function, dynamic structure factor or scattering law.

[4] These expressions have to be manipulated carefully, since the Heisenberg operators $\vec{R}_n(0)$ and $\vec{R}_{n'}(t)$ do not commute for $t\neq 0$. For instance,

$$\exp\{-{\rm i}2\pi\vec{q}\cdot\vec{R}_n(0)\}\exp\{{\rm i}2\pi\vec{q}\cdot\vec{R}_{n'}(t)\}\neq\exp\{{\rm i}2\pi\vec{q}\cdot[\vec{R}_{n'}(t)-\vec{R}_n(0)]\}.$$

Elastic nuclear scattering

After summing over the neutron final spin states, an expression for the elastic nuclear scattering is obtained from [*c.f.* Eq. (1.22)] [5].

$$\mathrm{Tr}\left[\overline{\langle\mathcal{A}_{\vec{q}}^{(\mathrm{n})\,\dagger}\rangle\langle\mathcal{A}_{\vec{q}}^{(\mathrm{n})}\rangle}\varrho_i\right] = \sum_{nn'}(b_n b_{n'} + b_{\mathrm{inc},n}^2\delta_{nn'})\langle \mathrm{e}^{-\mathrm{i}2\pi\vec{q}\cdot\vec{R}_n}\rangle\langle \mathrm{e}^{\mathrm{i}2\pi\vec{q}\cdot\vec{R}_{n'}}\rangle. \quad (1.60)$$

In fluids, the particle motion is translational, or diffusive, and takes place in a region of macroscopic dimensions, much larger than $1/q$, and thus the expectation value $\langle\exp\{\mathrm{i}2\pi\vec{q}\cdot\vec{R}_n\}\rangle$ vanishes unless $\vec{q}=0$. But $\nu=0$ and $\vec{q}=0$ means that there is no scattering at all, so that in liquids all scattering is inelastic. In solids, however, the particle motion takes place around an equilibrium position and is limited to a region comparable to $1/q$, and therefore $\langle\exp\{\mathrm{i}2\pi\vec{q}\cdot\vec{R}_n\}\rangle \neq 0$. Hence, elastic scattering in solids is very important, and often dominant.

Expression (1.60) allows us to obtain the *coherent and incoherent nuclear elastic* cross section, which are given by

$$\frac{d\sigma_{\mathrm{coh}}^{(\mathrm{n,\,e})}}{d\Omega_{\hat{k}_f}} = \Big|\sum_n b_n\langle \mathrm{e}^{\mathrm{i}2\pi\vec{q}\cdot\vec{R}_n}\rangle\Big|^2, \quad (1.61)$$

and

$$\frac{d\sigma_{\mathrm{inc}}^{(\mathrm{n,\,e})}}{d\Omega_{\hat{k}_f}} = \sum_n b_{\mathrm{inc},n}^2\Big|\langle \mathrm{e}^{\mathrm{i}2\pi\vec{q}\cdot\vec{R}_n}\rangle\Big|^2, \quad (1.62)$$

respectively. Notice again the big difference between coherent and incoherent elastic scattering. The coherent scattering is characterized by the strong interference between the scattered waves, which produces peaks in the scattered intensity along specific directions, determined by the sample atomic structure, that frequently are very sharp. This interference is completely absent in the incoherent scattering, that is entirely due to the presence of disorder, which cancels the interference terms. Thus, the contribution of the incoherent scattering is often merely a smooth background.

Inelastic nuclear scattering

The inelastic scattering cross section is obtained by susbtracting the elastic scattering from the whole cross section. The explicit expressions are

$$\frac{d^2\sigma_{\mathrm{coh}}^{(\mathrm{n,i})}}{d\Omega_{\hat{k}_f}dE_f} = \frac{k_f}{k_i}\int\frac{dt}{h}\,\mathrm{e}^{-\mathrm{i}2\pi\nu t}\sum_{nn'}b_n b_{n'}\times \left[\left\langle \mathrm{e}^{-\mathrm{i}2\pi\vec{q}\cdot\vec{R}_n(0)}\mathrm{e}^{\mathrm{i}2\pi\vec{q}\cdot\vec{R}_{n'}(t)}\right\rangle - \left\langle \mathrm{e}^{-\mathrm{i}2\pi\vec{q}\cdot\vec{R}_n}\right\rangle\left\langle \mathrm{e}^{\mathrm{i}2\pi\vec{q}\cdot\vec{R}_{n'}}\right\rangle\right] \quad (1.63)$$

[5] Equivalently the elastic nuclear scattering can be obtained from the $t\to\infty$ limit of equation (1.47)

for the *coherent nuclear inelastic* cross section, and

$$\frac{d^2\sigma^{(\mathrm{n,i})}_{\mathrm{inc}}}{d\Omega_{\hat{k}_f}dE_f} = \frac{k_f}{k_i}\int \frac{dt}{h}\,\mathrm{e}^{-\mathrm{i}2\pi\nu t}\sum_n b^2_{\mathrm{inc},n}\times \left[\left\langle \mathrm{e}^{-\mathrm{i}2\pi\vec{q}\cdot\vec{R}_n(0)}\mathrm{e}^{\mathrm{i}2\pi\vec{q}\cdot\vec{R}_n(t)}\right\rangle - \left\langle \mathrm{e}^{-\mathrm{i}2\pi\vec{q}\cdot\vec{R}_n}\right\rangle\left\langle \mathrm{e}^{\mathrm{i}2\pi\vec{q}\cdot\vec{R}_n}\right\rangle\right] \tag{1.64}$$

for the *incoherent nuclear inelastic* component.

In fluids, the elastic scattering is absent and the time-dependent pair correlations and self-correlations are related to mean inter-particle distances, velocity correlations and other properties of the fluid motion [10].

In solids, the nuclei perform oscillations about some equilibrium position. Let $\vec{R}_n = \vec{R}^{\mathrm{e}}_n + \vec{u}_n$, where $\vec{R}^{\mathrm{e}}_n = \langle \vec{R}_n\rangle$ denotes the equilibrium position and $\vec{u}_n$ is the quantum operator that describes the displacements from the equilibrium position. Then (1.63) can be written as

$$\frac{d^2\sigma^{(\mathrm{n,i})}_{\mathrm{coh}}}{d\Omega_{\hat{k}_f}dE_f} = \frac{k_f}{k_i}\int \frac{dt}{h}\,\mathrm{e}^{-\mathrm{i}2\pi\nu t}\sum_{nn'} b_n b_{n'}\mathrm{e}^{\mathrm{i}2\pi\vec{q}\cdot(\vec{R}^{\mathrm{e}}_{n'}-\vec{R}^{\mathrm{e}}_n)}T_n(-\vec{q})T_{n'}(\vec{q})\times \left[\frac{\left\langle \mathrm{e}^{-\mathrm{i}2\pi\vec{q}\cdot\vec{u}_n(0)}\mathrm{e}^{\mathrm{i}2\pi\vec{q}\cdot\vec{u}_{n'}(t)}\right\rangle}{T_n(-\vec{q})T_{n'}(\vec{q})} - 1\right], \tag{1.65}$$

where

$$T_n(\vec{q}) = \left\langle \mathrm{e}^{\mathrm{i}2\pi\vec{q}\cdot\vec{u}_n}\right\rangle \tag{1.66}$$

is the so called Debye-Waller factor.

If we assume that the displacements from the equilibrium position are small, the dynamics of $\vec{u}_n$ is approximately described by a set of coupled harmonic oscillators. Then, $\vec{u}_n(t)$ can be expanded in terms of normal modes, the phonons, which describe the collective excitations of the system, as

$$\vec{u}_n(t) = \sum_r \sqrt{\frac{h}{2M_n\nu_r}}\vec{\xi}_{r,n}\left(\mathrm{e}^{-\mathrm{i}2\pi\nu_r t}a_r + \mathrm{e}^{\mathrm{i}2\pi\nu_r t}a^\dagger_r\right), \tag{1.67}$$

where M_n is the mass of the n-th nucleus, $r = 1,\ldots,N_{\mathrm{p}}$ labels the phonon branches, N_{p} is the number of different phonon branches, and ν_r, $\vec{\xi}_{r,n}$, a_r and $a^\dagger_r$ are the frequency, the polarization vector, and the annihilation and creation operators of the corresponding phonon, respectively. The polarization vectors are real and dimensionless, and satisfy the normalization and closure conditions

$$\sum_n \vec{\xi}_{r,n}\cdot\vec{\xi}_{r',n} = \delta_{rr'}, \qquad \sum_r \xi^\alpha_{r,n}\xi^\beta_{r,n'} = \delta_{\alpha\beta}\delta_{nn'}. \tag{1.68}$$

The numerical factor in the right-hand side of (1.67) arises from the canonical commutation relations. Notice that expression (1.67) is valid for crystalline as well as for amorphous solids.

The term within brackets in (1.65) is an even function of $\vec{q}$. We expand it in powers of $\vec{q}$ and we get only even powers of the components of $\vec{q}$. The term of order $2p$ is called the p-phonon term, and is interpreted as a sum of scattering events in which p phonons are involved, some absorbed and some emitted. It is not difficult to get the 1-phonon term, which is the most important since it provides the phonon spectrum. To second order in $\vec{q}$ we have

$$\frac{\left\langle \mathrm{e}^{-\mathrm{i}2\pi\vec{q}\cdot\vec{u}_n(0)}\mathrm{e}^{\mathrm{i}2\pi\vec{q}\cdot\vec{u}_{n'}(t)}\right\rangle}{T_n(-\vec{q})T_{n'}(\vec{q})} - 1 = 4\pi^2\left\langle[\vec{q}\cdot\vec{u}_n(0)][\vec{q}\cdot\vec{u}_n(t)]\right\rangle + O(q^4). \quad (1.69)$$

From equations (1.69) and (1.67) we see that we have to compute $\langle a_r a_{r'}\rangle$, $\langle a_r a_{r'}^\dagger\rangle$, $\langle a_r^\dagger a_{r'}\rangle$, and $\langle a_r^\dagger a_{r'}^\dagger\rangle$. The phonons form an ideal Bose gas of non-conserved particles, thus it has zero chemical potential and, at temperature T, the thermal quantum average of an operator $\mathcal{O}$ is given by

$$\langle\mathcal{O}\rangle = \frac{1}{Z}\sum_{n_1=1}^{\infty}\cdots\sum_{n_{N_\mathrm{p}}=1}^{\infty}\langle n_1,\ldots,n_{N_\mathrm{p}}|\,\mathcal{O}\,|n_1,\ldots,n_{N_\mathrm{p}}\rangle\exp\Big(-\sum_{r=1}^{N_\mathrm{p}} n_r h\nu_r/k_\mathrm{B}T\Big), \quad (1.70)$$

where Z is the partition function and $|n_1,\ldots,n_{N_\mathrm{p}}\rangle$ is the state that contains n_r phonons of type r. Clearly we have $\langle a_r a_{r'}\rangle = \langle a_r^\dagger a_{r'}^\dagger\rangle = 0$ and

$$\langle a_r a_{r'}^\dagger\rangle = \langle n_r\rangle\,\delta_{rr'}, \qquad \langle a_r^\dagger a_{r'}\rangle = [1+\langle n_r\rangle]\,\delta_{rr'}, \quad (1.71)$$

where in the last equation we used the commutation relation $[a_r, a_{r'}] = \delta_{rr'}$, and $\langle n_r\rangle$ is the avearge value of the number of type r phonons, given by the Bose-Einstein statistics:

$$\langle n_r\rangle = \frac{1}{\exp(h\nu_r/k_\mathrm{B}T)+1}. \quad (1.72)$$

Then we have

$$\begin{aligned}\left\langle[\vec{q}\cdot\vec{u}_n(0)][\vec{q}\cdot\vec{u}_{n'}(t)]\right\rangle = \sum_r\Big[&(\vec{q}\cdot\vec{\xi}_{r,n})(\vec{q}\cdot\vec{\xi}_{r,n'})^*(1+\langle n_r\rangle)\mathrm{e}^{\mathrm{i}2\pi\nu_r t}\\ &+(\vec{q}\cdot\vec{\xi}_{r,n})^*(\vec{q}\cdot\vec{\xi}_{r,n'})\langle n_r\rangle\mathrm{e}^{-\mathrm{i}2\pi\nu_r t}\Big].\end{aligned} \quad (1.73)$$

Inserting equations (1.69) and (1.73) into (1.65) we obtain, to 1-phonon level

$$\frac{d^2\sigma^{(\mathrm{n,i})}_{\mathrm{coh,1ph}}}{d\Omega_{\hat{k}_f}dE_f} = \frac{k_f}{k_i}(2\pi)^2q^2\sum_r|\hat{q}\cdot\vec{v}_r(\vec{q})|^2\frac{1}{2\nu_r}\left[(1+\langle n_r\rangle)\delta(\nu-\nu_r)+\langle n_r\rangle\delta(\nu+\nu_r)\right], \quad (1.74)$$

where

$$\vec{v}_r(\vec{q}) = \sum_n \mathrm{e}^{\mathrm{i}2\pi\vec{q}\cdot\vec{R}_n^\mathrm{e}}\frac{b_n}{\sqrt{M_n}}T_n(\vec{q})\,\vec{\xi}_{r,n}. \quad (1.75)$$

The first term in equation (1.74) corresponds to a neutron loosing an amount of energy $h\nu_r$ by creating one r-type phonon, and the second term to a neutron gaining an amount of energy $h\nu_r$ by absorbing one r-type phonon. In the case of an amorphous solid one has to average over the disorder in equilibrium positions and harmonic forces between nuclei, and the phonon spectrum is a continuum whose structure is difficult to disentangle. In this case, the more interesting quantity is the density of states. For a crystal, however, the phonon spectrum is separated into phonon branches and the coherent 1-phonon neutron scattering allows to obtain the dispersion relation of each branch, as we will see.

An analogous phonon expansion can be developed for the incoherent inelastic cross section. For a monoatomic system it can be expressed solely in terms of the density of states. The 1-phonon contribution to the incoherent scattering has the relatively simple expression

$$\frac{d^2\sigma^{(\mathrm{n,i})}_{\mathrm{inc,1ph}}}{d\Omega_{\hat{k}_f} dE_f} = N_{\mathrm{n}} \frac{k_f}{k_i} \frac{b^2_{\mathrm{inc}}}{2M} (2\pi)^2 q^2 \left|T(\vec{q})\right|^2 \frac{Z(\nu)}{\nu} \frac{1}{2} \left[\coth\left(\frac{h\nu}{2k_{\mathrm{B}}T}\right) + 1\right], \quad (1.76)$$

where $Z(\nu) = \sum_r \delta(\nu - \nu_r)$ for $\nu > 0$ is the density of states, and we have defined $Z(-\nu) = Z(\nu)$.

Expressions (1.74) and (1.76) are valid in the harmonic approximation. Anharmonic corrections are usually important only at high temperature, but some phenomena like thermal expansion and thermal conductivity in solids cannot be explained without anharmonicity [11]. In the harmonic approximation, the Debye-Waller factor takes the simple form

$$T_n(\vec{q}) = \mathrm{e}^{-\vec{q}\cdot\tilde{\beta}_n\vec{q}}, \quad (1.77)$$

where $\tilde{\beta}_n$ is a 3×3 matrix that depends on the temperature and on the frequencies and polarization vectors of phonons.

1.2.5 Magnetic Scattering

Expressions for the magnetic scattering cross section can be obtained by applying the same ideas as in nuclear scattering. The derivations, and the expressions are much more difficult since the magnetic interaction Hamiltonian is much more complex than its nuclear counterpart. Furthermore, the atomic wave functions of the electrons enter the final results, due to the long range nature of the magnetic interactions.

Let us denote by $\mathcal{A}^{(\mathrm{m})}_{\vec{q}}$ the amplitude operator corresponding to magnetic scattering, defined by equation (1.7). Since the interaction Hamiltonian is

given by equation (1.38), we need the two integrals:

$$\int d^3r\, \mathrm{e}^{\mathrm{i}2\pi\vec{q}\cdot\vec{r}}\, \frac{\vec{r}_j - \vec{r}}{|\vec{r}_j - \vec{r}|^3} = -\mathrm{i}4\pi \mathrm{e}^{\mathrm{i}2\pi\vec{q}\cdot\vec{r}_j}\, \frac{\hat{q}}{q}, \tag{1.78}$$

$$\int d^3r\, \mathrm{e}^{\mathrm{i}2\pi\vec{q}\cdot\vec{r}}\, \nabla\times\left(\nabla\times\frac{\vec{s}_j}{|\vec{r}_j - \vec{r}|}\right) = 4\pi \mathrm{e}^{\mathrm{i}2\pi\vec{q}\cdot\vec{r}_j}\, \hat{q}\times(\vec{s}_j\times\hat{q}). \tag{1.79}$$

Then we can write $\mathcal{A}_{\vec{q}}^{(\mathrm{m})} = p\,\vec{\mathcal{M}}_{\perp\vec{q}}\cdot\vec{\sigma}$, where the operator

$$\vec{\mathcal{M}}_{\perp\vec{q}} = -2\mu_{\mathrm{B}}\sum_j \mathrm{e}^{\mathrm{i}2\pi\vec{q}\cdot\vec{r}_j}\left[\hat{q}\times(\vec{s}_j\times\hat{q}) + \frac{\mathrm{i}}{\hbar q}(\vec{p}_j\times\hat{q})\right], \tag{1.80}$$

is called the *magnetic interaction vector operator* and acts only on the electron degrees of freedom. The factor $-2\mu_{\mathrm{B}}$ in $\vec{\mathcal{M}}_{\perp\vec{q}}$ is introduced by convenience, so that, as we will show later, $\vec{\mathcal{M}}_{\perp\vec{q}}$ is the component perpendicular to the scattering vector of the Fourier transform of the magnetization density operator. With these definitions, we have $p = (m/m_{\mathrm{p}})\gamma r_{\mathrm{e}}/2\mu_{\mathrm{B}}$, where $r_{\mathrm{e}} = e^2/(4\pi\epsilon_0 m_{\mathrm{e}}c^2)$, with ϵ_0 and c being the vacuum permittivity and the velocity of light, respectively. It is customary to substitute by one the ratio between the neutron and proton mass, which is approximately 1.0014. The quantity r_{e} is the so called classical radius of the electron, and has the value $r_{\mathrm{e}} \approx 2.818\times10^{-15}$m. This is of the same order of magnitude as the nuclear scattering lengths, which means that *the magnetic scattering of thermal neutrons is of the same order of magnitude as the nuclear scattering.* The constant $p = 0.2695$ provides the conversion of magnetic moments, given in Bohr magnetons μ_{B}, to scattering lengths in units of 10^{-14} m.

Clearly, $\vec{\mathcal{M}}_{\perp\vec{q}}$ is orthogonal to $\vec{q}$, and can be written as

$$\vec{\mathcal{M}}_{\perp\vec{q}} = \hat{q}\times(\vec{\mathcal{M}}_{\vec{q}}\times\hat{q}) = \vec{\mathcal{M}}_{\vec{q}} - \left(\hat{q}\cdot\vec{\mathcal{M}}_{\vec{q}}\right)\hat{q}, \tag{1.81}$$

or, in components

$$\mathcal{M}^{\alpha}_{\perp\vec{q}} = \sum_{\beta}\left(\delta_{\alpha\beta} - \frac{q_\alpha q_\beta}{q^2}\right)\mathcal{M}^{\beta}_{\vec{q}}\,, \tag{1.82}$$

where

$$\vec{\mathcal{M}}_{\vec{q}} = -2\mu_{\mathrm{B}}\sum_j \mathrm{e}^{\mathrm{i}2\pi\vec{q}\cdot\vec{r}_j}\left[\vec{s}_j + \frac{\mathrm{i}}{\hbar q}(\vec{p}_j\times\hat{q})\right] \tag{1.83}$$

is called the *magnetic structure factor operator*. Notice that any operator proportional to $\vec{q}$ can be added to $\vec{\mathcal{M}}_{\vec{q}}$ without changing $\vec{\mathcal{M}}_{\perp\vec{q}}$. This fact can be used to simplify some expressions of the matrix elements of $\vec{\mathcal{M}}_{\perp\vec{q}}$. We want to stress the following important fact: *only the component of* $\vec{\mathcal{M}}_{\vec{q}}$ *perpendicular to* $\vec{q}$ *contributes to the magnetic neutron scattering.* We anticipate here that $\vec{\mathcal{M}}_{\vec{q}}$ is the Fourier transform of the magnetic moment density,

or magnetization density, operator. Thus, not surprisingly, the magnetic scattering of neutrons is closely linked to the magnetization density.

Using the general formula (1.15), we obtain the following expression for the magnetic scattering cross section in the case that the scattered neutron polarization state, σ_f, is observed:

$$\left(\frac{d^2\sigma^{(\mathrm{m})}}{d\Omega_{\vec{k}_f}\,dE_f}\right)_{\sigma_f} = p^2\frac{k_f}{k_i}\sum_{\alpha\beta}\rho^i_{\alpha\beta}(\sigma_f)\left\langle \mathcal{M}^{\beta\,\dagger}_{\perp\vec{q}}(0)\,\mathcal{M}^{\alpha}_{\perp\vec{q}}(t)\right\rangle_\nu, \tag{1.84}$$

where $\mathcal{M}^{\alpha}_{\perp\vec{q}}$ is the α-th component of the $\vec{\mathcal{M}}_{\perp\vec{q}}$ operator, and

$$\rho^i_{\alpha\beta}(\sigma_f) = \langle\sigma_f|\,\sigma_\alpha\varrho_i\sigma_\beta\,|\sigma_f\rangle\,. \tag{1.85}$$

After integrating over dE_f, the elastic contribution to the magnetic scattering cross section is

$$\left(\frac{d\sigma^{(\mathrm{m,\,e})}}{d\Omega_{\hat{k}_f}}\right)_{\sigma_f} = p^2\sum_{\alpha\beta}\rho^i_{\alpha\beta}(\sigma_f)\langle\mathcal{M}^{\beta}_{\perp\vec{q}}\rangle^*\,\langle\mathcal{M}^{\alpha}_{\perp\vec{q}}\rangle, \tag{1.86}$$

and the inelastic contribution is

$$\begin{aligned}\left(\frac{d^2\sigma^{(\mathrm{m,\,i})}}{d\Omega_{\hat{k}_f}\,dE_f}\right)_{\sigma_f} &= p^2\frac{k_f}{k_i}\sum_{\alpha\beta}\rho^i_{\alpha\beta}(\sigma_f)\times\\ &\int\frac{dt}{h}\,\mathrm{e}^{-\mathrm{i}2\pi\nu t}\Big[\big\langle\mathcal{M}^{\beta\,\dagger}_{\perp\vec{q}}(0)\mathcal{M}^{\alpha}_{\perp\vec{q}}(t)\big\rangle - \big\langle\mathcal{M}^{\beta}_{\perp\vec{q}}\big\rangle^*\big\langle\mathcal{M}^{\alpha}_{\perp\vec{q}}\big\rangle\Big]\end{aligned} \tag{1.87}$$

If the polarization states of the scattered neutrons are not resolved, we have to sum over σ_f in the above expressions. Since

$$\sum_{\sigma_f}\rho^i_{\alpha\beta}(\sigma_f) = \delta_{\alpha\beta} - \sum_{\gamma}\epsilon_{\alpha\beta\gamma}P^\gamma_i, \tag{1.88}$$

where $\epsilon_{\alpha\beta\gamma}$ is the tridimensional totally antisymmetric tensor and $\vec{P}_i$ is the polarization vector of the incident beam, we obtain

$$\frac{d\sigma^{(\mathrm{m,\,e})}}{d\Omega_{\hat{k}_f}} = p^2\left[\langle\vec{\mathcal{M}}_{\perp\vec{q}}\rangle^*\cdot\langle\vec{\mathcal{M}}_{\perp\vec{q}}\rangle - \big(\langle\vec{\mathcal{M}}_{\perp\vec{q}}\rangle^*\times\langle\vec{\mathcal{M}}_{\perp\vec{q}}\rangle\big)\cdot\vec{P}_i\right] \tag{1.89}$$

for the *magnetic elastic* contribution, and

$$\begin{aligned}\frac{d^2\sigma^{(\mathrm{m,\,i})}}{d\Omega_{\hat{k}_f}\,dE_f} = p^2\frac{k_f}{k_i}\int\frac{dt}{h}\,\mathrm{e}^{-\mathrm{i}2\pi\nu t}\Big\{&\big\langle\vec{\mathcal{M}}^{\dagger}_{\perp\vec{q}}(0)\cdot\vec{\mathcal{M}}_{\perp\vec{q}}(t)\big\rangle - \langle\vec{\mathcal{M}}_{\perp\vec{q}}\rangle^*\cdot\langle\vec{\mathcal{M}}_{\perp\vec{q}}\rangle\\ &+\Big[\big\langle\vec{\mathcal{M}}^{\dagger}_{\perp\vec{q}}(0)\times\vec{\mathcal{M}}_{\perp\vec{q}}(t)\big\rangle - \langle\vec{\mathcal{M}}_{\perp\vec{q}}\rangle^*\times\langle\vec{\mathcal{M}}_{\perp\vec{q}}\rangle\Big]\cdot\vec{P}_i\Big\}\end{aligned} \tag{1.90}$$

for the *magnetic inelastic* contribution.

Physical meaning of the operator $\vec{\mathcal{M}}_{\perp\vec{q}}$

We show in the following that $\vec{\mathcal{M}}_{\perp\vec{q}}$ is the component of the Fourier transform of the magnetization density operator perpendicular to the scattering vector, $\vec{q}$ [12]. Let us write $\vec{\mathcal{M}}_{\perp\vec{q}} = \vec{\mathcal{M}}_{\mathrm{S}\perp\vec{q}} + \vec{\mathcal{M}}_{\mathrm{L}\perp\vec{q}}$, where $\vec{\mathcal{M}}_{\mathrm{S}\perp\vec{q}}$ and $\vec{\mathcal{M}}_{\mathrm{L}\perp\vec{q}}$ are the spin and orbital contributions to $\vec{\mathcal{M}}_{\perp\vec{q}}$:

$$\vec{\mathcal{M}}_{\mathrm{S}\perp\vec{q}} = -2\mu_{\mathrm{B}} \sum_j \mathrm{e}^{\mathrm{i}2\pi\vec{q}\cdot\vec{r}_j}\, \hat{q} \times (\vec{s}_j \times \hat{q}), \tag{1.91}$$

$$\vec{\mathcal{M}}_{\mathrm{L}\perp\vec{q}} = -2\mu_{\mathrm{B}} \sum_j \mathrm{e}^{\mathrm{i}2\pi\vec{q}\cdot\vec{r}_j} \frac{\mathrm{i}}{\hbar q} (\vec{p}_j \times \hat{q}). \tag{1.92}$$

It is clear that

$$\vec{\mathcal{M}}_{\mathrm{S}\perp\vec{q}} = \hat{q} \times (\vec{\mathcal{M}}_{\mathrm{S}\vec{q}} \times \hat{q}), \tag{1.93}$$

where $\vec{\mathcal{M}}_{\mathrm{S}\vec{q}}$ is the Fourier transform of

$$\vec{\mathbb{M}}_{\mathrm{S}}(\vec{r}) = \sum_j -2\mu_{\mathrm{B}}\, \vec{s}_j\, \delta(\vec{r} - \vec{r}_j), \tag{1.94}$$

which is the spin magnetic moment density operator, *i.e.*, the magnetization density operator due to spin.

Let us turm to the orbital part. Since $\vec{q}\cdot\vec{r}_j$ commutes with $\vec{p}_j \times \hat{q}$, because the former operator is proportional to the component of $\vec{r}_j$ parallel to $\vec{q}$ and the latter is the component of $\vec{p}_j$ perpendicular to $\vec{q}$, we have

$$\vec{\mathcal{M}}_{\mathrm{L}\perp\vec{q}} = -\mathrm{i}\, \frac{\mu_{\mathrm{B}}}{\hbar q} \sum_j \left[\mathrm{e}^{\mathrm{i}2\pi\vec{q}\cdot\vec{r}_j} (\vec{p}_j \times \hat{q}) + (\vec{p}_j \times \hat{q}) \mathrm{e}^{\mathrm{i}2\pi\vec{q}\cdot\vec{r}_j} \right]. \tag{1.95}$$

The above equation is equivalent to

$$\vec{\mathcal{M}}_{\mathrm{L}\perp\vec{q}} = \frac{\mathrm{i}}{q} \int d^3r \mathrm{e}^{\mathrm{i}2\pi\vec{q}\cdot\vec{r}} \vec{\mathbb{D}}(\vec{r}) \times \hat{q}, \tag{1.96}$$

where, bearing in mind that $\mu_{\mathrm{B}} = e\hbar/2m_{\mathrm{e}}$,

$$\vec{\mathbb{D}}(\vec{r}) = -\frac{e}{2m_{\mathrm{e}}} \sum_j \left[\delta(\vec{r} - \vec{r}_j)\vec{p}_j + \vec{p}_j \delta(\vec{r} - \vec{r}_j) \right]. \tag{1.97}$$

The operator $\vec{\mathbb{D}}(\vec{r})$ is $-e$ times the electron probability density current, and therefore it is the electric current density operator. The solenoidal part of $\vec{\mathbb{D}}$ is, by definition, the rotational of the orbital magnetic moment density, $\vec{\mathbb{M}}_{\mathrm{L}}(\vec{r})$, and the irrotational part, written as $\nabla\Phi$, is the conduction current:

$$\vec{\mathbb{D}}(\vec{r}) = \nabla \times \vec{\mathbb{M}}_{\mathrm{L}}(\vec{r}) + \nabla\Phi. \tag{1.98}$$

The Fourier transform of $\vec{\mathbb{D}}(\vec{r})$ is related to the Fourier transforms of $\vec{\mathbb{M}}_{\rm L}(\vec{r})$ and Φ by

$$\int d^3r \mathrm{e}^{\mathrm{i}2\pi\vec{q}\cdot\vec{r}}\vec{\mathbb{D}}(\vec{r}) = -\mathrm{i}\,\vec{q}\times\int d^3r \mathrm{e}^{\mathrm{i}2\pi\vec{q}\cdot\vec{r}}\vec{\mathbb{M}}_{\rm L}(\vec{r}) - \mathrm{i}\,\vec{q}\int d^3r \mathrm{e}^{\mathrm{i}2\pi\vec{q}\cdot\vec{r}}\Phi(\vec{r}). \quad (1.99)$$

Inserting the above equation into (1.96), and noticing that the term with $\Phi(\vec{r})$ does not contribute to it, since it is proportional to $\vec{q}$, we obtain $\vec{\mathcal{M}}_{{\rm L}\perp\vec{q}} = \hat{q}\times(\vec{\mathcal{M}}_{{\rm L}\vec{q}}\times\hat{q})$, where

$$\vec{\mathcal{M}}_{{\rm L}\vec{q}} = \int d^3r \mathrm{e}^{\mathrm{i}2\pi\vec{q}\cdot\vec{r}}\vec{\mathbb{M}}_{\rm L}(\vec{r}) \quad (1.100)$$

is the Fourier transform of the orbital magnetic moment density operator.

Collecting the spin and orbital contributions to $\vec{\mathcal{M}}_{\perp\vec{q}}$ we obtain

$$\vec{\mathcal{M}}_{\perp\vec{q}} = \hat{q}\times(\vec{\mathcal{M}}_{\vec{q}}\times\hat{q}), \quad (1.101)$$

where the magnetic structure factor operator, $\vec{\mathcal{M}}_{\vec{q}} = \vec{\mathcal{M}}_{{\rm L}\vec{q}} + \vec{\mathcal{M}}_{{\rm S}\vec{q}}$, is the Fourier transform of the total magnetization density operator, $\vec{\mathbb{M}}(\vec{r})$, which is the sum of the orbital, $\vec{\mathbb{M}}_{\rm L}(\vec{r})$, and spin, $\vec{\mathbb{M}}_{\rm S}(\vec{r})$, magnetization density operators. Therefore, $\vec{\mathcal{M}}_{\perp\vec{q}}$ is the perpendicular component of the Fourier transform of the total magnetization density operator to the direction of the scattering vector.

Let us stress again the important fact that *only the component of the magnetic structure factor operator perpendicular to the scattering vector contributes to the magnetic neutron scattering.*

Matrix elements of $\vec{\mathcal{M}}_{\perp\vec{q}}$

The computations of these matrix elements are complex and we will give here only some hints to understand the origin of the main ingredients that enter the matrix elements.

The matrix elements of $\vec{\mathcal{M}}_{\perp\vec{q}}$ between the states $|\varphi_i\rangle$ and $|\varphi_f\rangle$ cannot be computed generically without making assumptions about the system. For definiteness, let us consider a system in which the magnetic moments are due to the unpaired electrons localized at ions. This is the case of magnetic moments originated by unpaired p electrons belonging to molecular orbitals in organic radicals, and of transition metals and rare earths, in which the unpaired electrons that contribute to the magnetic moment belong to a d and to an f sub-shell, respectively.

Let N be the number of ions, labelled by the index n, and let N_n be the number of electrons of ion n-th. The position of the ion nucleus is denoted by $\vec{R}_n$, and the position of its j-th electron with respect to the ion center by $\vec{r}_{nj}$, so that the position of the nj-th electron is $\vec{R}_n + \vec{r}_{nj}$. The spin operator of the nj-th electron is $\vec{s}_{nj}$ and the spin quantum number corresponding to

the spin z component is denoted by $m_{\mathrm{s},nj}$. Let $e_{nj} = \{\vec{r}_{nj}, m_{\mathrm{s},nj}\}$ denote the complete set of electron degrees of freedom. The $\vec{\mathcal{M}}_{\perp\vec{q}}$ operator is given by

$$\vec{\mathcal{M}}_{\perp\vec{q}} = \sum_{n=1}^{N} \mathrm{e}^{\mathrm{i}2\pi\vec{q}\cdot\vec{R}_n} \vec{\mathcal{M}}^{(n)}_{\perp\vec{q}}, \tag{1.102}$$

where $\vec{\mathcal{M}}^{(n)}_{\perp\vec{q}} = \sum_{j=1}^{N_n} \vec{\mathcal{M}}^{(nj)}_{\perp\vec{q}}$, with

$$\vec{\mathcal{M}}^{(nj)}_{\perp\vec{q}} = -2\mu_{\mathrm{B}} \mathrm{e}^{\mathrm{i}2\pi\vec{q}\cdot\vec{r}_{nj}} \left[\hat{q} \times (\vec{s}_{nj} \times \hat{q}) + \frac{\mathrm{i}}{\hbar q}(\vec{p}_{nj} \times \hat{q})\right]. \tag{1.103}$$

The state of the system can be written as

$$|\varphi\rangle = \sum_{\mu_1} \cdots \sum_{\mu_N} \phi_{\mu_1,\ldots,\mu_N} |\psi_{\mu_1,1}\rangle \cdots |\psi_{\mu_N,N}\rangle, \tag{1.104}$$

where $\phi_{\mu_1,\ldots,\mu_N}$ depends only on the nuclei coordinates $\vec{R}_1 \ldots \vec{R}_N$, and the electronic wavefunction $\psi_{\mu_n,n}$ depends on $e_1, \ldots, e_{N_n}$ and is localized around the n-th ion position, $\vec{R}_n$. It is antisymmetric under electron exchange, and there is negligible overlapping between $\psi_{\mu_n,n}$ and $\psi_{\mu'_n,n'}$ if $n \neq n'$. Since the electronic states do not overlap, there is no need to antisymmetrize the wavefunction with respect to the exchange of electrons at different ions, in the sense that antisymmetrization does not change the result obtained with the above wavefunction. The index μ_n labels all the possible electronic states of the n-th ion, so that two different states differ by the functions ϕ.

The matrix element of $\vec{\mathcal{M}}_{\perp\vec{q}}$ between states $|\varphi_i\rangle$ and $|\varphi_f\rangle$ is

$$\begin{aligned}\langle\varphi_f| \vec{\mathcal{M}}_{\perp\vec{q}} |\varphi_i\rangle = \sum_n \sum_{\{\mu_1,\ldots,\mu_N\}_n} \sum_{\mu_n,\mu'_n} \int d^3R_1 \cdots d^3R_N \times \\ \phi^{(f)\,*}_{\mu_1,\ldots,\mu'_n,\ldots,\mu_N} \mathrm{e}^{\mathrm{i}2\pi\vec{q}\cdot\vec{R}_n} \langle\psi_{\mu'_n,n}| \vec{\mathcal{M}}^{(n)}_{\perp\vec{q}} |\psi_{\mu_n,n}\rangle \phi^{(i)}_{\mu_1,\ldots,\mu_N},\end{aligned} \tag{1.105}$$

where $\{\mu_1, \ldots, \mu_N\}_n$ stands for the set of $N-1$ indices $\mu_1, \ldots, \mu_N$ excluding μ_n. In the above equation we used the orthonormality of the ionic wavefunctions, $\langle\psi_{\mu,n}|\psi_{\mu',n}\rangle = \delta_{\mu\mu'}$. It is apparent that we only need the matrix element of $\vec{\mathcal{M}}^{(n)}_{\perp\vec{q}}$ between the electronic states localized at ion n-th.

We consider the electronic structure of the ion described by a Hartree-Fock scheme in the central field approximation [13]. The multi-electronic state, $|\psi_{\mu,n}\rangle$, is a suitable antisymmetric superposition of products of single electron states, which are computed from a self-consistent central potential common to all the electrons. Therefore, the single electron states are labelled by four numbers: the principal quantum number, n_{p}, the orbital angular momentum ℓ, the z component of the orbital angular momentum, m, and the spin z component, m_{s}. Recall that $-\ell \leq m \leq \ell$ and m_{s} take only the

two values $\pm 1/2$. The single electron state is written as $|n_{\rm p}\ell m m_{\rm s}\rangle$, and its wave function is given by

$$\langle \vec{r}|n_{\rm p}\ell m m_{\rm s}\rangle = f_{n_{\rm p}\ell}(r)\mathrm{Y}_\ell^m(\hat{r})\chi_{m_{\rm s}}, \tag{1.106}$$

where $f_{n_{\rm p}\ell}(r)$ is the radial wavefunction, $\mathrm{Y}_\ell^m(\hat{r})$ is the ℓm spherical harmonic evaluated on the polar angles θ and φ determined by the unit vector $\hat{r}$, and $\chi_{m_{\rm s}}$ is the $m_{\rm s}$ component of the two component spinor that describes the electron spin state. Due to the rotational symmetry of the single electron Hamiltonian, the energy is independent of m and $m_{\rm s}$. An $n_{\rm p}\ell$ state is called a *sub-shell*. At this zero-th order of approximation the electrons fill the $n_{\rm p}\ell$ sub-shells with lowest energy. The sub-shell $n_{\rm p}\ell$ can be occupied at most by $2(2\ell+1)$ states. A state of $n_{\rm e}$ electrons occupying the $n_{\rm p}\ell$ sub-shell is specified by the $2n_{\rm e}$ numbers $m_1 m_{\rm s1}, \ldots, m_{n_{\rm e}} m_{{\rm s}\, n_{\rm e}}$, and is given by the antisymmetric combination

$$\frac{1}{\sqrt{n_{\rm e}!}}\sum_P (-1)^P \, |n_{\rm p}\ell m_{P1} m_{sP1}\rangle_1 \cdots |n_{\rm p}\ell m_{Pn_{\rm e}} m_{sPn_{\rm e}}\rangle_{n_{\rm e}}\,, \tag{1.107}$$

where P is a permutation of $1,\ldots,n_{\rm e}$, $(-1)^P$ is the sign of P, and $|\cdot\rangle_i$ describes the state of the i-th electron. Notice that the single electron states in sub-shell $n_{\rm p}\ell$ all have the same radial wave function.

The difference between the true interaction Hamiltonian and the self-consistent field, which contains the electrostatic interaction between the electrons, the spin-orbit coupling, and the crystal field energy, is treated as a perturbation. It lifts the degeneracy of the $n_{\rm p}\ell$ sub-shell. The way in which the $n_{\rm p}\ell$ sub-shell is split into energy eigenstates depends on which term of the perturbations dominates. Usually, the electrostatic energy is much higher than the spin-orbit coupling and than the crystal field energy. In this case the perturbation Hamiltonian at first order does not depend on the spin and, given that it is rotationally symmetric, commutes with the total orbital angular momentum (and with the total spin, obviously). Hence, the splitting of sub-shell $n_{\rm p}\ell$ can be characterized by the four quantum numbers L, M_L, S, M_S, corresponding to total orbital angular momentum, z component of total orbital angular momentum, total spin, and total spin z component[6], in addition to $n_{\rm p}\ell$. This is called the Russell-Saunders, or LS, spin-orbit coupling scheme, which we assume in the following.

The completely filled sub-shells have no net orbital angular momentum and no net spin, and thus do not contribute to the magnetic moment. Analogously, paired electrons, which combine their orbital angular momentum

[6]Notice that the electrostatic energy operator commutes with the spin of each electron separately (but not with the single electron orbital angular momentum). At first sight, it seems that the multi-electron states can be characterized by the single electron spins, not just by the total spin. However, the individual spins are not observables since the electrons are indistinguishable, and the single electron spin states are not good quantum numbers. Indeed, the single electron spin states are mixed in the antisymmetrization process, as can be seen in equation (1.107).

and their spin in such a way that both cancel, do not contribute to the magnetic moment. Consider then an ion with $n_{\rm u}$ unpaired electrons occupying a partially filled sub-shell $n_{\rm p}\ell$. These electrons are described by an LS state, $|n_{\rm p}\ell LSM_LM_S\rangle$, which is an anitsymmetric linear combination of states of the form

$$|n_{\rm p}\ell m_1 m_{s1}\rangle_1 \cdots |n_{\rm p}\ell m_{n_{\rm u}} m_{s\,n_{\rm u}}\rangle_{n_{\rm u}} \tag{1.108}$$

From now on we drop the quantum number $n_{\rm p}$ from the expressions, and we will write the radial wave function as $f(r)$. Let us stress that in general there are many ways of combining $n_{\rm u}$ orbital angular momentum and spin into ℓLS multiplets. This means there are many LS multiplets in $n\ell$ subshell that can be occupied by $n_{\rm u}$ electrons. Which one is occupied is decided by the minimization of the electrostatic repulsion between the electrons.

At this level of approximation, an LS state is $(2L+1)(2S+1)$ fold degenerate. This degeneracy is lifted by the remaining interactions. If the spin-orbit coupling dominates over the crystal field energy, rotational symmetry is preserved and then the states are split into multiplets characterized by the magnitude and z component of the total angular momentum operator, J and M, respectively. Thus the states are written as $|\ell LSJM\rangle$, and it remains a $2J+1$ degeneracy, due to the rotational symmetry of the isolated ion, which is removed by the crystal field interaction. These states are of course given by appropriate linear combinations of states of the form (1.108), If, on the contrary, the crystal field dominates over the spin-orbit coupling, the $(2L+1)(2S+1)$ degeneracy may be completely lifted and in this case the expectation value of the three components of the orbital angular momentum vanish, so that they do not contribute to the expectation value of the magnetic moment, which is entirely due to spin. In this case, it is said that the orbital angular momentum is *quenched*.

Usually, the energy differences between different LS multiplets are of the order of 1 eV or higher and thus neutrons with energies in the thermal range cannot induce transtions between them. This is an important point, since in these cases the neutron interaction can only change the values of M_L and M_S, that is, the ion spatial orientation. Hence, we have to consider only the matrix elements of $\vec{\mathcal{M}}^{(n)}_{\perp\vec{q}}$ between the states of the same LS multiplet, with constant L and S (and of course constant $n_{\rm p}$ and ℓ). Evidently, the matrix element of $\vec{\mathcal{M}}^{(nj)}_{\perp\vec{q}}$ is a linear combination of single particle matrix elements,

$$\langle \ell m' m'_{\rm s}|\, \vec{\mathcal{M}}^{(nj)}_{\perp\vec{q}}\, |\ell m m_{\rm s}\rangle\,. \tag{1.109}$$

The contribution of filled shells or paired electrons cancel and we have to consider only the contribution of unpaired electrons. Since the electrons are indistinguishable, the single electron matrix element (1.109) does not depend on j. To avoid heavy notation, from now on we drop the indices nj from the expressions and we denote by $\vec{r}$ the electron coordinate with respect to the center of the ion.

Let us consider first the contribution to (1.109) of the orbital part of $\vec{\mathcal{M}}^{(nj)}_{\perp\vec{q}}$. Since it does not depend on spin, we get an overall factor $\delta_{m_{\rm s}m'_{\rm s}}$. It remains

$$\langle \ell m'|\, \mathrm{e}^{\mathrm{i}2\pi\vec{q}\cdot\vec{r}}(\hat{q}\times\nabla)\,|\ell m\rangle = \int d^3r f(r) \mathrm{Y}_\ell^{m'*}(\hat{r}) \mathrm{e}^{\mathrm{i}2\pi\vec{q}\cdot\vec{r}}(\hat{q}\times\nabla) f(r) \mathrm{Y}_\ell^{m}(\hat{r}). \quad (1.110)$$

Let us give only a few hints about how to compute this, in order to recognize the origin of some factors entering the magnetic cross section, mainly the *magnetic form factor*. A thorough analysis with many detailed calculations can be found in the book of Lovesey [14]. First, notice that by integrating by parts and using the fact that $(\hat{q}\times\nabla)\exp(\mathrm{i}2\pi\vec{q}\cdot\vec{r}) = 0$, we can remove the derivative from the radial function $f(r)$. We get

$$\begin{aligned}\langle \ell m'|\, \mathrm{e}^{\mathrm{i}2\pi\vec{q}\cdot\vec{r}}(\hat{q}\times\nabla)\,|\ell m\rangle = \frac{1}{2}\int d^3r f^2(r) \mathrm{e}^{\mathrm{i}2\pi\vec{q}\cdot\vec{r}} \Big[&\mathrm{Y}_\ell^{m'*}(\hat{r})(\hat{q}\times\nabla)\mathrm{Y}_\ell^{m}(\hat{r}) \\ &- \mathrm{Y}_\ell^{m}(\hat{r})(\hat{q}\times\nabla)\mathrm{Y}_\ell^{m'*}(\hat{r})\Big].\end{aligned} \quad (1.111)$$

The derivative acts now only on the angular part of the wave function. We can extract a factor $1/r$ by defining $\hat{\nabla}$ so that $\nabla = (1/r)\hat{\nabla}$.

The spherical symmetry of the single electron wave functions makes it convenient to exploit the algebra of spherical tensors, working in terms of the spherical components of $\hat{q}\times\hat{\nabla}$, which is a vector operator[7]. We also expand the plane wave state $\exp(\mathrm{i}2\pi\vec{q}\cdot\vec{r})$ in the basis of spherical waves as

$$\mathrm{e}^{\mathrm{i}2\pi\vec{q}\cdot\vec{r}} = 4\pi \sum_{L=0}^{\infty}\sum_{M=-L}^{L} \mathrm{i}^L j_L(2\pi q r) \mathrm{Y}_L^M(\hat{r}) \mathrm{Y}_L^{M*}(\hat{q}), \quad (1.112)$$

where $j_L(x)$ is the spherical Bessel function of order L. Inserting this expansion into (1.111), in which we take the M'-th spherical component, we get

$$\begin{aligned}&\langle \ell m'|\, \mathrm{e}^{\mathrm{i}2\pi\vec{q}\cdot\vec{r}}(\hat{q}\times\nabla)_{M'}\,|\ell m\rangle = \\ &2\pi \sum_{L=0}^{\infty}\sum_{M=-L}^{L} \mathrm{i}^L \mathrm{Y}_L^{M*}(\hat{q}) \int dr r^2 \frac{1}{r} f^2(r) j_L(2\pi q r) I^{\ell m m'}_{M' L M}(\hat{q}),\end{aligned} \quad (1.113)$$

where

$$I^{\ell m m'}_{M' L M}(\hat{q}) = \int d^2\hat{r}\, \mathrm{Y}_L^M \left[\mathrm{Y}_\ell^{m'\,*}(\hat{q}\times\hat{\nabla})_{M'} \mathrm{Y}_\ell^{m} - \mathrm{Y}_\ell^{m}(\hat{q}\times\hat{\nabla})_{M'} \mathrm{Y}_\ell^{m'\,*} \right] \quad (1.114)$$

is an angular integral, with $d^2\hat{r} = \sin\theta d\theta d\varphi$. The $1/r$ factor in the radial integral comes from the definition of $\hat{\nabla}$ given above.

[7] Let us recall that the spherical components of a vector operator $\vec{V}$ are denoted by V_M, with $M = -1, 0, 1$, and defined as $V_{\pm1} = \mp(V_x \pm \mathrm{i}V_y)/\sqrt{2}$ and $V_0 = V_z$.

The angular integral can be evaluated straightforwardly using properties of spherical tensor operators. It gives rather complicated, and not very illuminating, linear combination of the spherical harmonics of $Y_L^M(\hat{q})$, with coefficients that are linear combinations of products of Clebsch-Gordan coefficients. Its product with the spherical harmonics entering (1.113) can be again reduced to a linear combination of simple spherical harmonics.

For the radial part we use the relation

$$j_L(x) = \frac{x}{2L+1}\left[j_{L-1}(x) + j_{L+1}(x)\right], \tag{1.115}$$

and the definition

$$\bar{J}_L(q) = \int dr r^2 f^2(r) j_L(2\pi q r), \tag{1.116}$$

and we can write the expression

$$\langle \ell m' | \mathrm{e}^{\mathrm{i}2\pi\vec{q}\cdot\vec{r}}(\hat{q}\times\nabla)_M | \ell m\rangle = 4\pi^2 q \sum_{L=1}^{\infty} \frac{\mathrm{i}^L}{2L+1}(\bar{J}_{L-1} + \bar{J}_{L+1}) C_L(\hat{q}), \tag{1.117}$$

where $C_L(\hat{q})$ is a linear combination of spherical harmonics. For the spin part, the computation is similar. One difference is that there is no gradient term, hence the $1/r$ factor is absent in the radial integral and only a single $\bar{J}_L$ comes from the radial part.

Therefore, the matrix element of the M-th spherical component of $\vec{\mathcal{M}}^{(n)}_{\mathrm{L}\perp\vec{q}}$ between LSJ states has the form

$$\langle \ell LSJM'_J | \, \mathcal{M}^{(n)\,M}_{\mathrm{L}\perp\vec{q}} \, | \ell LSJM_J\rangle = \sum_{L'=1}^{\infty} (\bar{J}_{L'-1} + \bar{J}_{L'+1}) A_{L'}(\hat{q}) \tag{1.118}$$

$$\langle \ell LSJM'_J | \, \mathcal{M}^{(n)\,M}_{\mathrm{S}\perp\vec{q}} \, | \ell LSJM_J\rangle = \sum_{L'=0}^{\infty} \bar{J}_{L'} B_{L'}(\hat{q}) \tag{1.119}$$

where the coefficients $A_{L'}$ and $B_{L'}$ obviously also depend on ℓ, L, S, J, M_J, M'_J, and M, and, we stress it again, are linear combinations of spherical harmonics. The symmetries of the Clebsch-Gordan coefficients imply that they vanish for sufficiently large L', so that the sums are in practice finite and suitable for numerical computations. It is however interesting to simplify $A_{L'}$ and $B_{L'}$ by making some approximation that provide more physical insight than expressions (1.118) and (1.119). This is the aim of the *dipole approximation*.

Dipole approximation

The dipole approximation is obtained by truncating of the sums in (1.118) and (1.119) to $L' \leq 1$ and keeping in $A_{L'}$ and $B_{L'}$ only the spherical harmonics $Y_{L''}^{M''}$ with $L'' \leq 2$ [15]. It can be shown that, in the dipole approximation,

the matrix elements of $\vec{\mathcal{M}}^{(n)}_{\vec{q}}$ between $LSJM_J$ states are equal to the matrix elements of the operator

$$\vec{\mathcal{M}}^{(n,\mathrm{D})}_{\vec{q}} = -\mu_\mathrm{B}\left\{\left[\bar{J}_{0n}(q)+\bar{J}_{2n}(q)\right]\vec{\mathbb{L}}_n + 2\bar{J}_{0n}(q)\,\vec{\mathbb{S}}_n\right\}, \tag{1.120}$$

where $\vec{\mathbb{L}}_n$ and $\vec{\mathbb{S}}_n$ are the total orbital angular momentum operator and the total spin operator, respectively, for the n-th ion. According to the Wigner-Eckart theorem, all vector operators are proportional to each other, and, therefore, to the total angular momentum operator $\vec{\mathbb{J}}$, on a given $|LSJM_J\rangle$ subspace. Consequently, if the total angular momentum is approximately conserved, so that J and M are good quantum numbers, as it happens in the case of rare earth ions, we have

$$\vec{\mathcal{M}}^{(n,\mathrm{D})}_{\vec{q}} = -\mu_\mathrm{B} g_n F_n(q)\vec{\mathbb{J}}_n, \tag{1.121}$$

where g_n is the Landé factor of the n-th ion,

$$g_n = 1 + \frac{J_n(J_n+1) - L_n(L_n+1) + S_n(S_n+1)}{2J_n(J_n+1)}, \tag{1.122}$$

and the magnetic form factor for the n-th ion is given by

$$F_n(q) = \bar{J}_{0n}(q) + \frac{J_n(J_n+1) + L_n(L_n+1) - S_n(S_n+1)}{3J_n(J_n+1) + L_n(L_n+1) - S_n(S_n+1)}\bar{J}_{2n}(q). \tag{1.123}$$

In the case of transition metal ions, the crystal field removes the degeneracy in the total orbital angular momentum, mixing states with different M_L quantum numbers, although it preserves the degeneracy in the spin quantum number M_S, since the crystal field Hamiltonian is independent of the spin. Hence, S and M_S remain good quantum numbers. If the degeneracy in the M_L quantum numbers is completely lifted, it can be easily shown that the expectation value of the total orbital angular momentum operator, $\vec{\mathbb{L}}$, does vanish in these states. As we said before, this phenomenon is called the *quenching* of the orbital angular momentum. And, since the neutron does not have enough energy to overcome the crystal field splitting energy, the only matrix element of $\vec{\mathbb{L}}$ that contributes to the magnetic neutron scattering vanishes. Hence, the scattering is only due to spin, and the magnetization operator is given by

$$\vec{\mathcal{M}}^{(n,\mathrm{D})}_{\vec{q}} = -\mu_\mathrm{B} 2\bar{J}_{0n}(q)\,\vec{\mathbb{S}}_n. \tag{1.124}$$

Actually, the spin-orbit interaction couples the states split by the crystal field and the quenching of the orbital angular momentum is not complete. In that case, $\vec{\mathbb{L}}$ is proportional to $\vec{\mathbb{S}}$ in the ground state subspace, so that $\vec{\mathbb{L}} = (g-2)\vec{\mathbb{S}}$, with g close to 2, and we have

$$\vec{\mathcal{M}}^{(n,\mathrm{D})}_{\vec{q}} = -\mu_\mathrm{B} g_n F_n(q)\,\vec{\mathbb{S}}_n, \tag{1.125}$$

with

$$F_n(q) = \frac{1}{g_n}\left[g_n \bar{J}_{0n}(q) + (g_n - 2)\bar{J}_{2n}(q)\right]. \tag{1.126}$$

The dipole approximation is valid at low q. The spherical Bessel functions $j_L(x)$ vanishes as $x \to 0$ as x^L, and therefore for $q \to 0$ we have $\bar{J}_L(q) \sim (q r_{\max})^L$, where $r_{\max}$ is the maximum of the radial function, $f(r)$, which is proportional to the Bohr radius. Then, the dipole approximation is justified if q is small in comparison to $1/r_{\max}$.

Magnetic scattering cross section in the dipole approximation

The explicit form of the matrix elements of $\vec{\mathcal{M}}_{\perp\vec{q}}$ can be obtained from (1.102) with the dipole approximation for $\vec{\mathcal{M}}^{(n)}_{\vec{q}}$, using the equations (1.121) or (1.125), depending on the case. To be generic, we write

$$\vec{\mathcal{M}}^{(n,\mathrm{D})}_{\vec{q}} = F_n(q)\,\vec{\mathbb{M}}_n, \tag{1.127}$$

where $\vec{\mathbb{M}}_n$ denotes the n-th ion magnetic moment density operator, which is given by $-\mu_{\mathrm{B}} g_n$ times either the total angular momentum operator or the total spin operator, depending on the case. $F_n(q)$ and g_n are the corresponding *magnetic form factor* and *Landé factor*, respectively of the n-th ion.

From the general equation (1.84) and the definition (1.102) we inmediately get

$$\left(\frac{d^2\sigma^{(\mathrm{m})}}{d\Omega_{\vec{k}_f} dE_f}\right)_{\sigma_f} = p^2 \frac{k_f}{k_i} \sum_{\alpha\beta} \rho^i_{\alpha\beta}(\sigma_f) \times \sum_{nn'} F^*_n(q) F_{n'}(q) \left\langle \mathrm{e}^{-\mathrm{i}2\pi\vec{q}\cdot\vec{R}_n(0)} \mathrm{e}^{\mathrm{i}2\pi\vec{q}\cdot\vec{R}_{n'}(t)} \mathbb{M}^{\beta\,\dagger}_{n\perp\vec{q}}(0) \mathbb{M}^{\alpha}_{n'\perp\vec{q}}(t) \right\rangle_\nu. \tag{1.128}$$

The magnetic moment dynamics and the nuclear dynamics are weakly coupled, so that to a good approximation the time-dependent correlation function in (1.128) factorizes into nuclear and magnetic moment factors, and we can write

$$\left(\frac{d^2\sigma^{(\mathrm{m})}}{d\Omega_{\vec{k}_f} dE_f}\right)_{\sigma_f} = p^2 \frac{k_f}{k_i} \sum_{\alpha\beta} \rho^i_{\alpha\beta}(\sigma_f) \sum_{nn'} F^*_n(q) F_{n'}(q) \times \int \frac{dt}{h} \mathrm{e}^{-\mathrm{i}2\pi\nu t} \left\langle \mathrm{e}^{-\mathrm{i}2\pi\vec{q}\cdot\vec{R}_n(0)} \mathrm{e}^{\mathrm{i}2\pi\vec{q}\cdot\vec{R}_{n'}(t)} \right\rangle \left\langle \mathbb{M}^{\beta\,\dagger}_{n\perp\vec{q}}(0) \mathbb{M}^{\alpha}_{n'\perp\vec{q}}(t) \right\rangle. \tag{1.129}$$

1.3 Neutron scattering by a crystal

Let us consider now the specific case of diffraction by a crystalline material. Let us define a crystal by its unit cell $(\vec{a}, \vec{b}, \vec{c})$ and the atoms contained in it,

labelled by $d = 1, \ldots, N_{\rm uc}$. The reciprocal lattice is generated by the basis $(\vec{a}^*, \vec{b}^*, \vec{c}^*)$, defined as usually in crystallography as

$$\vec{a}^* = \frac{(\vec{b} \times \vec{c})}{V}, \qquad \vec{b}^* = \frac{(\vec{c} \times \vec{a})}{V}, \qquad \vec{c}^* = \frac{(\vec{a} \times \vec{b})}{V}, \tag{1.130}$$

where $V = (\vec{a} \times \vec{b}) \cdot \vec{c}$ is the volume of the direct lattice unit cell. We denote by $\vec{H}$ a node of the reciprocal lattice with $\vec{H} = h\,\vec{a}^* + k\,\vec{b}^* + l\,\vec{c}^*$, where h, k, l are integer numbers (the Miller indices).

1.3.1 Nuclear scattering

The coherent scattering cross section can be obtained by applying the general results for solids obtained in section 1.2.4, taking into account that the equilibrium position of an atom can be written as $\vec{R}^{\rm e}_{ld} = \vec{R}_l + \vec{r}_d$, where $\vec{R}_l = l_a\vec{a} + l_b\vec{b} + l_c\vec{c}$, with l_a, l_b, and l_c integers, represents the position of the origin of the l-th cell, and $\vec{r}_d$ is the position of d-th atom relative to the origin of coordinates of the unit cell. Then, we have to substitute the summation in n entering the equations of section 1.2.4 by summations in l and d.

For the coherent elastic scattering, given by equation (1.61), we have to compute

$$\Big| \sum_n b_n \langle {\rm e}^{{\rm i}2\pi\vec{q}\cdot\vec{R}_n} \rangle \Big|^2 = \sum_{l,\,l'} {\rm e}^{{\rm i}2\pi\vec{q}(\vec{R}_{l'} - \vec{R}_l)} |N_{\vec{q}}|^2 \tag{1.131}$$

where

$$N_{\vec{q}} = \sum_d^{N_{\rm uc}} b_d\, T_d(\vec{q})\, {\rm e}^{{\rm i}2\pi\vec{q}\cdot\vec{r}_d} \tag{1.132}$$

is the so called *nuclear structure factor* of the unit cell and $N_{\rm uc}$ is the number of atoms inside it. Using the Poisson summation formula

$$\sum_{l,\,l'} {\rm e}^{{\rm i}2\pi\vec{q}\cdot(\vec{R}_{l'} - \vec{R}_l)} = \frac{N_{\rm c}}{V} \sum_{\vec{H}} \delta(\vec{q} - \vec{H}), \tag{1.133}$$

where $N_{\rm c}$ is the number of cristal unit cells in the system, we obtain

$$\frac{d\sigma^{({\rm n,\,e})}_{\rm coh}}{d\Omega_{\hat{k}_f}} = \frac{N_{\rm c}}{V} \sum_{\vec{H}} \delta(\vec{q} - \vec{H}) |N_{\vec{q}}|^2. \tag{1.134}$$

The above expression tells us that the scattered neutrons will follow directions such a way that $\vec{q} = \vec{H}$, *i.e.* the Bragg reflection will occurs only when the scattering vectors correspond to the nodes of the reciprocal lattice. These nodes are related to the characteristic distances between crystal planes (d_{hkl}) at the direct space. The amount of neutrons scattered for each

of these directions is proportional to the modulus square of the complex number $N_{\vec{H}}$, the *nuclear structure factor* evaluated at $\vec{q} = \vec{H}$.

Sometimes it is convenient to define the atoms of the crystal unit cell through the number of atoms in its asymmetric unit cell ($N_{\rm au}$), each one indexed with d, with coherent scattering length b_d, and located at $\vec{r}_d$. Let $\tilde{g}_p = \{\mathcal{R}_p|\vec{t}_p\}$ be the elements of the space group of the crystal ($\tilde{g}_p \in \mathcal{G}$), with rotational and translational parts, respectively, $\mathcal{R}_p$, and $\vec{t}_p$. The d-orbit in the unit cell is defined by the atoms at the p-site related to the d-site by $\vec{r}_p = \tilde{g}_p \vec{r}_d$. The number of atoms on a given orbit is less or equal than the order of the group $\mathcal{G}$, and all of them have the same scattering length b_d. The position of the same atom d at another unit cell, l, is $\vec{R}_{ld} = \vec{R}_l + \vec{r}_d$. The nuclear structure factor in (1.132) is rewritten as

$$N_{\vec{q}} = \sum_{d}^{N_{\rm au}} b_d \sum_{p}^{d-orbit} T_{pd}(\vec{q}) \mathrm{e}^{\mathrm{i}2\pi \vec{q}\cdot\tilde{g}_p\vec{r}_d}, \tag{1.135}$$

where $\vec{q}$ labels the nuclear Bragg reflexion ($\vec{q} = \vec{H}$) and p runs over the symmetry operators of the space group of the crystal that generates the atoms of the d-orbit. The factor $T_{pd}(\vec{q})$ is the Debye-Waller factor of the d-th atom at its equivalent position p. In the harmonic approximation, it is given by

$$T_{pd}(\vec{q}) = \mathrm{e}^{-\vec{q}\cdot\mathcal{R}_p\tilde{\beta}_d\mathcal{R}_p^{\dagger}\vec{q}}. \tag{1.136}$$

The elastic incoherent cross section by a crystal is immediately obtained from equation (1.62) by summing on all the atoms at the unit cell or by summing first on the asymmetric unit and then on each d-orbit (p)

$$\frac{d\sigma_{\rm inc}^{(\rm n,\,e)}}{d\Omega_{\hat{k}_f}} = N_{\rm c}\sum_{d}^{N_{\rm uc}} b_{{\rm inc},d}^2 |T_d(\vec{q})|^2 = N_{\rm c}\sum_{d}^{N_{\rm au}} b_{{\rm inc},d}^2 \sum_{p}^{d-orbit} |T_{pd}(\vec{q})|^2. \tag{1.137}$$

Scattering by Phonons

The coherent inelastic 1-phonon scattering by a crystal can be readily obtained from the general equation (1.74), setting $\vec{R}_{ld}^{\,\rm e} = \vec{R}_l + \vec{r}_d$, and taking into account that, due to the lattice translational symmetry, the phonons r are characterized by a wave vector, $\vec{p}$, which belongs to the first Brillouin zone in reciprocal space, and a branch index, s. The number of branches is equal to the number of atoms in the unit cell. The polarization vector is given by [16]

$$\vec{\xi}_{s,ld}(\vec{p}) = \frac{1}{\sqrt{N_{\rm c}}}\,\mathrm{e}^{\mathrm{i}2\pi\vec{p}\cdot\vec{R}_l}\,\vec{e}_{s,d}(\vec{p}), \tag{1.138}$$

and thus $\vec{v}_r(\vec{q})$, defined by equation (1.75), reads

$$\vec{v}_{s\vec{p}}(\vec{q}) = \frac{1}{\sqrt{N_{\rm c}}}\sum_{ld}\mathrm{e}^{\mathrm{i}2\pi\vec{q}\cdot\vec{R}_l}\,\mathrm{e}^{\mathrm{i}2\pi\vec{q}\cdot\vec{r}_d}\frac{b_d}{\sqrt{M_d}}\,T_d(\vec{q})\,\vec{e}_{s,d}(\vec{p}). \tag{1.139}$$

Inserting this into equation (1.74) and using (1.133), we obtain

$$\frac{d^2\sigma^{(\mathrm{n,i})}_{\mathrm{coh,1ph}}}{d\Omega_{\hat{k}_f}dE_f} = \frac{k_f}{k_i}q^2\frac{(2\pi)^2}{2V}\sum_{s,\vec{p}}\Big|\sum_d \frac{b_d}{\sqrt{M_d}}T_d(\vec{q})\mathrm{e}^{\mathrm{i}2\pi\vec{q}\cdot\vec{r}_d}\hat{q}\cdot\vec{e}_{s,d}(\vec{q})\Big|^2\times \\ \frac{1}{\nu_{s\vec{p}}}\sum_{\vec{H}}\Big[\delta(\vec{q}-\vec{p}-\vec{H})\delta(h\nu-h\nu_{s\vec{p}})\big(1+\langle n_{s\vec{p}}\rangle\big) \\ +\delta(\vec{q}+\vec{p}-\vec{H})\delta(h\nu+h\nu_{s\vec{p}})\langle n_{s\vec{p}}\rangle\Big]. \tag{1.140}$$

This equation provides a method to measure the *phonon dispersion relation*, that is, the phonon frequency as a function of its wave vector, for each branch. The technique is as follows. A monochromatic beam, with fixed wave vector $\vec{k}_i$ is scattered by a single crystal, and the intensity of the scattered beam is measured at a fixed direction, $\hat{k}_f$, as a function of the neutron energy E_f (or as a function of wave number, k_f). The Dirac delta functions of (1.140) impose severe constraints to the scattering: for given k_f, there will be a discrete set of phonon wave vectors, that will satisfy the constraint imposed by the wave vector Dirac delta function, namely, those that differ from the scattering vector by a reciprocal lattice vector: $\vec{p}=\vec{k}_i-\vec{k}_f+\vec{H}$. But then, in general, none of the frequencies $\nu_{s\vec{p}}$ will satisfy the constraint imposed by the frequency Dirac delta functions: $\nu_{s\vec{p}}\neq|E_i-E_f|/h$, since the index s is discrete. It is only for specific values of k_f that both constraints will be satisfied: sharp intensity peaks will appear only if $\vec{p}=\vec{k}_i-\vec{k}_f+\vec{H}$ and $\nu_{s\vec{p}}=|E_i-E_f|/h$. These peaks provide the phonon dispersion relations. The polarization vectors can be obtained from the intensities of the peaks. Neutron instruments suitable to measure the phonon dispersion relations are the *triple axis* and *time-of-flight* spectrometers.

The expression for the inelastic scattering is not sensitive to the atom arrangements and thus it is given by (1.74).

1.3.2 Magnetic scattering

If some of the ions in the unit cell have localized unpaired electrons, the neutrons suffer magnetic scattering. Let d_{m} label the magnetic ions within a cell. The position of the ld_{m} ion is given by $\vec{R}_l+\vec{r}_{d_{\mathrm{m}}}+\vec{u}_{ld_{\mathrm{m}}}$, where $\vec{u}_{ld_{\mathrm{m}}}$ is the quantum operator that describe the displacements from the equilibrium position. The magnetic form factors depend only on d_{m}, and not on the cell to which the ion belongs. We have to substitute the sums in n and n' in equation (1.129) by sums in ld_{m} and $l'd'_{\mathrm{m}}$. We obtain

$$\left(\frac{d^2\sigma^{(\mathrm{m})}}{d\Omega_{\hat{k}_f}dE_f}\right)_{\sigma_f} = p^2\frac{k_f}{k_i}\sum_{\alpha\beta}\rho^i_{\alpha\beta}(\sigma_f)\sum_{ld_{\mathrm{m}}l'd'_{\mathrm{m}}}\mathrm{e}^{\mathrm{i}2\pi\vec{q}\cdot(\vec{R}_{l'}-\vec{R}_l)}\mathrm{e}^{\mathrm{i}2\pi\vec{q}\cdot(\vec{r}_{d'_{\mathrm{m}}}-\vec{r}_{d_{\mathrm{m}}})}F^*_{d_{\mathrm{m}}}(q)F_{d'_{\mathrm{m}}}(q) \\ \int\frac{dt}{h}\mathrm{e}^{-\mathrm{i}2\pi\nu t}\Big\langle\mathrm{e}^{-\mathrm{i}2\pi\vec{q}\cdot\vec{u}_{ld_{\mathrm{m}}}(0)}\mathrm{e}^{\mathrm{i}2\pi\vec{q}\cdot\vec{u}_{l'd'_{\mathrm{m}}}(t)}\Big\rangle\Big\langle\mathbb{M}^{\beta\,\dagger}_{ld_{\mathrm{m}}\perp\vec{q}}(0)\mathbb{M}^{\alpha}_{l'd'_{\mathrm{m}}\perp\vec{q}}(t)\Big\rangle. \tag{1.141}$$

The elastic scattering component is extracted from the factorization of the time correlations in the $t \to \infty$ limit. Defining the vector $\vec{M}_{ld_\mathrm{m}} = \langle \vec{\mathbb{M}}_{ld_\mathrm{m}} \rangle$, which is real, and denoting by $\vec{M}_{ld_\mathrm{m}\perp\vec{q}}$ its component perpendicular to $\vec{q}$, we have

$$\left(\frac{d\sigma^{(\mathrm{m,e})}}{d\Omega_{\hat{k}_f}}\right)_{\sigma_f} = p^2 \sum_{\alpha\beta} \rho^i_{\alpha\beta}(\sigma_f) \sum_{ld_\mathrm{m}l'd'_\mathrm{m}} \mathrm{e}^{\mathrm{i}2\pi\vec{q}\cdot(\vec{R}_{l'}-\vec{R}_l)} \times \\ \mathrm{e}^{-\mathrm{i}2\pi\vec{q}\cdot\vec{r}_{d_\mathrm{m}}} T^*_{d_\mathrm{m}}(\vec{q}) F^*_{d_\mathrm{m}}(\vec{q}) \mathrm{e}^{\mathrm{i}2\pi\vec{q}\cdot\vec{r}_{d'_\mathrm{m}}} T_{d'_\mathrm{m}}(\vec{q}) F_{d'_\mathrm{m}}(\vec{q}) M^{\beta\,*}_{ld_\mathrm{m}\perp\vec{q}} M^{\alpha}_{ld_\mathrm{m}\perp\vec{q}}. \tag{1.142}$$

Notice that, in the most general case, $\vec{M}_{ld_\mathrm{m}}$ need not be commensurate with the nuclear lattice, but it can always be expanded in Fourier series as

$$\vec{M}_{ld_\mathrm{m}} = \sum_{\{\vec{K}\}} \vec{S}_{\vec{K}d_\mathrm{m}} \mathrm{e}^{-\mathrm{i}2\pi\vec{K}\cdot\vec{R}_l}, \tag{1.143}$$

where the complex vectors $\vec{S}_{\vec{K}d_\mathrm{m}}$ are the *Fourier coefficients* and $\{\vec{K}\}$ are the set of *propagation vectors*. The propagation vectors relate the magnetic moment at the l-th unit cell with respect to the zero-th unit cell. In the case of $\vec{K} = 0$, which means that the nuclear and magnetic periodicity are the same, then the Fourier coefficients, $\vec{S}_{\vec{K}d_\mathrm{m}}$ are equal to the magnetic moment, $\vec{M}_{d_\mathrm{m}}$, at site d_m, and do not depend on the lattice index l.

Moreover, because the magnetic moment $\vec{M}_{ld_\mathrm{m}}$ must be a real vector, it imposes the condition that summation extends to pairs of propagation vectors $\vec{K}$ and $-\vec{K}$ and the relation $\vec{S}_{-\vec{K}d_\mathrm{m}} = \vec{S}^*_{\vec{K}d_\mathrm{m}}$ between the Fourier coefficients.

Inserting expansion (1.143) into (1.142) and using equation (1.133) for the sum in $l\,l'$, we get

$$\frac{d\sigma^{(\mathrm{m,\,e})}_{\mathrm{coh}}}{d\Omega_{\hat{k}_f}} = \frac{N_\mathrm{c}}{V} \sum_{\vec{H}\vec{K}} \delta(\vec{q} - \vec{H} - \vec{K})\, |\vec{M}_{\perp\vec{q}}|^2, \tag{1.144}$$

where we have defined the *magnetic interaction vector*, $\vec{M}_{\perp\vec{q}}$, and the *magnetic structure factor*, $\vec{M}_{\vec{q}\vec{K}}$, for the crystal unit cell[8] as;

$$\vec{M}_{\perp\vec{q}} = \hat{q} \times (\vec{M}_{\vec{q}\vec{K}} \times \hat{q}), \tag{1.145}$$

$$\vec{M}_{\vec{q}\vec{K}} = p \sum_{d_\mathrm{m}}^{N_\mathrm{uc}} F_{d_\mathrm{m}}(\vec{q}) T_{d_\mathrm{m}}(\vec{q})\ \mathrm{e}^{\mathrm{i}2\pi\vec{q}\cdot\vec{r}_{d_\mathrm{m}}} \vec{S}_{\vec{K}d_\mathrm{m}}. \tag{1.146}$$

To have elastic magnetic scattered neutrons (magnetic Bragg peaks) the Dirac delta in (1.144) impose that the scattering vector must fulfill the

[8] Other authors define the magnetic structure factor for the crystal by keeping the sum on the unit cells, l and l', in equation (1.142) in its definition.

condition $\vec{q} = \vec{H} \pm \vec{K}$ ($\vec{H}$ is a node of the nuclear reciprocal lattice and $\vec{K}$ is the magnetic propagation vector).

The intensity of magnetic peaks is very sensitive to temperature, since the expectation value of the magnetic moment, $\vec{M}_{ld_\mathrm{m}}$ is. By increasing temperature $\vec{M}_{\vec{q}\vec{K}}$ decreases until it vanishes above the magnetic ordering temperature, in which case only the nuclear peaks survive. The behavior with temperature is one way of distinguishing magnetic and nuclear scattering.

Magnetic inelastic scattering

To discuss magnetic inelastic scattering it is convenient to introduce more notation. Let us define

$$N_\mathrm{E} = \left\langle \mathrm{e}^{-\mathrm{i}2\pi\vec{q}\cdot\vec{u}_{ld_\mathrm{m}}} \right\rangle \left\langle \mathrm{e}^{\mathrm{i}2\pi\vec{q}\cdot\vec{u}_{l'd'_\mathrm{m}}} \right\rangle, \quad M^{\alpha\beta}_\mathrm{E} = \left\langle \mathbb{M}^{\alpha\,\dagger}_{ld_\mathrm{m}\perp\vec{q}} \right\rangle \left\langle \mathbb{M}^{\beta}_{l'd'_\mathrm{m}\perp\vec{q}} \right\rangle, \tag{1.147}$$

and

$$N_\mathrm{I} = \left\langle \mathrm{e}^{-\mathrm{i}2\pi\vec{q}\cdot\vec{u}_{ld_\mathrm{m}}(0)} \mathrm{e}^{\mathrm{i}2\pi\vec{q}\cdot\vec{u}_{l'd'_\mathrm{m}}(t)} \right\rangle - \left\langle \mathrm{e}^{-\mathrm{i}2\pi\vec{q}\cdot\vec{u}_{ld_\mathrm{m}}} \right\rangle \left\langle \mathrm{e}^{\mathrm{i}2\pi\vec{q}\cdot\vec{u}_{ld_\mathrm{m}}} \right\rangle, \tag{1.148}$$

$$M^{\alpha\beta}_\mathrm{I} = \left\langle \mathbb{M}^{\alpha\,\dagger}_{ld_\mathrm{m}\perp\vec{q}}(0) \mathbb{M}^{\beta}_{l'd'_\mathrm{m}\perp\vec{q}}(t) \right\rangle - \left\langle \mathbb{M}^{\alpha\,\dagger}_{ld_\mathrm{m}\perp\vec{q}} \right\rangle \left\langle \mathbb{M}^{\beta}_{l'd'_\mathrm{m}\perp\vec{q}} \right\rangle. \tag{1.149}$$

The integrand of the time integral in equation (1.141) is split into four terms

$$\begin{gathered} \left\langle \mathrm{e}^{-\mathrm{i}2\pi\vec{q}\cdot\vec{u}_{ld_\mathrm{m}}(0)} \mathrm{e}^{\mathrm{i}2\pi\vec{q}\cdot\vec{u}_{l'd'_\mathrm{m}}(t)} \right\rangle \left\langle \mathbb{M}^{\alpha\,\dagger}_{ld_\mathrm{m}\perp\vec{q}}(0) \mathbb{M}^{\beta}_{l'd'_\mathrm{m}\perp\vec{q}}(t) \right\rangle = \\ N_\mathrm{I} M^{\alpha\beta}_\mathrm{I} + N_\mathrm{E} M^{\alpha\beta}_\mathrm{I} + N_\mathrm{I} M^{\alpha\beta}_\mathrm{E} + N_\mathrm{E} M^{\alpha\beta}_\mathrm{E}. \end{gathered} \tag{1.150}$$

Correspondingly, the magnetic scattering cross section is split into four terms, one for each of the above terms. The $N_\mathrm{E} M^{\alpha\beta}_\mathrm{E}$ term gives the elastic scattering discussed before. The $N_\mathrm{I} M^{\alpha\beta}_\mathrm{E}$ term gives the so called *magnetovibrational scattering*, which is elastic in the magnetic sector and inelastic in the nuclear part, with emission or absorption of phonons. This is essentially identical to the pure inelastic nuclear scattering, with the form factor modified by the magnetic factors. The $N_\mathrm{E} M^{\alpha\beta}_\mathrm{I}$ term gives scattering elastic in the nuclear sector and inelastic in the magnetic sector, with energy transfer between the neutron and the magnetic degrees of freedom. Finally, the $N_\mathrm{I} M^{\alpha\beta}_\mathrm{I}$ term gives inelastic scattering both in the nuclear and magnetic sectors, with energy exchange between the neutron and the magnetic and nuclear degrees of freedom.

Scattering by spin waves

Let us consider the inelastic magnetic scattering by an ordered magnetic material with no transfer of energy with phonons (that is, the term $N_\mathrm{E} M^{\alpha\beta}_\mathrm{I}$). In this case, the neutrons exchange energy only with the elementary magnetic excitations around the ordered magnetic state, which are called *magnons*

[17]. They are described as follows. Let $\vec{\mathbb{J}}_{ld_\mathrm{m}}$ denote the spin or total angular momentum operator, whatever matters, of the ld_m-th magnetic ion. Let us choose $\vec{M}_{ld_\mathrm{m}}$ as the local quantization axis for the ld_m-th ion, and let $\mathbb{J}^z_{ld_\mathrm{m}}$ the projection of $\vec{\mathbb{J}}_{ld_\mathrm{m}}$ along $\vec{M}_{ld_\mathrm{m}}$, and $\mathbb{J}^x_{ld_\mathrm{m}}$ and $\mathbb{J}^y_{ld_\mathrm{m}}$ the projections onto two mutually perpendicular directions in the plane orthogonal to $\vec{M}_{ld_\mathrm{m}}$. Let $\mathbb{J}^\pm_{ld_\mathrm{m}}$ be the corresponding ladder operators. The magnetic ground state of the ion is given by $|JM_J\rangle$ with $M_J = J$. At low temperature, M_J cannot depart much from its maximum value J. Evidently, this cannot be the case if $J = 1/2$, hence we assume $J > 1/2$. Let us introduce the departure number, $n = J - M_J$, to characterize the magnetic states $|n\rangle = |J\, J-n\rangle$. We perform a Holstein-Primakoff transformation [18], introducing the operators a_{ld_m} and $a^\dagger_{ld_\mathrm{m}}$ which satisfy the bosonic commutation relations

$$[a_{ld_\mathrm{m}}, a_{l'd'_\mathrm{m}}] = 0, \quad [a^\dagger_{ld_\mathrm{m}}, a^\dagger_{l'd'_\mathrm{m}}] = 0, \quad [a_{ld_\mathrm{m}}, a^\dagger_{l'd'_\mathrm{m}}] = \delta_{ll'}\,\delta_{d_\mathrm{m}d'_\mathrm{m}}. \tag{1.151}$$

At each ion, they act on the magnetic states as the creation and annihilation operators of an harmonic oscillator:

$$a_{ld_\mathrm{m}}\,|n\rangle = n^{1/2}\;|n-1\rangle\,, \qquad a^\dagger_{ld_\mathrm{m}}\,|n\rangle = (n+1)^{1/2}\;|n+1\rangle\,. \tag{1.152}$$

By introducing this bosonic operators, the space of states has been artificially enlarged to the space of states with any $n > 0$, but only the states with $n \le 2J$ have physical meaning, and states with $n > 2J$ do not influence the physical results. Indeed, the angular momentum operators are expressed in terms of the bosonic operators as

$$\begin{aligned}
\mathbb{J}^+_{ld_\mathrm{m}} &= \big(2J - a^\dagger_{ld_\mathrm{m}} a_{ld_\mathrm{m}} - 1\big)^{1/2} a_{ld_\mathrm{m}},\\
\mathbb{J}^-_{ld_\mathrm{m}} &= \big(2J - a^\dagger_{ld_\mathrm{m}} a_{ld_\mathrm{m}}\big)^{1/2} a^\dagger_{ld_\mathrm{m}},\\
\mathbb{J}^z_{ld_\mathrm{m}} &= J - a^\dagger_{ld_\mathrm{m}} a_{ld_\mathrm{m}}.
\end{aligned} \tag{1.153}$$

The system Hamiltonian, expressed in terms of the bosonic operators, is expanded in powers of a_{ld_m} and $a^\dagger_{ld_\mathrm{m}}$. It is easy to see from the above equations that this expansion is actually an expansion in powers of $1/2J$. The lowest order is provided by the quadratic terms. In the linear, or harmonic, approximation, only the quadratic terms are taken into account, and the magnetic dynamics is described by a system of coupled harmonic oscillators. In this case we have

$$\mathbb{J}^+_{ld_\mathrm{m}} = \sqrt{2J}\,a_{ld_\mathrm{m}}, \quad \mathbb{J}^-_{ld_\mathrm{m}} = \sqrt{2J}\,a^\dagger_{ld_\mathrm{m}}, \quad \mathbb{J}^z_{ld_\mathrm{m}} = J - a^\dagger_{ld_\mathrm{m}} a_{ld_\mathrm{m}}. \tag{1.154}$$

This approximation is good for large J, and in this case the neglected terms can be systematically taken into account by perturbation theory.

In the linear approximation, the eigenstates of the system, which are called *magnons*, form a Bose-Einstein gas of non conserved particles, with

zero chemical potential. Moreover the correlation $N_{\rm E}M_{\rm I}$ of equation (1.150) can be readily computed in a way completely analogous to that of phonons. Let us consider for simplicity a crystal with only one magnetic ion per unit cell, so that the magnetic ions form a Bravais lattice (and we can remove the $d_{\rm m}$ index), and assume that the system is ferromagnetically ordered. Thus, the only non vanishing Fourier mode of the magnetic moment is that with $\vec{K}=0$, which is denoted in the following by S. To linear order, the solution to the equations of motion is given by

$$a_l(t)=\frac{1}{\sqrt{N_{\rm c}}}\sum_{\vec{p}}{\rm e}^{{\rm i}2\pi(\vec{p}\cdot\vec{R}_l-\nu_{\vec{p}}\,t)}\,b_{\vec{p}}\,,\quad a_l^\dagger(t)=\frac{1}{\sqrt{N_{\rm c}}}\sum_{\vec{p}}{\rm e}^{-{\rm i}2\pi(\vec{p}\cdot\vec{R}_l-\nu_{\vec{p}}\,t)}\,b_{\vec{p}}^\dagger, \tag{1.155}$$

where $\vec{p}$ belongs to the first Brillouin zone of the magnetic ion lattice, the operators $b_{\vec{p}}$ and $b_{\vec{p}}^\dagger$ satisfy the commutation relation $[b_{\vec{p}},b_{\vec{p}'}^\dagger]=\delta_{\vec{p}\,\vec{p}'}$, and $\nu_{\vec{p}}$ are the magnon frequencies.

Using the fact that $\vec{\mathbb{M}}_l=g\mu_{\rm B}\vec{\mathbb{J}}_l$, equations (1.154) and (1.155), and defining $M=g\mu_{\rm B}J$, we easily obtain $\langle\mathbb{M}_l^x\rangle=\langle\mathbb{M}_l^y\rangle=0$, and

$$\langle\mathbb{M}_l^z\rangle=M\big[\,1-(1/JN_{\rm c})\sum_{\vec{p}}\langle n_{\vec{p}}\rangle\,\big], \tag{1.156}$$

where $\langle n_{\vec{p}}\rangle$ is the average value of the number of magnons with wave vector $\vec{p}$, given by the Bose-Einstein distribution (1.72). For the time correlation functions we have $\langle\mathbb{M}_l^z(0)\mathbb{M}_{l'}^\alpha(t)\rangle=\langle\mathbb{M}_l^\alpha(0)\mathbb{M}_{l'}^z(t)\rangle=0$, with $\alpha=x,y$, and

$$\langle\mathbb{M}_l^z(0)\mathbb{M}_{l'}^z(t)\rangle=M^2\Big(1-\frac{2}{JN_{\rm c}}\sum_{\vec{p}}\langle n_{\vec{p}}\rangle\Big)=\langle\mathbb{M}_l^z\rangle\langle\mathbb{M}_{l'}^z\rangle+O(1/J^2), \tag{1.157}$$

so that this correlation, called the *longitudinal* correlation, does not contribute to inelastic scattering[9]. For the remaining components, called the *transverse* correlations, we have

$$\langle\mathbb{M}_l^x(0)\mathbb{M}_{l'}^x(t)\rangle=\langle\mathbb{M}_l^y(0)\mathbb{M}_{l'}^y(t)\rangle,\ \ \langle\mathbb{M}_l^x(0)\mathbb{M}_{l'}^y(t)\rangle=-\langle\mathbb{M}_l^y(0)\mathbb{M}_{l'}^y(t)\rangle, \tag{1.158}$$

with

$$\langle\mathbb{M}_l^x(0)\mathbb{M}_{l'}^x(t)\rangle=\frac{M^2}{2JN_{\rm c}}\sum_{\vec{p}}\Big[{\rm e}^{-{\rm i}2\pi\phi_{ll'}(\vec{p})}\,\big(\langle n_{\vec{p}}\rangle+1\big)+{\rm e}^{{\rm i}2\pi\phi_{ll'}(\vec{p})}\,\langle n_{\vec{p}}\rangle\Big]\,, \tag{1.159}$$

$$\langle\mathbb{M}_l^x(0)\mathbb{M}_{l'}^y(t)\rangle=\frac{{\rm i}M^2}{2JN_{\rm c}}\sum_{\vec{p}}\Big[{\rm e}^{-{\rm i}2\pi\phi_{ll'}(\vec{p})}\,\big(\langle n_{\vec{p}}\rangle+1\big)-{\rm e}^{{\rm i}2\pi\phi_{ll'}(\vec{p})}\,\langle n_{\vec{p}}\rangle\Big]\,, \tag{1.160}$$

where $\phi_{ll'}(\vec{p})=\vec{p}\cdot(\vec{R}_{l'}-\vec{R}_l)-\nu_{\vec{p}}\,t$.

[9]Notice that this correlation is independent of time. The $1/J^2$ terms have to be neglected in the linear approximation for consistency. Higher order corrections guarantee that the second equality in (1.157) holds to all orders in the $1/J$ expansion.

Consider the scattering of an unpolarized beam. We do not observe the polarization state of the scattered neutrons, so that $\sum_{\sigma_f} \rho^i_{\alpha\beta}(\sigma_f) = \delta_{\alpha\beta}$. Then, the cross section depends only on the projection of the time correlation function onto the component perpendicular to $\vec{q}$, which is

$$\sum_{\alpha\beta} \Big(\delta_{\alpha\beta} - \frac{q_\alpha q_\beta}{q^2}\Big) \Big[\langle \mathbb{M}^\beta_l(0)\mathbb{M}^\alpha_{l'}(t)\rangle - \langle \mathbb{M}^\beta_l\rangle\langle \mathbb{M}^\alpha_{l'}\rangle\Big] = \Big(1+\frac{q_z^2}{q^2}\Big)\big\langle \mathbb{M}^x_l(0)\mathbb{M}^x_{l'}(t)\big\rangle, \tag{1.161}$$

where we used $1 - q_x^2/q^2 + 1 - q_y^2/q^2 = 1 + q_z^2/q^2$.

Now, to obtain the inelastic magnetic scattering cross section by a ferromagnet to $1/J$ order (1-magnon scattering), we can insert (1.161) into (1.149) and this into (1.129). The sums in l and l' are obtained using (1.133), and we get

$$\begin{aligned}\frac{d^2\sigma^{(\mathrm{m})}}{d\Omega_{\hat{k}_f} dE_f} &= p^2\,\frac{k_f}{k_i}\,\frac{1}{V}\,\frac{M^2}{2J}\Big(1+\frac{q_z^2}{q^2}\Big)F^2(q)\,T^2(\vec{q})\times \\ &\sum_{\vec{p}\,\vec{H}}\Big[\delta(\vec{q}-\vec{p}-\vec{H})\,\delta(h\nu - h\nu_{\vec{p}})\,\big(\langle n_{\vec{p}}\rangle + 1\big) \\ &\quad + \delta(\vec{q}+\vec{p}-\vec{H})\,\delta(h\nu + h\nu_{\vec{p}})\,\langle n_{\vec{p}}\rangle\Big]\,.\end{aligned} \tag{1.162}$$

This expression is similar to expression (1.140) for the scattering by phonons, and the *magnon dispersion relations*, which provide the dependence of the frequency $\nu_{\vec{p}}$ with the wave vector $\vec{p}$, can be obtained applying the same ideas. One difference between magnon and phonon scattering is the factor $1 + q_z^2/q^2$, which takes values between 1 and 2. If the scattering vector is parallel to $\hat{z}$ the factor is 2, and if it is perpendicular to $\hat{z}$ it is 1. This correspond to the fact that the deviation of the magnetic moment with respect to its equilibrium value is perpendicular to $\hat{z}$. Therefore, it has two components perpendicular to $\hat{q}$ if this vector is parallel to $\hat{z}$ and only one component perpendicular to $\hat{q}$ if it is perpendicular to $\hat{z}$.

The magnon dispersion relation allows us to investigate the nature of the magnetic interactions. For instance, in a ferromagnetic system described by a Heisenberg model, we have $h\nu_{\vec{p}} = 2J[K(0) - K(\vec{p})]$, where $K(\vec{p})$ is the Fourier transform of the exchange interaction coupling.

1.4 Polarization analysis

The scattering of a polarized beam of neutrons together with the analysis of the polarization of the scattered beam is a powerful tool that allows us to extract much more information about the target than the simpler scattering of unpolarized neutrons. Since, as we are going to see, polarization analysis introduces correlations between nuclear and magnetic scattering amplitudes

which are absent in the case of unpolarized beams, we have to consider both nuclear and magnetic scattering at once. To this end, let us write the scattering amplitude operator as a matrix in spin space:

$$\mathcal{A}_{\vec{q}} = \vec{\mathcal{V}}_{\vec{q}} \cdot \vec{\sigma} + \mathcal{W}_{\vec{q}} \mathrm{I}_2, \tag{1.163}$$

where $\vec{\sigma}$ and I_2 are, respectively, the Pauli matrices and the 2×2 identity matrix acting on the neutron spin degrees of freedom, and

$$\vec{\mathcal{V}}_{\vec{q}} = p\vec{\mathcal{M}}_{\perp\vec{q}} + \frac{1}{2}\sum_n \mathrm{e}^{\mathrm{i}2\pi\vec{q}\cdot\vec{R}_n} B_n \vec{\mathcal{I}}_n, \qquad \mathcal{W}_{\vec{q}} = \sum_n \mathrm{e}^{\mathrm{i}2\pi\vec{q}\cdot\vec{R}_n} A_n. \tag{1.164}$$

In the above expressions $\vec{R}_n$, $\vec{\mathcal{I}}_n$, A_n and B_n denote, respectively, the position, the spin, and the two scattering lengths of the n-th nucleus [*c.f.* equation (1.30)].

Let us consider elastic scattering. The density matrix and the polarization vector of the scattered beam are obtained by substituting (1.163) into equations (1.25) and (1.27), respectively. The sum over σ_f defining $I_{\vec{q}}$ and the trace entering equation (1.27) can be easily computed applying several times the well known identity for the Pauli matrices

$$\sigma_\alpha \sigma_\beta = \mathrm{I}_2\, \delta_{\alpha\beta} + \mathrm{i} \sum_\gamma \epsilon_{\alpha\beta\gamma}\sigma_\gamma, \tag{1.165}$$

and using $\mathrm{Tr}\,\sigma_\alpha = 0$ and $\mathrm{Tr}\,\sigma_\alpha\sigma_\beta = 2\delta_{\alpha\beta}$. In the above equation $\epsilon_{\alpha\beta\gamma}$ is the totally antisymmetric tensor in three dimensions. Then, the average over the disorder can be computed as in section 1.2.4. The assumptions are: i) there is no correlation between the probability distributions of isotopes in different nuclei; ii) the nuclear spins are uniformly randomly oriented in space; iii) the spin orientations of different nuclei are uncorrelated; and iv) the disorder in magnetic properties is independent from the disorder in nuclear properties.

Let us introduce the following quantities, appropriate for a generic scattering target

$$W_{\vec{q}} \,=\, \overline{\langle \mathcal{W}_{\vec{q}} \rangle} \,=\, \sum_n b_n \big\langle \mathrm{e}^{\mathrm{i}2\pi\vec{q}\cdot\vec{R}_n} \big\rangle, \tag{1.166}$$

$$\vec{V}_{\vec{q}} \,=\, \overline{\langle \vec{\mathcal{V}}_{\vec{q}} \rangle} \,=\, p\big\langle \vec{\mathcal{M}}_{\perp\vec{q}} \big\rangle, \tag{1.167}$$

where $b_n = \bar{A}_n$ is the coherent scattering length of the n-th nucleus. Notice that by definition $\vec{V}_{\vec{q}}$ is perpendicular to $\vec{q}$. Sometimes $W_{\vec{q}}$ and $\vec{V}_{\vec{q}}$ are referred to, respectively, as generic Nuclear Structure Factor and Magnetic Interaction Vector for the whole system. Retaining only the coherent component from equation (1.27), we get

$$I_{\vec{q}} = W_{\vec{q}} W^*_{\vec{q}} + \vec{V}_{\vec{q}} \cdot \vec{V}^*_{\vec{q}} + \big(W_{\vec{q}} \vec{V}^*_{\vec{q}} + \vec{V}_{\vec{q}} W^*_{\vec{q}}\big) \cdot \vec{P}_i - \mathrm{i}\big(\vec{V}_{\vec{q}} \times \vec{V}^*_{\vec{q}}\big) \cdot \vec{P}_i \tag{1.168}$$

and

$$I_{\vec{q}}\vec{P}_f = \left(W_{\vec{q}}W^*_{\vec{q}} - \vec{V}_{\vec{q}}\cdot\vec{V}^*_{\vec{q}}\right)\vec{P}_i \;+\; \vec{V}_{\vec{q}}\left(\vec{P}_i\cdot\vec{V}^*_{\vec{q}}\right) \;+\; \left(\vec{P}_i\cdot\vec{V}_{\vec{q}}\right)\vec{V}^*_{\vec{q}} \\ +\,\mathrm{i}\left(\vec{V}_{\vec{q}}W^*_{\vec{q}} \;-\; W_{\vec{q}}\vec{V}^*_{\vec{q}}\right)\times\vec{P}_i \;+\; W_{\vec{q}}\vec{V}^*_{\vec{q}} \;+\; W^*_{\vec{q}}\vec{V}_{\vec{q}} \;+\; \mathrm{i}\left(\vec{V}_{\vec{q}}\times\vec{V}^*_{\vec{q}}\right), \tag{1.169}$$

where $\vec{P}_f$ and $\vec{P}_i$ are, respectively, the final and initial beam polarizations.

The theoretical foundations of the scattering of polarized neutrons were developed in [12, 19–26], and can be summarized in the Blume-Maleev equations (1.168) and (1.169) [24, 27] which open new possibilities to design experiments with polarized neutrons beams.

Two consequences of equation (1.169) are immediately apparent: 1) if there is no magnetic scattering, the scattered beam has the same polarization vector as the incident beam; and 2) the magnetic scattering can polarize an unpolarized beam, since the last three terms are independent of $\vec{P}_i$.

Let us consider the elastic scattering by a crystal. As before, the ion position is written as $\vec{R}_l+\vec{r}_d+\vec{u}_{ld}$, and equations (1.166) and (1.167) become

$$W_{\vec{q}} = N_{\vec{q}}\sum_l \mathrm{e}^{\mathrm{i}2\pi\vec{q}\cdot\vec{R}_l}, \qquad \vec{V}_{\vec{q}} = \sum_{\vec{K}}\vec{M}_{\perp\vec{q}}\sum_l \mathrm{e}^{\mathrm{i}2\pi(\vec{q}+\vec{K})\cdot\vec{R}_l}. \tag{1.170}$$

where $N_{\vec{q}}$ and $\vec{M}_{\perp\vec{q}}$ are given by equations (1.132) and (1.145). Then each term of (1.168) and (1.169) contains sums in l and l' of terms of the form (1.133). Thus, each term of these equations is a sum of terms that contain a Dirac delta function $\delta(\vec{q}-\vec{H}\pm\vec{K})$. This is Bragg scattering, and the delta functions define the Bragg peaks at $\vec{q}=\vec{H}\pm\vec{K}$. We get the first Blume-Maleev equation for the scattered intensity in a crystal as

$$I_{\vec{q}} = |N_{\vec{q}}|^2 + |\vec{M}_{\perp\vec{q}}|^2 + \left(N_{\vec{q}}\vec{M}^*_{\perp\vec{q}} + N^*_{\vec{q}}\vec{M}_{\perp\vec{q}}\right)\cdot\vec{P}_i + \mathrm{i}\left(\vec{M}^*_{\perp\vec{q}}\times\vec{M}_{\perp\vec{q}}\right)\cdot\vec{P}_i \tag{1.171}$$

where the vectors $N_{\vec{q}}\vec{M}^*_{\perp\vec{q}} + N^*_{\vec{q}}\vec{M}_{\perp\vec{q}}$ and $\mathrm{i}\vec{M}^*_{\perp\vec{q}}\times\vec{M}_{\perp\vec{q}}$ are called, respectively, *Nuclear-Magnetic Interference Vector* and *Chiral Vector*. The second Blume-Maleev equation for the scattered polarization in a crystal is

$$\begin{aligned} I_{\vec{q}}\vec{P}_f &= \left(|N_{\vec{q}}|^2 - |\vec{M}_{\perp\vec{q}}|^2\right)\vec{P}_i + \left(\vec{P}_i\cdot\vec{M}^*_{\perp\vec{q}}\right)\vec{M}_{\perp\vec{q}} + \left(\vec{P}_i\cdot\vec{M}_{\perp\vec{q}}\right)\vec{M}^*_{\perp\vec{q}} \\ &- \mathrm{i}\left(N_{\vec{q}}\vec{M}^*_{\perp\vec{q}} - N^*_{\vec{q}}\vec{M}_{\perp\vec{q}}\right)\times\vec{P}_i + N_{\vec{q}}\vec{M}^*_{\perp\vec{q}} + N^*_{\vec{q}}\vec{M}_{\perp\vec{q}} \\ &- \mathrm{i}\left(\vec{M}^*_{\perp\vec{q}}\times\vec{M}_{\perp\vec{q}}\right). \end{aligned} \tag{1.172}$$

Notice that, by definition, $N_{\vec{q}}$ vanishes if $\vec{K}$ is not a vector of the nuclear reciprocal lattice, and the nuclear scattering does not contribute to the magnetic satellites.

1.5 Magnetic Crystallography

Let us consider that the nuclear unit cell, as defined in section 1.2.4, contains some magnetic atom located at site $d_{\rm m}$ of the asymmetric unit cell with magnetic moment $\vec{M}_{d_{\rm m}}$. The magnetic moment is an *axial vector* and therefore its transformation rule includes the determinant of the operator (det). Moreover, the symmetry group that we need to consider is not the space group of the crystal but its magnetic space group where the *Time Reversal* operation ($\mathcal{I}'$) can play a role (this operation reverses the components of the magnetic moment and does not change the atomic coordinates).

The magnetic space groups ($\mathcal{M}$) are obtained as the outer direct product of the crystallographic group $\mathcal{G}$ and the group $\mathcal{K}$ formed by the *Identity*, $\mathcal{I}$, and the *Time Reversal*, $\mathcal{I}'$, operations $\mathcal{M} \subset \mathcal{G} \bigotimes \mathcal{K}$ where $\mathcal{K} = \{\mathcal{I},\ \mathcal{I}'\}$. So that a magnetic group has *primed* operations, in which the time reversal acts after an operation of the crystallographic group, and *unprimed* operations. Starting from the 230 space groups $\mathcal{G}$, also known as Fedorov groups, it is possible to buil the 1651 magnetic space groups, or Shubnikov groups, $\mathcal{M}$, as follows: Type I) 230 *colorless* groups without *primed* operations ($\mathcal{M} = \mathcal{G}$), Type II) 230 *grey* or paramagnetic groups composed with the same operations *primed* and *unprimed* ($\mathcal{M} = \mathcal{G} + \mathcal{G}\mathcal{I}'$). The other 1191 called *Black-White* groups are built as $\mathcal{M} = \mathcal{H} + (\mathcal{G} - \mathcal{H})\mathcal{I}'$ where $\mathcal{H}$ are the index 2 subgroups of $\mathcal{G}$ as constituting the *unprimed* elements and the rest of operators ($\mathcal{G} - \mathcal{H}$) multiplied by the time reversal $\mathcal{I}'$. These *Black-White* groups can be split in; Type III) 674 groups in which $\mathcal{H}$ has the same translation group $\mathcal{T}$ as $\mathcal{G}$, and Type VI) 517 groups in which the translation group $\mathcal{T}$ contains translations associated with the time reversal (*primed* translations). Shubnikov groups can be generalized to magnetic *superspace* groups in order to describe the symmetry of the incommensurate magnetic structures.

A paramagnetic crystal is described with a *grey* group but when it orders magnetically the time reversal symmetry is broken. Therefore, in the ordered phase, its Shubnikov group will not include the $\mathcal{I}'$ operation alone, but it can appear combined with any other transformation.

Let $\tilde{g}_p = \{\delta_p|\mathcal{R}_p|\vec{t}_p\}$ be a symmetry operation of the magnetic space group $\mathcal{M}$. A magnetic atom of the $d_{\rm m}$-orbit located at site p, related to the site $d_{\rm m}$ by $\vec{r}_p = \tilde{g}_p\vec{r}_{d_{\rm m}}$, will have a magnetic moment $\vec{M}_p = \delta_p \det(\mathcal{R}_p)\mathcal{R}_p\vec{M}_{d_{\rm m}}$ where δ_p is -1 or $+1$ for *primed* or *unprimed* $\tilde{g}_p$ operations, respectively.

Therefore the magnetic structure factor defined in (1.146) considering $N_{\rm au}$ as the number of magnetic atoms at the asymmetric unit cell, indexed with $d_{\rm m}$ and located at $\vec{r}_{d_{\rm m}}$, and its p-th equivalents by symmetry ($d_{\rm m}$-orbit), reads:

$$\vec{M}_{\vec{q}\vec{K}} = p \sum_{d_{\rm m}}^{N_{\rm au}} F_{d_{\rm m}}(q) \sum_{p}^{d_{\rm m}-orbit} T_{pd_{\rm m}}(\vec{q})\delta_p \det(\mathcal{R}_p)\mathcal{R}_p\vec{S}_{\vec{K}d_{\rm m}} \mathrm{e}^{\mathrm{i}2\pi\vec{q}\cdot\tilde{g}_p\vec{r}_{d_{\rm m}}} \quad (1.173)$$

where the d_{m}-index runs over the magnetic atoms associated to the propagation vector $\vec{K}$ (notice that the Fourier coefficient with index $\vec{K}$ contributes only to the K-satellite), The sum over p concerns the symmetry operators of the crystal that belong to the propagation vector group and $F_{d_{\mathrm{m}}}(q)$ is the magnetic form factor for the d_{m}-th atom. The constant p in front of the right-hand side of (1.173) was defined in section 1.2.5. In the case of a propagation vector different from zero, Eq. (1.144) tells us that two magnetic satellites will be observed around each Bragg nuclear reflection.

1.5.1 Describing magnetic structures

It is possible to describe magnetic structures using the magnetic content of the nuclear unit cell (magnetic moments or Fourier coefficients) and a propagation vector which describe the relation between the orientations of the magnetic moments located in equivalent magnetic atoms but in different nuclear unit cells. The propagation vector appears naturally in the Landau Theory of the 2nd order phase transitions as the modulation that minimize the magnetic energy in the ordered state. The *Irreducible Representations* (*irrep*) of the symmetry group of the propagation vector $\mathcal{G}^{\vec{K}} \in \mathcal{G}$, knowing that it transforms as a polar vector, are also employed to classify a magnetic structure. Usually, only one propagation vector pair ($\{\vec{K}, -\vec{K}\}$) survives as ground state describing the majority of the magnetic structures. However also multi-$\vec{K}$ structures and structures with one $\vec{K}$ and its harmonics are possible.

Based on the translation properties of a magnetic structure, it is possible to define *commensurate* and *incommensurate* structures when, respectively, the components of the $\vec{K} = (p\,q\,r)$ in the nuclear reciprocal lattice basis are rational numbers ($\{p,\, q,\, r\} \in \mathbb{Q}$) or not. In the first case, it is possible to find a magnetic unit cell that is a *multiple* of the nuclear one.

Let us now consider initially the simplest case in Eq. (1.143), that is $\vec{K} = (0\,0\,0)$. In this case the Fourier coefficient $\vec{S}_{\vec{K}d_{\mathrm{m}}}$ is a real vector equal to the magnetic moment at site d_{m}, $\vec{M}_{ld_{\mathrm{m}}}$. This $\vec{K}$ means that the magnetic and the crystallographic unit cells are the same. All the ferromagnetic (FM) structures, and a large part of the antiferromagnetic (AF) ones, occur with this propagation vector. Notice that AF with $\vec{K} = 0$ is possible if there are more than one similar atom at the unit cell.

For a propagation vector, $\vec{K}$, on the Brillouin zone border, i.e. $\vec{K} = \frac{1}{2}\vec{H}$, the Fourier coefficient $\vec{S}_{\vec{K}d_{\mathrm{m}}}$ is real and the magnetic moment, along different unit cells, change its sign, but not its modulus, according to:

$$\vec{M}_{ld_{\mathrm{m}}} = (-1)^{\vec{R}_l \cdot \vec{K}} \vec{S}_{\vec{K}d_{\mathrm{m}}}, \tag{1.174}$$

where $\vec{R}_l$ was defined in 1.2.4 and $\vec{K}$ has the form $(\frac{1}{2}\,\frac{1}{2}\,\frac{1}{2})$, $(\frac{1}{2}\,0\,\frac{1}{2})$, etc...

Let us consider now that $(\{\vec{K},-\vec{K}\})$ are at the interior of the Brillouin zone. If the Fourier coefficients $\vec{S}_{\vec{K},d_{\rm m}}$ are real or its imaginary and real parts are parallel then they can describe an *amplitude modulated* or *sinusoidal* structure:

$$\vec{M}_{ld_{\rm m}} = \vec{S}_{\vec{K}d_{\rm m}} \cos\{2\pi(\vec{K}\cdot\vec{R}_l + \phi_{\vec{K}d_{\rm m}})\}. \tag{1.175}$$

Also with $(\{\vec{K},-\vec{K}\})$ at the interior of the Brillouin zone, in the general case where the Fourier coefficients $\vec{S}_{\vec{K}d_{\rm m}}$ are complex vectors, an *helicoidal* or a *cycloidal* structure can be described if both the real and imaginary parts of $\vec{S}_{\vec{K}d_{\rm m}}$ are orthogonal. In the first case the propagation vector is also orthogonal to both components but in the second case the propagation vector is contained in the plane formed by both components. Let us see how evolves the magnetization along different unit lattices l:

$$\begin{aligned}\vec{M}_{ld_{\rm m}} = {} & 2{\rm Re}\left[\vec{S}_{\vec{K}d_{\rm m}}\right]\cos\{2\pi(\vec{K}\cdot\vec{R}_l + \phi_{\vec{K}d_{\rm m}})\} \\ & -2{\rm Im}\left[\vec{S}_{\vec{K}d_{\rm m}}\right]\sin\{2\pi(\vec{K}\cdot\vec{R}_l + \phi_{\vec{K}d_{\rm m}})\}\end{aligned} \tag{1.176}$$

If the real and imaginary part vectors have the same modulus, then the helicoid or the cycloid have a circular envelope; if not the envelope is elliptical.

The experimental finding of the propagation vector is the first step to determine a magnetic structure. Usually this is done with powder neutron diffraction techniques, which allow a quick inspection of the 3D reciprocal space projected in 1D. The indexation of the magnetic peaks will produce the magnetic lattice and therefore the propagation vector. Once this is done, it is very convenient to use symmetry arguments to reduce the number of possible magnetic structures. Finally, for each possible model it is necessary to try and fit the magnetic intensities measured with neutrons[10]. A complete monograph on these procedures can be found in [28].

At this point it is very important to remember that the experiments produce the scattered intensities, $I_{\vec{q}}$, which are real positive numbers, because they are proportional to the modulus square of the nuclear structure factor, or the magnetic interaction vector, which in absence of spatial inversion symmetry are complex quantities. It means that the experiment does not give a complete information on the nuclear or magnetic structure, because different structures differing in a global phase factor will produce the same intensities pattern. One example of this is explained latter.

1.6 Neutron Powder Diffraction

The first commercial X-ray powder diffractometer was introduced by Philips company in 1947. In the fifties and sixties the use of these apparatuses

[10]The FullProf Suite has the necessary software to accomplish these tasks.

increased, mainly due to mineralogists and metallurgists, as a tool to perform primary structural studies (phase identification, defects, vacancies, etc...). In 1969 Rietveld [29] developed a method for the whole pattern analysis of the powder neutron diffraction data. Later, Cox, Young, Thomas and others [30–32] firstly applied the method to analyze synchrotron and conventional X-ray data. It is important to mention here that the Rietveld method is a refinement process that requires an approximation to the correct structure in advance. Nowadays powder diffraction is a very popular technique that can be found in many laboratories to characterize any kind of crystalline matter and plays a central role in structural physics, chemistry or materials science. It has produced important advances in the knowledge and understanding of high-T_c superconductors, zeolites, fullerenes, permanent magnets, etc... Extensive monographs on powder diffraction can be found in [33, 34]. Here, we will explain some particularities or advantages of the neutron powder diffraction that justify their use.

For a nuclear structure, which includes the determination of the positions of any light element (H, Li, C, N, O, S, etc...), or light elements in the presence of any heavy element (U, Pb, Bi, Ta, etc...), the use of neutron diffraction is the most suitable. For example, in [35] by using powder neutron diffraction in the multiferroic $(NH_4)_2FeCl_5{\cdot}H_2O$, the anomaly observed in the specific heat at 79 K was assigned to an order-disorder phase transformation due to the hydrogen atoms in the NH_4 cation, which produces a change of the symmetry from the space group $Pnma$ at room temperature to $P2_1/c$ for $T < 79$ K. As an example of the second case, high-resolution *in situ* powder neutron diffraction was employed to determine the changes in the UO_2 structure during oxidation allowing the determination and refinement of the structure of β-U_3O_7 [36] at 483 K. Also, if some next-neighbors elements are present (Mn, Fe, Co, Ni, etc...) simultaneously in the structure (e.g. Fe_nNi_m alloys), they can be easily distinguishable by using neutron diffraction.

In situ or *in operando* experiments, employing complex sample environments (very low and high temperatures mK to 3000 K, high pressure up to 30 GPa , high magnetic field up to 20 T), are easy and commonly performed. Due to the large penetration depth of neutrons beams and their non destructiveness, the determination of residual stress or textures measurements in bulk materials is another typical engineering application of neutron powder diffraction [37].

As was explained before, neutrons interact with matter via the strong nuclear force with the nuclei but also via the magnetic dipolar interaction with the unpaired electrons, both interactions with a comparable intensity. That is the reason why neutron powder diffraction is the primary technique to determine magnetic structures, as will be explained in detail in this section. In certain cases, it is necessary to go further using single crystal techniques, with polarized or unpolarized neutrons, as it will be explained

later in sections 1.8 and 1.9.

A *powder* is a polycrystalline sample formed by a huge number of microscopic single crystals randomly oriented. Under these conditions, there are thousands of crystallites[11] in diffraction conditions when the powder is illuminated with an appropriate wave. The 3-dimensional reciprocal space of the powder formed by these crystallites is a set of concentric spherical shells, with radiuses equal to the modulus of each node at the reciprocal lattice (indexed with the vector $\vec{H}$). The intersection of these shells with the *Ewald Sphere* gives rise to the powder diffraction as a set of *Debye-Scherrer Cones* and the intersections of these with a 2D detector gives rise to the typical *Debye-Scherrer Rings*. The integration around these rings reduces the 2D data to a 1D diffraction pattern where the abscissae axis is the 2θ angle ($n\lambda = 2d\sin\theta$) and the ordinates axis corresponds to the diffracted intensity. Therefore, the 3D reciprocal lattice is condensed into a 1D in powder diffraction pattern. This leads to both accidental and exact peak overlap, and some times complicates the determination of individual peak intensities. Also, if the powder is not randomly oriented and therefore it has any preferred orientation, or textures, then the powder leads to biased peak intensities.

In reactor based neutron sources, where the diffractometers operate usually at constant wavelength, the scattering variable is the 2θ angle. However in spallation neutron sources, due to their pulsed nature, the diffractometers are based on *Time of Flight* techniques (ToF) being the scattering variable the incident neutron wavelength λ_i of a polychromatic beam.

The principle of ToF is based on the fact that neutrons have a mass (m) and therefore the de Broglie equation relates the wavelength of the neutron, λ_i, to its velocity, v_i according to $\lambda_i = h/mv_i$, where h is Planck's constant. Therefore, it is possible to determine the wavelength of the neutron by measuring the time t_i that a neutron employs to travel a fixed distance L. Combining these ideas with the Bragg equation yields:

$$\lambda_i = \frac{ht_i}{mL} = 2d_i \sin\theta_0, \qquad t_i = 505.55685(40)\ L\ d_i \sin\theta_0. \tag{1.177}$$

Therefore the d-spacing is proportional to the time of flight (t_i) and the diffraction patters are collected at fixed θ_0. To measure the t_i, all we need is to measure the arrival time of the neutron at the detector, knowing that the starting time of the neutron is fixed by the use of chopper, in reactor sources, or by using the pulses structure, in spallation sources. In equation (1.177) the units are μs, m, and Å for t_i, L and d_i, respectively.

[11] Notice that 1 cm^3 contains $\sim 10^9$ crystallites with size $\sim 10\mu$m or $\sim 10^{12}$ crystallites with size $\sim 1\mu$m.

1.6.1 Some ideas about the Rietveld method

A powder diffraction pattern is a histogram of *counts* measured at the detector (y_i, at the ordinates axis) for each value of the scattering variable (x_i at the abscissae axis), which can be scattering angles ($2\theta_i$), time of flight (t_i) or energies E_i. The Rietveld method consists in minimizing the weighted squared difference between the observations y_i and the calculated y_{ical} against a set of different parameters ($\vec{\xi}$) related mainly with the atomic structure and microstructure of the sample and the optics of the instrument (monochromators, collimators, slits, pulse structure, etc..):

$$\chi^2 = \sum_{i=1}^{n} w_i \{y_i - y_{ical}(\vec{\xi})\}^2, \tag{1.178}$$

where w_i is the inverse of the variance (σ_i^2) of the observation y_i and y_{ical} represent the calculated *counts* as follows:

$$y_{ical} = \sum_{\phi} S_\phi \sum_{\vec{q}} I_{\phi,\vec{q}}\, \Omega(x_i - x_{\phi,\vec{q}}) + y_{bi}. \tag{1.179}$$

The index ϕ runs over all the different phases, nuclear or magnetic, present at the powder with scale S_ϕ, the vector $\vec{q}$ labels a nuclear or magnetic Bragg reflection ($\vec{q} = \vec{H}$ or $\vec{q} = \vec{H} \pm \vec{K}$ where $\vec{H}$ is a node of the reciprocal lattice and $\vec{K}$ is a magnetic propagation vector), $\Omega(x_i - x_{\phi,\vec{q}})$ is the peak-shape normalized function centered at the Bragg position $\vec{q}$ of phase ϕ, which includes the instrumental and sample microstructural effects, and $I_{\phi,\vec{q}}$ is the intensity of that Bragg reflection, which includes the modulus squared either of the nuclear structure factor $|N_{\vec{q}}|^2$ (Eq. 1.135) or the magnetic interaction vector $|\vec{M}_{\perp\vec{q}}|^2$ (Eq. 1.145), among other different corrections (asymmetry, transmission, preferred orientation, efficiencies, etc...). The background is represented by y_{bi}.

The Rietveld method needs an initial, nuclear and/or magnetic, structural model as input. Essentially, it enters at the calculations of the nuclear structure factor (atomic coordinates, occupancies, *Debye-Waller* factors, etc...) or at the magnetic interaction vector (vectorial magnetic atomic moments). Also the Bragg positions $x_{\phi,\vec{q}}$ are a function of the unit cell $(a, b, c, \alpha, \beta, \gamma)$.

1.6.2 Selected examples

Magnetic structure of MnO

Up to year 1949 the only method to detect antiferromagnetism in a compound was via indirect experiments, *i.e.* by observing some anomalies in the specific heat and susceptibility. However, based on the pioneering paper of Halpern and Johnson [12], Shull and Smart, at the Oak Ridge National

Laboratory, initiated a research program to investigate at room temperature the magnetic properties of powders of MnF_2, $MnSO_4$, MnO and α-Fe_2O_3 with neutron scattering. They found no magnetic Bragg signals in MnF_2, $MnSO_4$ but a short-range order in MnO and coherent magnetic scattering in α-Fe_2O_3, being the ordering temperatures, 122 K and 950 K respectively [38]. In the case of MnO, they also collected neutron scattering data at 80 K and observed the same Bragg nuclear peaks observed at 300 K and, additionally, also new strong peaks not indexed with the chemical unit cell but with a doubled cell in each crystallographic direction, in agreement with an AF Longe Range Order (LRO) with a propagation vector $\vec{K} = (\frac{1}{2}\ \frac{1}{2}\ \frac{1}{2})$. This was one of the first magnetic structures determined with neutron scattering.

Antiferromagnetic structures with $\vec{K} = 0$ in $A_2FeX_5{\cdot}H_2O$ (A=K, Rb, X=Cl, Br)

The family of low anisotropy antiferromagnets $A_2FeX_5{\cdot}H_2O$, where (A=K, Rb, X=Cl, Br) was well known in the eighties [39] due to the dimensionality crossover observed in its magnetic behavior [40] and also because its experimental accessibility to the *spin flop* phase transition at relatively low magnetic fields [41] (see section 1.7). Moreover, the diamagnetically site diluted compounds $A_2Fe_{1-x}In_xX_5{\cdot}H_2O$ were a good physical realization of the theoretical *Ramdom Field Ising Model* [42] by its equivalence with the *Diluted Antiferromagnet in presence of a Field* model, as proved by Fishman and Aharony [43]. Moreover, this AF family showed a significant *remanent magnetization*, with singular scaling properties, when cooled in presence of very low fields. All these facts increased the interest in these compounds [44–48].

However, the magnetic structure of these compounds was unknown till Palacio *et al.* collected neutron powder diffraction at the D1B and D2B instruments at the ILL with several main objectives; i) to determine the magnetic super-exchange pathways by refining the O and H atomic positions with high precision at low temperature, ii) to determine and classify the magnetic structure and iii) to measure the temperature evolution of the magnetic moment for each sub-lattice in order to compare it with the observed remanent magnetization to see if both were proportional [49].

The analysis of the data accomplished all these goals. The system crystallizes at the *Pnma* space group. The unit cell of $A_2FeX_5{\cdot}D_2O$ contains four discrete $[FeX_5{\cdot}H_2O]^{2-}$ octahedra connected by hydrogen bonds. In each octahedron three halogen atoms, the oxygen atom and the iron atom are in special positions 4*c* and the other atoms are in general positions. The octahedra are arranged in planes perpendicular to the $\vec{b}$-axis. The hydrogen bonds connect octahedra related by the inversion operator to form chains along the $\vec{b}$-axis. The structure is schematised in Figure 1.6.

The propagation vector found was $\vec{K} = (0\,0\,0)$ giving *ac*-ferromagnetic

planes, antiferromagnetically coupled along the $\vec{b}$-axis with all the magnetic moments parallel to the $\vec{a}$-axis (easy axis), being the super-exchange pathway along the $\vec{b}$-axis (J_1) the most intense. The symmetry analysis helped to classify the magnetic structure as the *irrep* $\Gamma_{1u}(A_x\,0\,C_z)$ of $Pnma$ which is compatible with an A_x, AF, mode along $\vec{a}$-axis and an C_z mode, also AF, along the $\vec{c}$-axis, even if accidentally the refinement did not produce any appreciable magnetic moment along the $\vec{c}$-axis. The magnetic structure had the symmetry of the $Pn'm'a'$ Shubnikov group. As we will see later, the mode C_z will play an important role in the magnetic structure of the ammonium derivative (see section 1.7). Unexpectedly the magnetic moment found at low temperature was 3.9(1) $\mu_{\rm B}$ and 4.06(5) $\mu_{\rm B}$, for respectively K and Rb derivatives, which is around 20% lower than that expected for Fe^{3+}. This question will be analyzed later in section 1.8. The temperature evolution of the sub-lattice magnetic moment was found to be not proportional to the observed remanent magnetization, excluding therefore the possibility of a *bulk effect* as the origin of that remanence.

The problem of the *global phase* in $Ca_3Co_{2-x}Fe_xO_6$

The spin-chain compounds $Ca_3Co_{2-x}Fe_xO_6$ (x=0.2 and 0.4) crystallizes in the rhombohedral space group $R\bar{3}c$ where Co^{3+} ions are located at Wyckoff position $6a\,(0\,0\,\frac{1}{4})$, with $S=2$, and $6b\,(0\,0\,0)$, with $S=0$, separated by Ca^{2+}. The Co^{3+} ions in the adjacent spin chains are shifted by 1/6 or 1/3 along the $\vec{c}$-axis. The compound with $x=0$ was reported to exhibit a *Partially Disordered Antiferromagnetic* (PDA) state, where 2/3 ferromagnetic Ising spin-chain orders with AF interchain interaction while the remaining 1/3 are disordered with zero net magnetization. After the Rietveld refinement of neutron powder diffraction it was possible to locate the Fe^{3+} at the trigonal prims sites $6a$. At low temperatures additional magnetic Bragg peaks were indexed in the nuclear lattice with a propagation vector $\vec{K}=(0\,0\,1)$ which indicates that the centering translation $\vec{t}=(0\,0\,\frac{1}{2})$ was lost in the magnetic structure. The Γ_2 *irrep* of $\mathcal{G}^{\vec{K}}$, common in both sites, labels the magnetic structure and corresponds with ferromagnetic ac-planes, with the magnetic moment parallel to $\vec{c}$-axis, coupled AF along the $\vec{b}$-axis.

In [50] it is demonstrated that two different magnetic structures, i) amplitude modulated structure with a propagation vector $\vec{K}=(0\,0\,1)$ in $R\bar{3}c$ and ii) a PDA structure, with a propagation vector $\vec{K}=(0\,0\,0)$ in $P\bar{1}$, are able to fit the same neutron diffraction pattern because the Fourier coefficients for each model only differ in a global phase factor that cannot be determined by the experiment (see 1.2.5). Both models assure that the total magnetic moment in the unit cell is zero and their Fourier coefficient is:

$$\begin{aligned} \vec{S}_{\vec{K},\,pd_{\rm m}} &= m_z\,(0\,0\,c)\mathrm{e}^{-\mathrm{i}2\pi\psi_{\vec{K},\,pd_{\rm m}}} \\ \psi_{(0\,0\,1),\,pd_{\rm m}} &- \psi_{(0\,0\,0),\,pd_{\rm m}} = \tfrac{\pi}{6} \end{aligned} \qquad (1.180)$$

where m_z is the refined magnetic moment and $c = 1$ or $c = 2\sqrt{3}$ for respectively $\vec{K} = (0\,0\,1)$ or $\vec{K} = (0\,0\,0)$ and the phase factor $\psi_{\vec{K},pd_{\rm m}}$ for each model differs in $\frac{\pi}{6}$ for all the atoms in the orbit of both sites $6a$ and $6b$. Both models correspond to a magnetic moment parallel to the $\vec{c}$-axis, which changes its modulus along the z coordinate of the unit cell following the sequences $...\frac{\sqrt{3}}{2},\ 0,\ -\frac{\sqrt{3}}{2},\ \frac{\sqrt{3}}{2},\ 0,\ -\frac{\sqrt{3}}{2}...$ for $\vec{K} = (0\,0\,0)$ and $...1,\ -\frac{1}{2},\ -\frac{1}{2},\ 1,\ -\frac{1}{2},\ -\frac{1}{2}....$ for $\vec{K} = (0\,0\,1)$.

Incommensurate spiral magnetic structure in $LiFeAs_2O_7$

Iron diarsenate was intensively studied because its redox properties as cathode material in Li-ion batteries. However it was also interesting to understand how the Fe ions interacted, through magnetic exchange pathways involving 2 oxygens, originating a LRO at temperatures ~ 35 K. For that reason, and to refine the crystallographic structure regarding the light elements, Rousse *et al.* [51] performed high resolution powder neutron diffraction experiments at the instrument D1A at several temperatures and thermodiffraction from 2K to 50 K at the high flux D1B instrument, which is optimized for magnetic measurements with its good resolution at low angles.

The refined nuclear structure confirmed the space group as $C2$ and allowed to locate with high accuracy the Li atoms, which are in the free channels along the $(0\,0\,1)$ direction formed by each FeO_6 octahedron surrounded by six diarsenate As_2O_7. Unlike the phosphate analogue, the patterns collected in $LiFeAs_2O_7$ below 35 K showed new extra Bragg peaks indexed with a propagation vector $\vec{K} = (0.709\ 0\ 0.155)$, which is not a high symmetry point of the Brillouin zone, representing a incommensurate structure.

With these conditions, the symmetry analysis does not provide any constraint on the Fourier coefficients. The authors excluded the possibility of any spiral structure with axis parallel to neither any crystallographic axis nor the propagation vector. However, by using *simulating annealing* techniques, the authors found two possible orientations for the spiral axis, related by the twofold rotation axis, indistinguishable by the diffraction pattern, and a magnetic moment for Fe ion 4.28(3) $\mu_{\rm B}$. This magnetic structure is intermediate between a pure helical and pure cycloidal structure.

The magnetic spiral structure can be explained by considering a triangular topology of AF interactions between the Fe ions (J_1, J_2 and J_3), which produces some frustration responsible from the non collinearity of the spins, which fulfil the conditions $J_2 \approx 0.522 J_1$ and $J_3 \approx 6.932 J_1$.

Long period helical structures

TM_3S_6 (T=Transition metal, M = Nb and Ta), an intercalated systems of 2H-MS_2, are described by the chiral space group $P6_322$ and they *appar-*

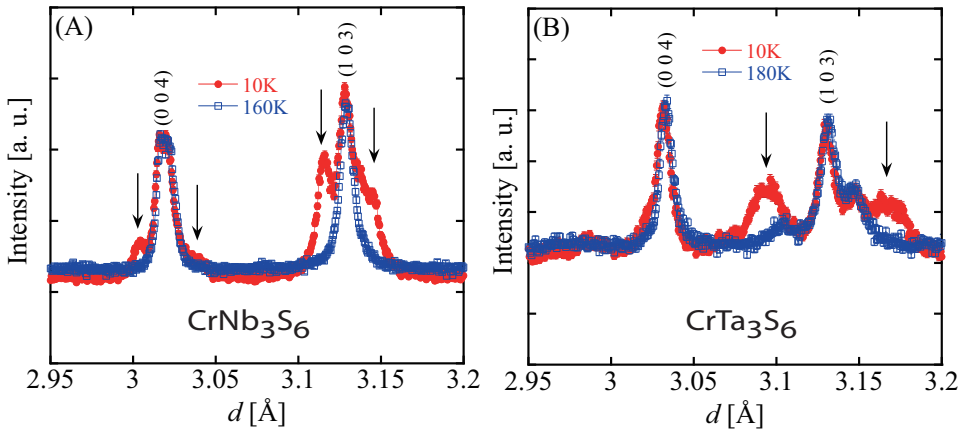

Figure 1.1: Neutron powder diffractograms around the nuclear (0 0 4) and (1 0 3) reflections in (a) $CrNb_3S_6$ and (b) $CrTa_3S_6$. The vertical arrows indicate observed magnetic satellite peaks

.

ently showed a variety of magnetic behaviours; paramagnetism for $TiNb_3S_6$, VNb_3S_6, $TiTa_3S_6$ and VTa_3S_6, AF for $FeNb_3S_6$, $CoNb_3S_6$, $NiNb_3S_6$, $CoTa_3S_6$ and $NiTa_3S_6$, and ferromagnetism for $CrNb_3S_6$, $MnNb_3S_6$, $CrTa_3S_6$, $MnTa_3S_6$ and $FeTa_3S_6$ [52–54].

The monoaxial helimagnet $CrNb_3S_6$ has received attention recently due to the observation of magnetic chiral soliton lattice directly probed by Lorentz transmission electron microscopy (LTEM) [55] and by the theoretical predictions about its magnetic phase diagrams [56–59]. However thermal neutron diffraction studies firstly reported that $CrNb_3S_6$ was a ferromagnet because the magnetic peaks were observed at the same diffraction angle as the nuclear ones [60].

The pitch angle of a chiral helimagnetic structure, mainly determined by the ratio of the exchange interaction (J) and the Dzyaloshinskii-Moriya interaction (D), is usually very small and therefore the period can be hundreds of angstroms[12]. In some cases, the angular resolution of conventional neutron diffractometers is not high enough to separate nuclear Bragg from magnetic satellite peaks. As a consequence, some compounds with helical ordering may be easily misinterpreted as ferromagnets.

In this example, it is highlighted that ultra high resolution neutron powder diffraction experiments made it possible to detect incommensurate satellite peaks related to very small propagation vectors in the compounds $CrNb_3S_6$ and $CrTa_3S_6$, previously reported as ferromagnets [61].

For that purpose, the experiments were performed at the SuperHRPD diffractometer, in the Materials and Life Science Facility (MLF), at 10 K

[12] In helical structures, driven by *magnetic frustration* the period is usually shorter

and paramagnetic phase at 160 K and 180 K for, respectively, $CrNb_3S_6$ and $CrTa_3S_6$. Fig.1.1 shows the results around the nuclear (0 0 4) and (1 0 3) reflections for $CrNb_3S_6$ and $CrTa_3S_6$ obtained by the backward detector bank. The magnetic satellites for both compounds (Fig.1.1) were successfully separated and indexed by $\vec{K} = (0\,0\,\delta)$, with $\delta = 0.0206(2)$ for $CrNb_3S_6$, giving a helimagnetic period of 510 Å, slightly longer than that reported with LTEM. This discrepancy was assigned to the sample quality because a fewer defects in Cr sites may change the helical periodicity governed by D/J. The new observed peaks for $CrTa_3S_6$ were indexed with $\delta = 0.0538(1)$, which produced a period of 225 Å.

1.7 Single Crystal Neutron Diffraction

As it was explained before, the NPD techniques provide unique information about the magnetic periodicities, or magnetic correlations, in magnetically Long Range Ordered (LRO) materials. However the information given by the powder diffraction techniques is sometimes incomplete because, basically, we have only access to a projection of the 3D reciprocal space onto one dimension (1D), *i.e.* only the modulus of the reciprocal lattice $\vec{H}$ node vector is measurable and therefore different reflections $I_{\vec{H}}$ associated to $\vec{H}$ vectors with the same modulus will overlap at the same point in the powder diffractogram. However the diffraction in single crystals will permit the full exploration of the 3D reciprocal space and the individual measurement of each reflexion $I_{\vec{H}}$. Moreover, diffraction in single crystals will specially be suitable when an external axis needs to be defined (e.g. a magnetic field). In the next examples these ideas will be illustrated.

Modulated magnetic structures in multiferroics

The magneto-electric effect, *i.e.* the cross control of magnetization with electric fields and the electric polarization by magnetic fields, was predicted a long time ago by Pierre Curie [62]. Later on, in the 1960's and 70's, materials with this effect attracted great interest. However, it was after the discover of magneto-electric multiferroicity in the perovskite $TbMnO_3$ by Kimura *et al.* [63] when these materials became interesting from the point of view of its spintronic applications, because of its enhanced coupling. In their seminal paper, several magnetic models to explain the observed magneto electricity properties in $TbMnO_3$ were suggested and, as a consequence, it was imperative to revisit the previous knowledge about its published magnetic structures.

Magnetic structures of $TbMnO_3$. At room temperature the crystal structure of $TbMnO_3$ can be described with the space group *Pbnm*. The heat capacity shows three anomalies at $T_{Mn} \approx 41$ K, $T_L \approx 27$ K and $T_{Tb} \approx 7$ K. Previous neutron scattering experiments seemed to indicate that the Mn

sublattice ordered with a sinusoid modulated AF structure between T_{Mn} and T_L, with the magnetic moments parallel to the $\vec{b}$ axis, and an incommensurate propagation vector $\vec{K} = (0\ 0.295\ 0)$, which slightly decreased its value to $\vec{K} = (0\ 0.27\ 0)$. In this region, X-ray diffraction revealed that the modulated magnetic order was accompanied with a lattice modulation. In the region between T_L and T_{Tb} the magnetic propagation vector locked at constant value $\vec{K} = (0\ 0.27\ 0)$, and below T_{Tb} the Tb ions ordered magnetically with a different propagation vector. It is below T_L when $TbMnO_3$ develops ferroelectric behaviour with an electrical polarization parallel to the $\vec{c}$ axis. It is clear that the knowledge of the magnetic structure is not complete and for that reason new neutron diffraction experiments in single crystals were needed. Initially Kajimoto and co-workers [64, 65], from experiments in single crystals, suggested the existence of a *complex non-collinear* magnetic order below T_L together with the incommensurate lattice modulation.

Moreover, the experiments done by Kenzelmann and co-workers [66] contributed to clarify the magnetic models at every region of the $T - B$ phase diagram. Their works agreed with the order observed previously for the region between T_{Mn} and T_L. They classified the magnetic structure under the Γ_3 *irrep* of $\mathcal{G}^{\vec{K}}$ without observing high-order Fourier components. However, in the region from T_L to T_{Tb}, they described the magnetic structure by using Γ_2 and Γ_3 *irreps* forming a elliptical spiral perpendicular to the $\vec{b}$ axis and with a significant magnetization along the $\vec{a}$ axis in the Tb sub-lattice. The simultaneous presence of both *irreps* indicate the breaking of inversion symmetry and therefore the presence of electrical polarization below T_L. Below T_{Tb} a new propagation vector, $\vec{K}_{Tb} = (0\ 0.425\ 0)$, associated with Tb ions appeared together with several strong odd high-order harmonics, indicating strong distortions at the sinusoidal modulated Tb magnetic structure.

Multiferroicity in the molecular compound $(NH_4)_2FeCl_5{\cdot}H_2O$. The magnetic structures of the low anisotropy AF series $A_2FeX_5{\cdot}H_2O$ at zero magnetic field were discussed in subsection 1.6.2. However, the ammonium derivative $(NH_4)_2FeCl_5{\cdot}H_2O$, which has been described as the first molecular multiferroic [67], develops a slightly different one [68, 69]. In fact, this compound shows two anomalies in the heat capacity curves at $T_{FE} = 6.9$ K and $T_N = 7.2$ K associated with different magnetic phases. Single crystal neutron diffraction at cero magnetic field allowed to determine an incommensurate propagation vector $\vec{K} = (0\ 0\ 0.2288)$ at 2K. Moreover, none of the models described by an unique *irrep* of the $\mathcal{G}^{\vec{K}}$, with $\mathcal{G} = P2_1/c$, did reproduce the collected magnetic reflections. However the simultaneous use of 2 *irrep*, with a phase difference between the Fourier Coefficients of the respective *irrep* of $\pi/2$, fitted it. It was a hint of a symmetry reduction from $2/m \rightarrow m$, also needed to explain the observed ferroelectricity in this compound. Within this model, the Fe magnetic moments develop 2 pairs of AF coupled cycloids contained in the a, c-plane and propagating along

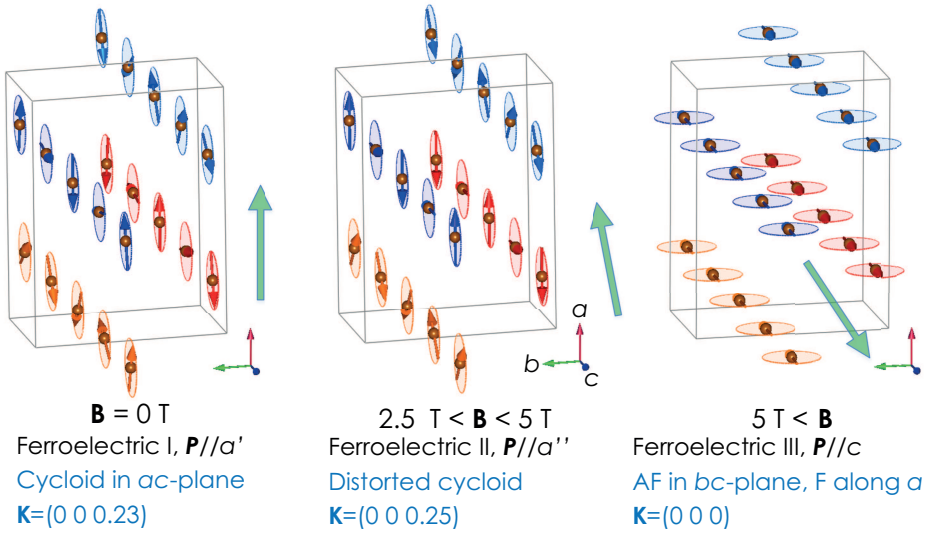

Figure 1.2: Magnetic structures of $(NH_4)_2FeCl_5{\cdot}H_2O$ for the three regimes of the magnetic field applied parallel to the $\vec{a}$ axis at $T = 2$ K. The propagation vector $\vec{K}$ is changing from $\vec{K}_0 = (0\ 0\ 0.23)$, to $\vec{K}_{3.5} = (0\ 0\ \frac{1}{4})$ and $\vec{K}_{5.5} = (0\ 0\ 0)$ for fields 0, $2.5 \leq B \leq 5$ and $5 < B$ T. The green arrow represents the direction of the electrical polarization vector.

the $\vec{c}$-axis with a phase shift of 41.5°. The same super-exchange pathway along the $\vec{b}$-axis (J_1) that produces the AF coupling in the cycloids, and the reduced magnetic moment of $3.8\,\mu_B$ measured for the Fe^{+3} ions, were also observed in the K and Rb derivatives.

Spin-Flop transition and magnetic structures in the hybrid multiferroic $(NH_4)_2FeCl_5{\cdot}H_2O$

In the preceding paragraphs, the magnetic structures of the series of easy axis Heisenberg AF $A_2FeX_5{\cdot}H_2O$, at zero magnetic field, determined from NPD experiments, has been shown. However, due to the low anisotropy of the ion Fe^{3+} in these compounds, its *Spin–Flop* transitions occur at relatively low fields ($\vec{B} \leq 5$T)) [39]. It facilitated the determination of the magnetic structures inside the *Spin–Flop* region, by using single crystal neutron diffraction techniques with an applied magnetic field. In fact, the magnetic moment flopped from the $\vec{a}$ axis at zero field to the $\vec{c}$ axis for fields $\vec{B} \leq 3$T keeping the same *irreps* Γ_{1u} of the space group *Pnma* [70].

In crystals of the ammonium derivative $(NH_4)_2FeCl_5{\cdot}H_2O$, which shows a multiferroic behaviour, the evolution of its cycloidal magnetic structure was also studied, by applying a magnetic field parallel to its $\vec{a}$ easy axis at low temperatures ($T = 2$K), with the help of neutron diffraction [71]. These experiments showed the change of the propagation vector from $\vec{K}_0 = (0\,0\,0.23)$, to $\vec{K}_{3.5} = (0\ 0\ \frac{1}{4})$ and $\vec{K}_{5.5} = (0\ 0\ 0)$ for fields $B = 0$, $2.5 \leq B \leq 5$ and $5 < B$ T. The electrical polarization vectors related to the magnetic structures determined in these experiments are in agreement with the macroscopic measurements done in Ref. [67]. The knowledge of the magnetic structures, incommensurate and distorted commensurate cycloidal in the *ac*-plane and collinear in the $\vec{c}$ axis (corresponding to the spin–flop transition), leads to the conclusion that the mechanism responsible for multiferroicity in $(NH_4)_2FeCl_5{\cdot}H_2O$ is changing from the so called *spin–current* mechanism to the *spin–dependent p–d hybridization* mechanism. The magnetic structures in the three different magnetic field regimes are displayed in the figure 1.2.

Magnetic ordering by dipolar interactions in Single Molecule Magnet Mn_{12}-acetate

In the 90's the molecular magnetic clusters like Mn_{12} or Fe_8 or Mn_4 and others where intensively studied because they show a Single Molecule Magnet (SMM) behaviour including quantum tunnelling of the magnetization vector [72–77] . All of them behave as super-paramagnetic entities with a large magnetic moment, blocking temperatures below 10 K and a large magnetic anisotropy. Here we will focus on the Mn_{12}-acetate cluster.

Mn_{12}-acetate is a cluster containing 12 Mn atoms arranged in such a way that 4 ions with Mn^{4+} with S=3/2 are in a core surrounded by 8 Mn^{3+} with S=2 coupled AF [78, 79] with those of the core giving a total spin equal to 10 and therefore a magnetic moment of 20 μ_B. It crystallizes in the tetragonal space group $I\bar{4}$ with 4 molecules in the unit cell with a quasi null intermolecular exchange due to weak Van der Waals forces.

Mn_{12}-acetate was theoretically predicted at low temperatures (∼0.5 K) to be a ferromagnetic LRO due to strong dipolar magnetic interactions between the high-spin molecules [80]. Therefore the verification of this prediction was a very nice experiment to be done with the use of neutron diffraction in a deuterated single crystal (0.5x0.5x1 mm^3) of Mn_{12}-acetate.

However, the spin reversal via quantum tunnelling in Mn_{12}-acetate becomes extremely slow at low temperatures (∼2 months at T=2 K) and, for the time scales 10^2-10^4 seconds of a typical neutron diffraction experiment, the spins are unable to attain thermal equilibrium below a blocking temperature $T_B \sim 3$ K, higher than the ordering temperature $T_C \sim 0.5$ K. This problem could be circumvented by the application of an orthogonal magnetic field to the anisotropy axis $\vec{c}$ of Mn_{12}-acetate ($\vec{B}_\perp$) that promotes quantum tunnelling of the molecular spins [81].

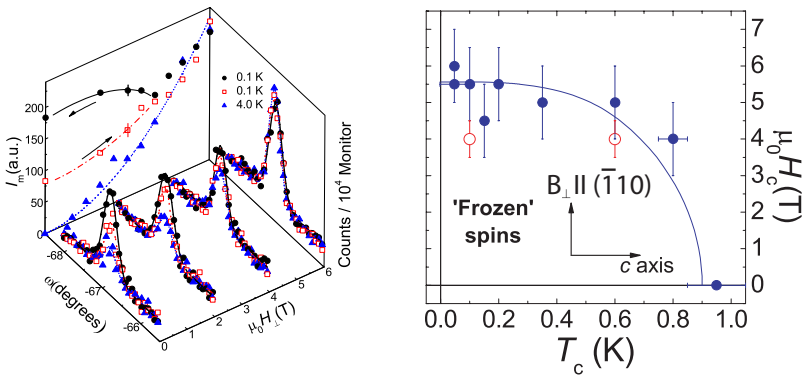

Figure 1.3: Evolution of the reflection (2 2 0) for different magnetic fields $\vec{B}_\perp$ and temperatures (left) and the experimental magnetic phase diagram of Mn_{12}-acetate (right). From ref.[81].

.

The experiment was performed at the instrument D10 of ILL, as proposed in the last paragraph, by using a cryomagnet to apply vertical magnetic fields up to 6 T and with a dilution fridge to go down to ∼30 mK. The examination of several appropriate magnetic reflections of a deuterated crystal of Mn_{12}-acetate, aligned with it $\vec{c}$ axis in the horizontal plane and its $(\bar{1}\,1\,0)$ axis parallel to $\vec{B}_\perp$, as a function of T and $\vec{B}_\perp$ were enough to determine its magnetic phase diagram, which shows a ferromagnetic phase transition line at $\sim$ 0.9 K at zero field in agreement with the predictions (Figure 1.3). These results verified that for large enough $\vec{B}_\perp$ the molecule of Mn_{12}-acetate becomes diamagnetic because its ground state is something like $|\phi\rangle = |10, +10\rangle - |10, -10\rangle$ giving $S_T = 0$

Trapping the different magnetic phases in the chiral molecular magnet $[Cr(CN)_6][Mn(S)\text{-}pnH(H_2O)]\cdot(H_2O)$

The magnetic-field-induced effects can be anticipated to be very large if the structurally chiral compound orders magnetically (e.g. ferrimagnetism, ferromagnetism, weak ferromagnetism, conical, helical, etc...) below a certain temperature. Despite this interest, very few molecular candidates likely to exhibit magnetic and nuclear chirality have been synthesized until now.

Inoue and coworkers have recently developed a synthetic approach based on cyano-bridged bimetallic complexes by networking magnetic 'bricks' that have more than three connections. In these compounds, cyanometallate magnetic anions $[M(CN)_n]^{m-}$ and a second magnetic metal ion M' coordinated to a chiral ligand alternate as building blocks to develop a chiral lattice [82, 83]. Here we analyse the magnetic structures of the chiral magnetic molecular compound of formula $[Cr(CN)_6][Mn(S)\text{-}pnH(H_2O)]\cdot(H_2O)$

where (S)-pn=(S)-1,2-diaminopropane prepared following Inoue' s strategy.

This compound presents three nuclear phases, each one is magnetic at low temperature with critical temperatures of T_C = 38 K, 39 K and 73 K for Phases I, II and III, respectively, all remarkably high temperatures for a metal-organic molecular magnet. The three phases can be transformed into one another, differing mainly in the position of the chiral carbon and in the water content, by heating and cooling and applying vacuum conditions. Remarkably enough, all three nuclear phases (and therefore also the magnetic ones) are reversible and can be reached in the same experiment by using neutron LAUE diffraction [84].

For the three phases the space group is $P2_12_12_1$. In Phase I the Mn^{2+} ions are linked to four Cr^{3+} ions by four of the six cyanide groups in the $[Cr(CN)_6]^{3-}$ ion thus forming a bimetallic patchwork that is arranged almost perpendicularly to the $\vec{c}$ axis to form a two-dimensional chiral network. The Mn^{2+} ions are also linked to one water molecule and to the amino-acid ligand, which induces the chirality and completes the octahedron [85].

As particularities of the neutron LAUE diffraction method we can mention that i) it gives access, in a very fast way, to a large portion of the reciprocal space and therefore it allows some "dynamic" crystallographic studies and ii) LAUE methods use a quasi "white" neutron beam, which means that the number of neutrons arriving to the sample is increases, and therefore it can be employed in very small crystals.

In a small crystal of $[Cr(CN)_6][Mn(S)\text{-pnH}(H_2O)]\cdot(H_2O)$ this technique determined that the propagation vector is $\vec{K}$ = (0 0 0) for the three magnetic phases, so the nuclear and the magnetic unit cells are the same. All three phases show two interpenetrating magnetic sublattices, one of Cr and another one of Mn AF coupled. Magnetic Phases I and II can be described by the *irrep* Γ_4 of $P2_12_12_1$, which leaves the $\vec{a}$ axis ferromagnetic, while Phase III is described by a Γ_3, leaving the $\vec{b}$ axis ferromagnetic. The magnitudes of the moments are slightly less than the spin–only moments for Cr^{3+} and Mn^{2+}, but are in good agreement with similarly coordinated ions in the other Cr and Mn compounds.

1.8 Polarized Neutron Diffraction

The experiments described till now were performed with non-polarized neutrons beams, so that the intensity diffracted was $I_{\vec{q}} = N_{\vec{q}}N^*_{\vec{q}} + \vec{M}_{\perp\vec{q}} \cdot \vec{M}^*_{\perp\vec{q}}$ ($\vec{q} = \vec{H} \pm \vec{K}$ where $\vec{H}$ is a node of the reciprocal lattice and $\vec{K}$ is the magnetic propagation vector that plays only in the magnetic part). In such expression, the Nuclear Structure Factor, $N_{\vec{q}}$, and the Magnetic Interaction Vector, $\vec{M}_{\perp\vec{q}}$, appear not coupled.

However, if we polarize the neutron beam, by using, for example, ^{3}He spin filters or Heusler-Alloy monochromators, the first Blume-Maleev equa-

tion (Eq. 1.171) states that, on top of the modulus square of $N_{\vec{q}}$ and $\vec{M}_{\perp\vec{q}}$, the scattered intensity, $I_{\vec{q}}$, incorporates the initial polarization vector of the neutron beam, $\vec{P}_i$, multiplying the *Nuclear-Magnetic Interference Vector* $(N_{\vec{q}}\vec{M}^*_{\perp\vec{q}} + N^*_{\vec{q}}\vec{M}_{\perp\vec{q}})$ and the *Chiral Vector* $\mathrm{i}(\vec{M}^*_{\perp\vec{q}} \times \vec{M}_{\perp\vec{q}})$, which is non null for non-collinear magnets.

In the following examples the initial polarization $\vec{P}_i$ of the neutron beam can be changed between two states, up ($\uparrow$) and down ($\downarrow$), or parallel and antiparallel, and the detector counts for all the scattered neutrons for each initial polarization state up, $I^{\uparrow}_{\vec{q}}$, or down, $I^{\downarrow}_{\vec{q}}$. These scattered intensities include both *non spin-flip* and *spin-flip* processes (e.g. $I^{\uparrow}_{\vec{q}} = I^{\uparrow\uparrow}_{\vec{q}} + I^{\uparrow\downarrow}_{\vec{q}}$ and $I^{\downarrow}_{\vec{q}} = I^{\downarrow\downarrow}_{\vec{q}} + I^{\downarrow\uparrow}_{\vec{q}}$). These are the ideas of the Linear Neutron Polarimetry initially developed experimentally by Moon, Riste and Koheler [86].

The Fourier transform of the magnetic structure factors, $\vec{M}_{\vec{q}}$, which can be experimentally determined by using polarized neutron diffraction (PND) is directly related to the magnetization density in the unit cell. In these experiments a key point is the maximization of the induced magnetization in the sample along the magnetic field axis, which is parallel to the initial beam polarization. For that reason, in most cases, high magnetic fields and low temperatures will be used for paramagnetic samples. Also, in these experiments, the previous knowledge of the crystalline structure (i.e. the nuclear structure factors $N_{\vec{q}}$) obtained from a non-polarized neutron experiment is needed.

Whilst the nuclear contribution to the diffraction intensities is independent of the polarization of the neutron beam, the magnetic contribution varies depending on whether the incident beam is polarized parallel ($\uparrow$) or anti-parallel ($\downarrow$) to the applied field. In a PND experiment the measured quantity is the *Flipping Ratio*, $R_{\vec{q}} = I^{\uparrow}_{\vec{q}}/I^{\downarrow}_{\vec{q}}$, where $I^{\uparrow}_{\vec{q}}$ and $I^{\downarrow}_{\vec{q}}$, were defined before and they adopt the following expression when the polarization of the neutron beam is parallel to a magnetic field applied along the $\vec{z}$ axis:

$$I^{\uparrow(\downarrow)}_{\vec{q}} = |N_{\vec{q}}|^2 \pm (N_{\vec{q}}\vec{M}^{z*}_{\perp\vec{q}} + N^*_{\vec{q}}\vec{M}^{z}_{\perp\vec{q}}) + |\vec{M}_{\perp\vec{q}}|^2 \pm \mathrm{i}(\vec{M}^{x*}_{\perp\vec{q}}\vec{M}^{y}_{\perp\vec{q}} \mp \vec{M}^{x}_{\perp\vec{q}}\vec{M}^{y\,*}_{\perp\vec{q}}). \quad (1.181)$$

where the upper or down sign in $\pm$ or $\mp$ is taken for up ($\uparrow$) or down ($\downarrow$) initial polarization, respectively. Assuming that the magnetization is parallel (or quasi-parallel) to the polarization of the beam $\vec{P}_i$ or the interaction vector is real ($\vec{M}_{\perp\vec{q}} = \vec{M}^*_{\perp\vec{q}}$), the *Flipping Ratio* $R_{\vec{q}}$ is given by,

$$R_{\vec{q}} = \frac{I^{\uparrow}_{\vec{q}}}{I^{\downarrow}_{\vec{q}}} = \frac{|N_{\vec{q}}|^2 + (N_{\vec{q}}\vec{M}^{z*}_{\perp\vec{q}} + N^*_{\vec{q}}\vec{M}^{z}_{\perp\vec{q}}) + |\vec{M}_{\perp\vec{q}}|^2}{|N_{\vec{q}}|^2 - (N_{\vec{q}}\vec{M}^{z*}_{\perp\vec{q}} + N^*_{\vec{q}}\vec{M}^{z}_{\perp\vec{q}}) + |\vec{M}_{\perp\vec{q}}|^2}, \quad (1.182)$$

where $\vec{q}$ is the scattering vector of the Bragg reflection[13], $N_{\vec{q}}$ and $\vec{M}_{\perp\vec{q}}$ are the nuclear structure factor and magnetic interaction vector, respectively.

[13] If these experiments are done in a magnetically ordered crystal then the nuclear and magnetic lattices need to be the same

When the crystal structure is non-centrosymmetric, both $N_{\vec{q}}$ and $\vec{M}_{\perp\vec{q}}$ are complex, and the magnetic structure factors $\vec{M}_{\vec{q}}$ cannot be directly extracted from Eq. 1.182 by using *direct methods* (Fourier Transform, Maximum Entropy). Instead, the spin density can be modeled to provide a best fit to the flipping ratios by using *indirect methods*. Two approaches have been utilized to model the spin-density distribution; (a) magnetic wave-function approach [87] and (b) multipolar-expansion approach [88].

Magnetic wave-function approach. In this approach the magnetization density $m(\vec{r}) = \left|\left\langle \vec{\mathbb{M}}(\vec{r})\right\rangle\right|$ coming from each ion can be described in terms of an orbital $|\psi_i\rangle$ centered in that ion

$$m(\vec{r}) = \sum_{i\in atoms} S_i \mid \langle \vec{r} \mid \psi_i\rangle \mid^2 \text{ and } |\psi_i\rangle = \sum_j \alpha_{ij} \, |\varphi_j\rangle \, . \tag{1.183}$$

The S_i are the atomic spin populations and the $|\psi_i\rangle$ are the atomic magnetic wave functions, which are linear combinations of standard atomic orbitals and the coefficients α_{ij} fulfill the condition $\sum_j |\alpha_{ij}|^2 = 1$. The atomic spin populations, S_i, the coefficients α_{ij}, and the radial exponents of the Slater atomic orbitals are the parameters of the model.

Multipolar expansion approach. In this approach the spin density is partitioned into separate atomic contributions which are expanded in the basis of real spherical harmonics $\mathcal{Y}_l^m$, which are also referred to as multipoles [88]

$$m(\vec{r}) = \sum_{i\in atoms} \sum_l \mathcal{R}_i^l(|\vec{r} - \vec{r}_i|) \sum_{m=-l}^{m=l} p_i^{lm} \mathcal{Y}_l^m(\theta_i, \varphi_i), \tag{1.184}$$

where p_i^{lm} are the population coefficients of the real spherical harmonics $\mathcal{Y}_l^m(\theta_i, \varphi_i)$ and $\mathcal{R}_i^l$ are the Slater radial functions defined as:

$$\mathcal{R}_i^l(r) = \frac{\zeta_l^{n_l+3}}{(n_l+2)!} r^{n_l} e^{-\zeta_l r}. \tag{1.185}$$

The ideas described here were applied to understand the magnetic interaction mechanisms in the purely organic magnet family *p*-X-C_6F_4CNSSN and in the low anisotropy AF family $A_2FeX_5{\cdot}H_2O$.

Spin density experiments in *p*-O_2N-C_6F_4CNSSN and $A_2FeX_5{\cdot}H_2O$ (A=K, Rb, X=Cl, Br)

Magnetic interaction mechanism in p-X-C_6F_4CNSSN (X=O_2N, CN, Br, I). To enhance the magnetic interaction, and therefore the temperature for magnetic LRO, sulphur based organic magnets were proposed [89] due to the larger radially extension of the sulfur atomic orbitals compared with

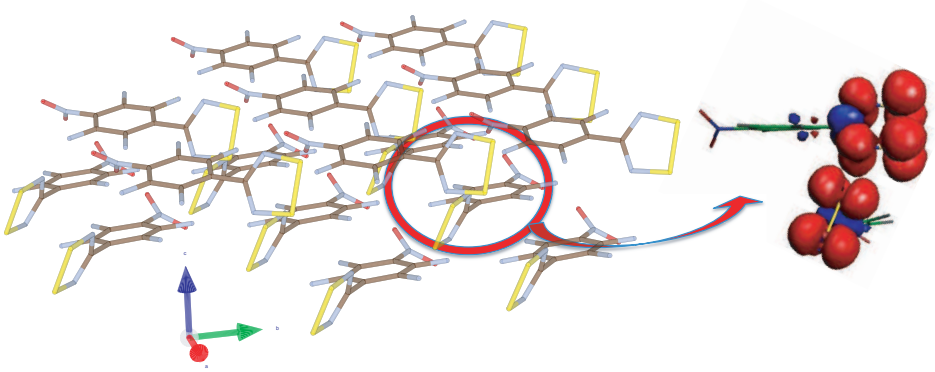

Figure 1.4: Relative space localization of two molecules of p-O_2N-C_6F_4CNSSN. The magnetic interaction between these two molecules is supposed to be ferromagnetic due to the small magnetic orbital overlapping.

those of the oxigen in p-NPNN ($T_C = 0.65$ K) [90]. This strategy proved to be very successful and it is today the phase β of p-NC-C_6F_4CNSSN, which undergoes a phase transition to a canted AF state below 36 K, being the metal-free compound with the highest reported magnetic LRO temperature [91].

The spin density studies in a crystal of p-O_2N-C_6F_4CNSSN, obtained with polarized neutron diffraction, and supported by *ab-initio* Density Functional Theory (DFT) calculations, were crucial to provide a fundamental understanding of the magnetic behavior of the dithiadiazolyl radical family and the magnetism of p-orbitals, which can be employed to design new metal-free sulphur-based magnets [92].

The polarized neutron diffraction studies revealed that the spin density is almost entirely located on the sulphur and nitrogen atoms of the dithiadiazolyl ring in a p_z orbital-type distribution with the $\hat{z}$ axis perpendicular to the ring, and a small negative spin density on the C atom arising out of spin polarization. These studies also show that the spin density is displaced away from both atoms and bonds within the dithiadiazolyl ring, in agreement with the anti-bonding nature of the SOMO determined by *ab-initio* DFT calculations. Both the experimental and theoretical studies also indicate small negative spin densities in the plane of the heterocyclic ring.

This exhaustive and complete study of the spin density in the prototype system p-O_2N-C_6F_4CNSSN helped to better understand the magnetic interaction mechanism, and therefore the magnetic behavior, in all the members of the serie p-X-C_6F_4CNSSN (X=O_2N, CN, Br, I), for which the packing is controlled by the substituent in the *para* position. This is due to the fact that the relative positions in the space of the interacting magnetic molecular orbitals, which have been determined to be located in the ring of the ·CNSSN, control the nature and strength of the magnetic interactions.

In Figure 1.4 the relative positions of the magnetic orbitals of the rings ·CNSSN from two different molecules of p-O_2N-C_6F_4CNSSN. Because the quasi-null overlapping of the magnetic orbitals, the magnetic interactions between those molecules must be ferromagnetic.

Enhancement of the magnetic interaction constant by spin delocalization in the family $A_2FeX_5{\cdot}H_2O$ (A=K, Rb, X=Cl, Br). As mentioned in the preceding sections, these series of low anisotropy AF showed magnetic LRO at relatively high temperatures ($T_C \geq 10$ K) [39] compared with other hydrated salts of transition metal ions $Cs_2FeCl_5{\cdot}4H_2O$ ($T_C = 0.185$ K [93]) or $Cs_2MnCl_4{\cdot}2H_2O$ ($T_C = 1.8$ K [94]) with similar coordination and with similar, or even shorter, magnetic super-exchange pathways. In $A_2FeX_5{\cdot}H_2O$ there are five different possible magnetic interactions which are propagated through two super-exchange pathways, which consist of double bridges of the sort $Fe-X\cdots X-Fe$ or $Fe-O-H\cdots X-Fe$. These super-exchange pathways, which will be explained in detail later in this chapter, are surprisingly effective in transmitting the magnetic interaction that results in relatively high transition temperatures.

The knowledge of the spin density distribution in the $A_2FeX_5{\cdot}H_2O$ series allows the determination of whether the relatively high magnetic transition temperatures are due to an important spin delocalization from the iron ion toward the ligand atoms. The existence of such a spin delocalization, which would strengthen the interaction between magnetic orbitals localized in different octahedra, is also supported by a reduced magnetic moment observed with neutron powder diffraction experiments at the Fe^{3+} site, (3.9(1) μ_B and 4.06(5)μ_B for $K_2FeCl_5{\cdot}H_2O$ and $Rb_2FeCl_5{\cdot}H_2O$, respectively) far below the $5\mu_B$ expected for the saturated magnetic moment of the Fe^{3+} [95].

Polarized neutron diffraction experiments, done at the D23 instrument from the ILL, on $K_2FeCl_5{\cdot}H_2O$ and $Rb_2FeBr_5{\cdot}H_2O$ were performed to corroborate the hypothesis [96]. In this case, the *Flipping Ratios* were analyzed with the Maximum Entropy Method [97] and with a multipolar expansion of the spin magnetization and it was demonstrated that the entity [$FeX_5{\cdot}H_2O$] is much more effective at delocalizing the spin, $\sim 20\%$, than other $3d$ transition metal complexes aqua or halide coordinated [98–107]. As for iron compounds, in a Fe^{2+} compound, FeF_2, there is a 10% spin delocalization from the iron ion [108] and in a $[FeCl_4]^-$ complex the spin population of

the chlorine atoms is around 0.15 $\mu_{\rm B}$ [109]. Also Campo and co-workers [96] showed that the spin delocalization is larger for Br than for Cl atoms, which explains why the transition temperatures in the bromide compounds are higher than in their chloride analogs. It was found also that, inside the distorted octahedra [$FeX_5{\cdot}H_2O$], the shorter the distance between the halide (X) and the Fe ion, the higher the spin delocalization at the halide, except in the case of the halide forming part of the pathway $Fe-O-H\cdots X-Fe$, which define the most intense magnetic interaction constant, J_1, in these compounds.

This spin delocalization reflects the fact that the magnetic molecular orbitals are spread over the ligand atoms, thus enhancing the magnetic interactions through a super-exchange magnetic interaction mechanism. This enhancement of the magnetic interactions is the cause of the surprisingly high transition temperatures in this series of compounds.

Determination of atomic site susceptibility tensors

In the last section it was assumed that the magnetic field induced magnetization of the sample ($\vec{M}$) and the applied magnetic field ($\vec{B}$) were parallel, *i.e.* the magnetic anisotropy was negligible and therefore $\vec{M}=\chi\vec{B}$. However this condition is not every time satisfied. In these cases it is necessary to take into account the anisotropic susceptibility for each magnetic crystallographic site, the bulk magnetization being the sum vector of all of these. The formalism for calculating the magnetic scattering in these cases was developed by Gukasov and Brown in Ref. [110]. For example, for one magnetic ion located on site $d_{\rm m}$, the local induced magnetization will be $\vec{M}_{d_{\rm m}}=\tilde{\chi}^{d_{\rm m}}\vec{B}$, where $\tilde{\chi}^{d_{\rm m}}$ is the symmetric local susceptibility tensor for site $d_{\rm m}$ with the number of independent components given by the local symmetry of the site $d_{\rm m}$. An equivalent magnetic atom located at site p related to the site $d_{\rm m}$ by $\vec{r}_p=\tilde{g}_p\vec{r}_{d_{\rm m}}$, where the magnetic group symmetry operator is $\tilde{g}_p=\{\delta_p|\mathcal{R}_p|\vec{t}_p\}$, would have magnetization $\vec{M}_p=\tilde{\chi}^p\vec{B}=\mathcal{R}_p\tilde{\chi}^{d_{\rm m}}\mathcal{R}_p^{-1}\vec{B}$. Therefore, the magnetization distribution at the unit cell, considering only one magnetic atom at $\vec{r}_{d_{\rm m}}$ and its equivalents by symmetry ($d_{\rm m}$-orbit), reads

$$\vec{M}(\vec{r})=\sum_{p}^{d_{\rm m}-orbit} m_{d_{\rm m}}(\vec{r}-\tilde{g}_p\vec{r}_{d_{\rm m}})\mathcal{R}_p\tilde{\chi}^{d_{\rm m}}\mathcal{R}_p^{-1}\vec{B}, \tag{1.186}$$

where $m_{d_{\rm m}}(\vec{r})$ is the magnetization distribution (assumed spherical) around the atom $d_{\rm m}$ and p runs over the symmetry operators of the space group of the crystal that generates the atoms of the $d_{\rm m}$-orbit. The expression (1.186) can be easily generalized for several magnetic sites in the asymmetric unit cell. Therefore the magnetic structure factor becomes

$$\vec{M}_{\vec{q}}=\sum_{d_{\rm m}}^{N_{\rm au}} F_{d_{\rm m}}(q)\sum_{p}^{d_{\rm m}-orbit}\mathcal{R}_p\tilde{\chi}^{d_{\rm m}}\mathcal{R}_p^{-1}\vec{B}\ \mathrm{e}^{\mathrm{i}2\pi\vec{q}\cdot\tilde{g}_p\vec{r}_{d_{\rm m}}}, \tag{1.187}$$

where the $d_{\rm m}$ index runs over the magnetic atoms, the $F_{d_{\rm m}}(q)$ is the magnetic form factor for the $d_{\rm m}$-th atom. At most, six free parameters define the local susceptibility tensors $\tilde{\chi}^{d_{\rm m}}$. For some cases, when the magnetic atom occupies an special Wyckoff position, it is possible to add symmetry constraints, reducing the number of parameters, by imposing $\mathcal{R}_p\tilde{\chi}^{d_{\rm m}}\mathcal{R}_p^{-1} \equiv \tilde{\chi}^{d_{\rm m}}$ for those operations of the space group $\tilde{g}_p$ for which $\tilde{g}_p\vec{r}_{d_{\rm m}} = \vec{r}_{d_{\rm m}}$. The relationship between the bulk and site susceptibilities tensor is $\tilde{\chi}^{bulk} = \sum_{d_{\rm m}}\sum_p \mathcal{R}_p\tilde{\chi}^{pd_{\rm m}}$. The bulk susceptibility tensor transforms with the full symmetry of the crystallographic class.

The magnetic structure factor expressed in Eq. 1.187, parametrized with the components of the site susceptibility tensors, can be used to model the *Flipping Ratios* (Eq.1.182) which can be measured with polarized neutron diffraction experiments. These ideas were used to reinvestigate the magnetic structures of $Nd_{3-x}S_4$ and $U_3Al_2Si_3$ [110, 111].

The compound $Nd_{3-x}S_4$ crystallizes in the cubic space group $I\bar{4}3d$ in which the twelve Nd atoms occupy the Wyckoff position $12a$ with a local tetragonal symmetry $\bar{4}$ (3 sets of 4 Nd atoms with tetragonal axis parallel to each of the 3 main axis). Unpolarized neutron diffraction experiments with magnetic field parallel to one of the main axis demonstrated that there is a large difference between the magnetic moments found for the Nd located in the set with its tetragonal axis parallel to the field and the other 2 sets of $12a$. However, for an arbitrary orientation of the crystal with the magnetic field, no symmetry constraints on each Nd magnetic moment could be applied. The approach of the site susceptibility tensor, for this particular space group and Wyckoff position, implies that only to parameters are needed regardless of the field direction $\tilde{\chi}^{12a}_{11} = \tilde{\chi}^{12a}_{22} \neq \tilde{\chi}^{12a}_{33}$ and $\tilde{\chi}^{12a}_{12} = \tilde{\chi}^{12a}_{23} = \tilde{\chi}^{12a}_{13} = 0$. By measuring *Flipping Ratios*, it was possible to determine these 2 parameters: $\tilde{\chi}^{12a}_{11} = 1.45(5)\mu_{\rm B}$ and $\tilde{\chi}^{12a}_{33} = 0.55(5)\mu_{\rm B}$. These parameters represent an oblate susceptibility tensor for each one of the 3 sets of Nd in $12a$, each having its short axis parallel to the main axis on which it lies. The non-collinear distribution of Nd magnetic moments is not incompatible, however, with the bulk cubic symmetry of the crystal, since the vector sum of all magnetic moments remains parallel to the field, and invariant with respect to the field orientation.

$U_3Al_2Si_3$ crystallizes in the tetragonal body centered space group $I\bar{4}$ and the U atoms are sited in 3 different Wyckoff positions; U1 and U2 in $2a$, with tetragonal local symmetry, and U3 in $8c$, with triclinic symmetry. The system orders magnetically below $T_C = 36$ K, with propagation vector $\vec{K} = 0$, and previous neutron powder diffraction experiments seem to indicate, with good agreement factors, a collinear AF order for U1 and U2 sub-lattices and ferromagnetic order for the U3 one. However, this model, in which U1 and U2 are in similar Wyckoff positions, produces very dif-

ferent magnetic moment, for each of these Uranium atoms. Nevertheless, the local susceptibility approach shows clearly that, in the paramagnetic region, there is a strong elongation of the magnetic susceptibility tensors of U3 (prolate) along one of the (110)-type axes, which increases as the temperature decreases. In the ordered phase, a non-collinear structure emerges with magnetic moments pointing along the same (110)-type axes, giving a net ferromagnetic moment in the *ab*-plane. On the contrary, the U1 and U2 atoms show a rather low local susceptibility, suggesting that these atoms have small moments, characterized by nearly spherical magnetic ellipsoids, indicating low local anisotropy. The absence of ordering in the U1, U2 sublattices at low temperatures must be attributed partly to the low moment, and partly to the fact that the first magnetic neighbor of either U1 or U2 atoms is far away.

1.9 Spherical Neutron Polarimetry

In the previous section the polarization of the incoming and scattered neutron beam, respectively $\vec{P}_i$ and $\vec{P}_f$, was fixed to be parallel or antiparallel to a given direction ($\hat{z}$) following the experimental method developed by Moon et al. [86]. However, this method cannot distinguish a rotation of the neutron polarization vector from a change in its modulus. This is the reason why the method of three-dimensional analysis of polarization (or spherical neutron polarimetry, SNP) was developed. Basically, the idea is to implement experimentally the second Blume-Maleev equation (1.172) [112–114].

However, it was in 1989 when Tasset and his colleagues developed at the ILL the instrument called CRYOPAD, which allowed the three-dimensional analysis of the polarization at large scattering angles [115, 116]. In CRYOPAD the neutron beam can be initially polarized, $\vec{P}_i$, in the three orthogonal directions $\hat{x}$, $\hat{y}$ and $\hat{z}$, (righ-hand coordinate system). The scatterer (sample) is placed in zero magnetic field, and the three components of the polarization vector of the scattered neutrons, $\vec{P}_f$, are measured for each initial $\vec{P}_i$ and for a given scattering vector $\vec{q}$. This conforms the polarization tensor $\tilde{P}_{fi}$, where the indices f and i refer to the *final* and *initial* polarizations. For example, it is possible to measure the diagonal components $\tilde{P}_{fi}^{xx}$, $\tilde{P}_{fi}^{yy}$ and $\tilde{P}_{fi}^{zz}$, the same determined in the linear polarization analysis, and the non-diagonal components ($\tilde{P}_{fi}^{yx}$, etc.), related to a polarization rotation in the scattering event. The SNP, some times also called zero-field polarimetry, allows the determination of complex magnetic structures. Domain structures and the effect of external influences can also be studied [117–121]. Another advantage of SNP (also valid for linear neutron polarimetry) is that the measured data, to a good approximation, are not affected by extinction effects. In the next subsections several applications of this technique will be highlighted.

Proving the magneto-electric coupling in the molecular multiferroic $(NH_4)_2FeCl_5{\cdot}H_2O$

As explained in the previous sections, the compound $(NH_4)_2FeCl_5{\cdot}H_2O$ has been described as a molecular *improper* multiferroic [35, 67, 69, 71, 122]. However, from the macroscopic characterization and the unpolarized neutron diffraction experiments it was not posible to elucidate the nature of the magnetic phase observed between $T_{FE} = 6.9$ K and $T_N = 7.2$ K. In fact, it was supposed, by analogy with the archetypical compound $TbMnO_3$ where two order parameters condense successively at T_{FE} and T_N [66], that it should correspond with a sinusoidal modulated magnetic phase, either parallel to the $\vec{a}$ or to the $\vec{c}$ axes, respectively labeled with the irreps Γ_1 or Γ_2 of the little group of the propagation vector $\vec{K}_0 = (0\ 0\ 0.23)$ in $P2_1/c$. This would correspond to a transition on warming from a cycloidal ($T < T_{FE}$) to a collinear sinusoidal AF structure ($T_{FE} < T < T_N$), the latter being compatible with the absence of electric polarization. Furthermore, the symmetry at the multiferroic phase below T_{FE} was unclear.

Rodríguez-Velamazán [123] did SNP experiments in $(NH_4)_2FeCl_5{\cdot}H_2O$ under an applied electric field ($\vec{E}$), to explore the possibility of controlling the *hand* of the cycloidal magnetic domains, and therefore, the electric polarities. These experiments allowed the determination of the absolute magnetic configuration and domain population of this system, under different applied external fields $\vec{E}$. In fact, for this compound, the term $\tilde{P}_{fi}^{yx}$ gave the information about the domain population. The experiment showed that the system is completely switchable, which represents a direct evidence of its magneto-electric coupling. Moreover, SNP data were used to refine the previously proposed magnetic structure of the ground state ($T < T_{FE}$), obtaining a more accurate magnetic structure model. In fact the group $P11'(\alpha\beta\gamma)0s$ is the only compatible symmetry with the measured polarization tensor $\tilde{P}_{fi}$. Finally, the existence of a collinear sinusoidal magnetic phase with moments parallel to the $\vec{a}$ axis in the temperature region $T_{FE} < T < T_N$ was confirmed by the sign of the term $\tilde{P}_{fi}^{yy}$, which is negative.

Elucidating the magnetic order in GdB_4

The family of compounds RB_4 attracted a huge interest in the past for their interesting physical properties (LRO, mixed valence, heavy fermion behavior, etc...). For example, the presence of magneto-electric coupling in GdB_4 was proposed, assuming that the inversion center was combined with the time reversal operation and a zero propagation vector $\vec{K} = 0$ with AF behavior [124, 125]. Also, in resonant X-ray scattering experiments at the Gd-L_3 edge some interference between magnetic and anisotropic charge contributions was observed, which was compatible with several magnetic models for GdB_4 [126]. Blanco *et al.*, in an elegant and easy way, shed

light on these questions by using SNP [127]. In the next paragraphs this instructive example will be summarized.

This compound crystallizes in the tetragonal space group $P4/mbm$, in which 4 Gd ions occupy the Wyckoff position $4g$ with point symmetry $m2m$, whereas the 16 B atoms are in $4e$, $8j$ and $4h$. From macroscopic measurements (Heat Capacity, Magnetic Susceptibility, etc..) it was well known that the system ordered AF below $T_N < 42$ K and that all the magnetic moments resided on the ab-plane. The resonant X-ray experiments did not discern between collinear or non-collinear arrangements of the magnetic moments [128], but electrical resistance experiments seemed to indicate some non-collinear model [129]. Despite all these experimental findings, the magnetic structure was not determined with neutron scattering because of the strong absorption of both B and Gd natural especies. However, Blanco *et al.* grew a ^{11}B enriched single crystal to undertake SNP experiments, at very short wavelength in order to minimize the absorption effects, and to find out the magnetic structure unambiguously [127]. At low temperature, they found a propagation vector $\vec{K} = 0$ and measured the polarization tensors $\tilde{P}$ for different set of reflections ($h0l$ and $hk0$), finding that the off-diagonal terms were null within the experimental error. Another significant feature was the non observation of scattering for the lines $hh0$ and $h\bar{h}0$ (*i.e.* $\tilde{P}_{fi}^{xx} \sim \tilde{P}_{fi}^{yy} \sim \tilde{P}_{fi}^{zz} \sim 1.0$), which was only compatible with a non-collinear model of AF pairs parallel to the [110] and [1$\bar{1}$0] directions. The complete analysis of all the polarization tensors, using the magnetic symmetry models derived from the space group $P4/mbm$ with $\vec{K} = 0$, gave unequivocally the Shubnikov group $P4/m'b'm'$, with a Gd magnetic moment equal to 7.14(17) μ_B, as model for the magnetic order in GdB_4.

1.10 Small Angle Neutron Scattering in Magnetism

Small Angle Neutron Scattering (SANS) is a widely employed technique for microstructure determinations in several disciplines, such as materials science, physics, chemistry, biology, etc... The reason is that SANS is one of the few experimental methods available to probe mesoscopic length-scales in the real space (from 1-300 nm) and in bulk materials. In addition, the spin of the neutron confers to the SANS the possibility to study magnetic phenomena and materials in the nano and mesoscopic scales with high sensitivity. SANS is often utilized complementarily to other magnetic image and surface techniques like, Lorentz Transmission Electron Microscopy, Magnetic or Atomic Force Microscopy, Kerr Effect Magnetization, Scanning Tunneling Microscopy with spin polarization, etc...

Magnetic SANS techniques are employed to study different magnetic materials: magnetic nanoparticles, magnetic steels, hard and soft magnets, magnetic oxides, ferrofluids, metallic alloys, magnetic skyrmions, chiral soli-

tons and helical order in non centro-symmetric magnets, vortex in type II superconductors, etc.... In a recent review [130], detailed information on the applications of magnetic SANS in magnetic materials can be found. In this section only several examples, related to magnetic textures, will be explained in more detail. Additionally, in the previous chapter, other examples related to the use of SANS to study magnetic materials have been described.

The expressions governing the SANS cross sections for unpolarized or polarized neutrons are basically the Blume-Malayev equations (1.168) and (1.169) introduced in the previous sections and adapted to the common SANS configurations ($\vec{B} \parallel \vec{k}_i$ or $\vec{B} \perp \vec{k}_i$). In Figure 1.5 these configurations are schematized for typical experiments on skyrmion lattice studies.

In addition, the discrete nature of the matter has no relevance for the length-scales accessible with SANS and therefore the magnetization on each atom $\vec{M}_{d_{\mathrm{m}}}$ is replaced by a continuous vector field $\vec{M}(\vec{r})$. The magnetic SANS signal will reflect the variation of the magnetization, in modulus and orientation, at the nano-scale length. Then the *Magnetic Structure Factor* vector ($\vec{M}(\vec{q})$) employed in SANS is the Fourier Transform of the field $\vec{M}(\vec{r})$. In a similar way, the scalar *Nuclear Structure Factor* ($N(\vec{q})$) is defined by using a *scattering length density* $b(\vec{r})$ instead of the atomic b_n. Therefore we get:

$$\vec{M}(\vec{q}) = \int d^3r \ \vec{M}(\vec{r}) \ \mathrm{e}^{-\mathrm{i}2\pi\vec{q}\cdot\vec{r}}, \tag{1.188}$$

$$N(\vec{q}) = \int d^3r \ b(\vec{r}) \ \mathrm{e}^{-\mathrm{i}2\pi\vec{q}\cdot\vec{r}}. \tag{1.189}$$

The sample scattering volume appears at SANS cross sections via a constant $K = V^{-1}p^2$, where p was defined in section 1.2.5.

In the next subsection an example related to vortex matter will be presented in order to illustrate the power of the magnetic SANS.

Stroboscopic SANS experiments on skyrmionic lattices (SKL)

Skyrmion textures, which are topologically protected nanometric vortex-like magnetic objects, that have been discovered in cubic magnets without inversion symmetry (MnSi [131], $Fe_{1-x}Co_xSi$ [132], FeGe [133], Cu_2OSeO_3 [134, 135]), were theoretically predicted a long time ago by the Bogdanov seminal studies [136, 137]. However, the stability of the skyrmion lattices (SKL) has been studied only in a limited way, mostly concerning with radial or elliptic stability [136, 138]. Hence, solitonic configurations that are considered stable or metastable may actually be unstable due to some mode that is non homogeneous along the magnetic field direction. Closely related to the stability analysis is the idea that some metastable state may become

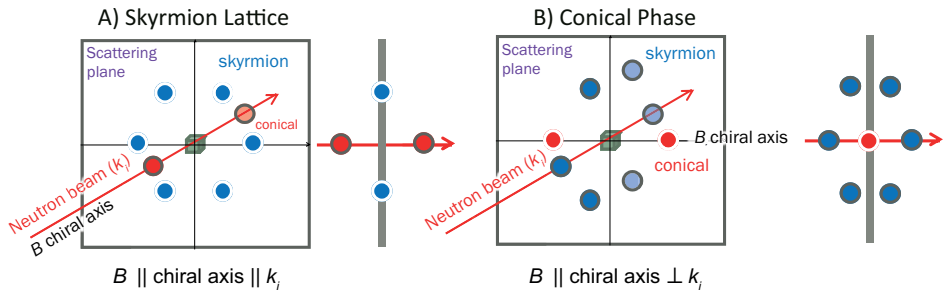

Figure 1.5: Scheme showing the typical SANS configurations to observe the Skyrmion Lattice (A) and the Conical Phase (B) in cubic chiral helimagnets. Blue (A) and red (B) spots are observed at the neutron detector related, respectively, with the hexagonal packing of the SKL and the Conical phase with propagation vector parallel to the field ($\vec{B} \parallel \vec{K}$)

the equilibrium state by virtue of the thermal fluctuations. These two related problems, the stability of stationary points and the effect of thermal fluctuations at relatively low temperatures, are addressed in Ref. [139] and, as a result, it is shown that the low T phase diagram $B - T$ contains an unexpected new SKL phase.

Nakajima *et al.* [140, 141] by using stroboscopic SANS measurements in single crystals of MnSi at the *time-of-flight* instrument TAIKAN located at the Spallation Neutron Source (MLF) in Japan, explored the low temperature region of the phase diagram. By appropriately synchronizing the neutron and electrical current pulses (which are employed to create temperature ramps in the sample) with the neutron 2D-detector, it is possible to study the time evolution of SANS patterns with a resolution of 30 ms. The employed set-up allowed to cool down the sample temperature with a rate of 100 K s^{-1}.

The skyrmion lattices are usually visible in SANS experiments under the configuration for which the magnetic field is parallel to the incoming neutron beam ($\vec{B} \parallel \vec{k}_i$). This is schematized in Figure 1.5 A) and show the six-fold typical pattern of an hexagonal lattice. However, the two spots defining the conical state are observed when the propagation vector of the helix, which is often parallel to the magnetic field, is perpendicular to the beam ($\vec{B} \parallel \vec{K} \perp \vec{k}_i$). See Figure 1.5 B). When the SKL is observed in $\vec{B} \parallel \vec{k}_i$ no signal appears in $\vec{B} \perp \vec{k}_i$ and reciprocally for the conical state. The crystal studied by Nakajima *et al.* was aligned with its (0 0 1) axis parallel to the horizontal magnetic field and the (1 1 0) in the vertical.

Nakajima *et al.* explored the phase diagram by doing measurements in equilibrium and also by doing fast quenching from the paramagnetic state, passing through the *A-phase*, to the low T region. At some values in the $T - B$ plane SANS data were also collected. Metastable SKL states were

captured at low T, in agreement with [139] and also a magnetic phase transition from triangular to square SKL was identified with decreasing magnetic field at low temperatures.

1.11 Magnetic Inelastic Scattering

The previous sections have been dedicated to describing different applications of neutron scattering based on the measurement of the nuclear or the magnetic elastic coherent part of the double differential cross sections, i.e. the incoming neutron exchanges momentum with the sample but it does not exchange its energy. However, there are also nuclear and magnetic inelastic coherent parts, which are very small but which wear very important information about the collective excitations of atomic or magnetic origin (e.g. phonons, spin-waves, etc...).

In magnetically ordered systems, each magnetic moment deviates from its equilibrium position along a particular direction. However, these deviations cannot be arbitrary because the magnetic moments are coupled. Basically it produces collective coherent deviations, also called spin-waves (see section 1.3.2). As illustrated in section 1.3.2, by using the second quantization picture it is possible to obtain the single quantum (the *magnon*), and its energy $E(\vec{q})$ (dispersion relations), where $\vec{q}$ is a vector of the Brillouin Zone that labels each magnon. By using linear approximations, valid when the deviations with respect to the magnetic moment are small, (low temperatures and/or large enough magnetic moment), it is easy to demonstrate that $E(\vec{q})$ is related to the Fourier transform of the magnetic exchange interaction constants J_{l,d_m} between the different magnetic atoms d_m at different lattices l. The number of branches, acoustic or optic, depends on the number of independent magnetic atoms in the unit cell and their degeneracy is related to the multiplicity of each magnetic orbit.

It has been found that this formalism is also appropriate to reasonably describe the spin-waves in $3d$ transition-metal magnets. In AF materials it is found that the dispersion relations are linear in q for small q and, depending on the ion anisotropies, several gaps are opened at $\vec{q} = 0$.

On the other hand, the spin-wave dispersion relations are considered as the finger-print to understand the superconductivity. For example, in related materials like the *pnictides* and *chalcogenides* it seems that there exist some recognizable pattern in the next nearest neighbors magnetic interactions even if the first neighbors interactions are completely different.

Moreover, when the crystal field produced by electrostatic interactions with surrounding atoms is predominant, the energy levels of a magnetic atom are minimally dispersive. In these cases, it is possible to use inelastic neutron scattering to determine those energy levels assuming that they are

accessible by magnetic dipolar transitions[14]

An intermediate case, between isolated magnetic centers and extended magnets, happens for magnetic clusters formed by several atoms magnetically coupled inside of a molecule (e.g. SMM, metallo-proteines, phthalocianines, etc...). These objects can be prepared in a highly controlled manner, via chemical routes, and often they allow the study of new magnetic quantum phenomena.

The next two examples will illustrate how to determine the hierarchy between different magnetic interaction constants in the family $A_2FeX_5{\cdot}H_2O$ (A=K, Rb, X=Cl, Br) and how to determine the parameters in the spin Hamiltonian in SMM (e.g. Mn_{12}-acetate and Fe_8). Both systems have been described in preceding sections.

Understanding magnetic interactions in $K_2FeCl_5{\cdot}D_2O$

The aim of this example is to go a step further in the understanding of the magnetic interaction mechanisms in this series of compounds by determining the magnetic coupling constants [142]. The analysis of the five magnetic coupling constants, particularly the comparison between magnetic interactions including and not including oxygen atoms in the super-exchange pathways, contribute to the understanding of the relative importance of two influential factors on the strength of the magnetic interaction: i) the spin population on the ligand atoms (see the example in the section 1.8) and ii) the distances between the two ligand atoms in the magnetic super-exchange pathways transmitting the magnetic interaction.

Therefore, in this example, after determining all the possible magnetic interactions from an analysis of the nuclear structure, previously determined by using single crystal neutron diffraction experiments, which allowed us to locate accurately the position of the oxygen and the hydrogen atoms, the study of the magnetic coupling constants determined by inelastic triple axis neutron spectroscopy (TAS) are reported.

The unit cell of $K_2FeX_5{\cdot}D_2O$ has been described in section 1.6.2. In this structure there are five possible magnetic interactions between an iron ion and its first shell of neighbour Fe ions. Figure 1.6 A) represents the unit cell of $K_2FeCl_5{\cdot}D_2O$, whereas Figure 1.6 B) shows a scheme of the five magnetic interactions projected on the *ac*-plane together with the magnetic structure.

The inelastic neutron scattering experiment was performed on the three-axis spectrometer IN12 at the ILL. In order to determine the magnon dispersion curves, constant-q scans along the $(0\ 1\ \zeta)$, $(0\ 1+\zeta\ 0)$, $(0\ \frac{3}{2}\ \zeta)$, $(0\ 1+\zeta\ \zeta)$, $(0\ 0\ 1+\zeta)$ and $(\zeta\ 0\ 1)$ directions were performed at 1.6 K, temperature much lower than the Néel temperature of 14.06 K. The measured directions in the reciprocal space were selected in order to have a correct description of the first Brillouin Zone (BZ). See Figure 1.6 C).

[14] $\Delta M_S = \pm 1$

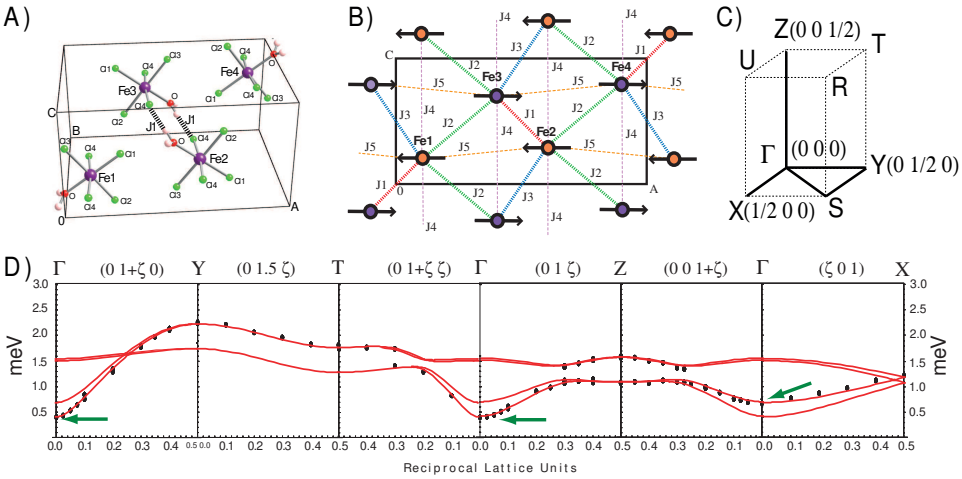

Figure 1.6: A) Structure of $K_2FeCl_5{\cdot}D_2O$. The potassium atoms have been omitted for clarity. The halogen labels are represented in all the octahedra together with the label for the 4 iron ions: Fe1(x, y, z), Fe2$(\frac{1}{2}+x, \frac{1}{4}, \frac{1}{2}-z)$, Fe3$(\frac{1}{2}-x, \frac{3}{4}, \frac{1}{2}+z)$, Fe4$(-x, \frac{3}{4}, -z)$. B) Scheme of the five magnetic interactions projected on the *ac*-plane. Thick lines represent interactions connecting a Fe ion with two other Fe ions, one with $y+\frac{1}{2}$ and the other with $y-\frac{1}{2}$. The magnetic structure is also shown. Orange circles correspond to Fe ions with $y=\frac{1}{4}$ whereas pink circles $y=\frac{3}{4}$. C) High symmetry points of the first BZ together with the different directions that have been measured (thick lines). D) Experimental points measured for each direction of high symmetry at the BZ. The red line is the fit of te points to a linear spin-wave model including uniaxial and rhombic anisotropies.

A gap in the energy is observed in the low energy magnon branch at the center of the zone (Γ). Moreover, an additional feature in the dispersion curves is that this energy gap appears to be split in the different Brillouin zones, around 0.38 meV and 0.58 meV in the (0 1 0) and the (0 0 1) zones respectively. This different gap can be observed in Figure 1.6 D) indicated with green arrows. Therefore, a model with a rhombic magnetic anisotropy term is needed in order to correctly fit the different gaps. The Hamiltonian which includes this rhombic magnetic anisotropy is:

$$\mathcal{H} = -\sum_{l,l',d_{\rm m},d'_{\rm m}} J_{ld_{\rm m},l'd'_{\rm m}} \vec{\mathbb{M}}_{ld_{\rm m}} \cdot \vec{\mathbb{M}}_{l'd'_{\rm m}} - \sum_{ld_{\rm m}} \sigma_{d_{\rm m}} A_{d_{\rm m}} \mathbb{M}^z_{ld_{\rm m}} - \sum_{ld_{\rm m}} E_{d_{\rm m}} \left[\left(\mathbb{M}^x_{ld_{\rm m}}\right)^2 - \left(\mathbb{M}^y_{ld_{\rm m}}\right)^2 \right]. \tag{1.190}$$

The magnetic exchange coupling constants obtained, after fitting all the experimental dispersion curves to the relation $E(\vec{q})$ derived from Hamiltonian expressed in the equation (1.190), are $J_1 = -0.113(3)$, $J_2 = -0.037(1)$,

$J_3 = -0.032(3)$, $J_4 = -0.023(2)$, $J_5 = -0.025(2)$ meV. The values of the variable $A_{d_{\rm m}}$ and $E_{d_{\rm m}}$ were 0.073 meV and 0.0072 meV respectively, which gives an axial anisotropy $D = 0.0146$ meV. The experimental and fitted dispersion curves are depicted in Figure 1.6 D).

The results of this study can be related to other studies of several magnetic phenomena of this AF series: i) The energy gap at the Γ point in the magnon dispersion curves is in good agreement with the energy gap calculated from an analysis of the boundaries of the magnetic phase diagram [41]. ii) The physical interpretation of the two different energy gaps at the Γ point implies that the hardest magnetic axis is the $\vec{b}$-axis. The same conclusion is deduced from the magnetic structure in the spin-flop phase in which the magnetic moments are collinear to the $\vec{c}$-axis [47]. iii) The magnetic structures determined from the values of the magnetic coupling constants correspond to the experimental magnetic structure. iv) Estimation of the Neel temperatures using a mean field approach results in values close to the experimental ones. v) The values of the magnetic interactions also explain the magnetic dimensionality crossover observed in the heat capacity and magnetic measurements [40].

Neutron spectroscopy in magnetic molecular clusters

The interest of SMM, like Mn_{12}-acetate, has already been introduced in subsection 1.7. In these materials, the knowledge of the magnetic anisotropy of the clusters, which is assumed to be much smaller than the exchange energy, is central to understanding how the quantum tunneling of the magnetization (QTM) can occur. With uniaxial anisotropy, the energy levels of a cluster depend on the orientation of the spin S relative to its anisotropy axis. However, for QTM to be allowed, the rotational symmetry about the z axis must be broken by small high-order spin terms. The general Hamiltonian in expression (1.191), where quadratic and quartic terms in $\tilde{S}$ are included, describes appropriately the energy levels in Mn_{12}-acetate and Fe_8 SMM:

$$\mathcal{H} = D\big[\mathbb{S}_z^2 - \frac{1}{3}S(S+1)\big] + E\big[\mathbb{S}_x^2 - \mathbb{S}_y^2\big] + B_4^0\mathbb{O}_4^0 + B_4^2\mathbb{O}_4^2 + B_4^4\mathbb{O}_4^4 \quad (1.191)$$

where the operators $\mathbb{O}_4^0$, $\mathbb{O}_4^2$ and $\mathbb{O}_4^4$ are defined as:

$$\mathbb{O}_4^0 = 35\ \mathbb{S}_z^4 - [30S(S+1) - 25]\,\mathbb{S}_z^2 - 6S(S+1) + 3S^2(S+1)^2$$

$$\mathbb{O}_4^2 = \frac{1}{4}\left\{\big[7\mathbb{S}_z^2 - S(S+1) - 5\big]\big(\mathbb{S}_+^2 + \mathbb{S}_-^2\big) + \big(\mathbb{S}_+^2 + \mathbb{S}_-^2\big)\big[7\mathbb{S}_z^2 - S(S+1) - 5\big]\right\}$$

$$\mathbb{O}_4^4 = \frac{1}{2}\left(\mathbb{S}_+^4 + \mathbb{S}_-^4\right)$$

Thus, to validate the different theories of QTM, the knowledge of the transversal anisotropy parameters (B_4^0, B_4^2, B_4^4) in the spin Hamiltonian is very important, whose precise determination requires a suitable experimental technique. The advantage of Inelastic Neutron Scattering over other techniques,

like High Field Electron Paramagnetic Resonance (EPR), is that it is not necessary to perturb the system by applying a magnetic field and it can give a detailed picture of the scheme levels from a straightforward analysis.

The cluster $[Fe_8O_2(OH)_{12}(tacn)_6]^{8+}$ (in short Fe_8) is a molecule formed by 8 Fe^{3+} ions in a planar butterfly geometry giving a $S = 10$ due to the AF coupling between the Fe ions. Cacciuffo *et al.* employed INS techniques in non-deuterated powder of Fe_8 at low temperatures ($1 \leq T \leq 10$ K) at the Time of Flight spectrometer IN5 of ILL working with a resolution of 19 μeV with the aim to determine the different parameters defining the spin-Hamiltonian of this cluster [143].

The ground level, $|S = 10; M = \pm 10\rangle$, is the only one populated at the lowest temperature. As the temperature increases, other levels start to be populated, being the next one the $|S = 10; M = \pm 9\rangle$. The uniaxial and rhombic anisotropy parameters (D, E) mainly control the energy distance between the lowest levels whereas the other parameters (B_4^0, B_4^2, B_4^4) are involved in some mixing of the upper energy levels ($|S; M\rangle$ with $|M| \leq 6$) less distant among them. Usually these levels are populated at the highest temperatures. In fact, the position of the peaks at the energy transfer axis gives directly the eigenvalues of the Hamiltonian (1.191) (which depends on the parameters) whereas the intensity of the peaks is related to the wave function of the eigenvectors. Therefore, in principle, it is possible to obtain the values of the parameters by fitting the peaks positions.

Cacciuffo *et al.* found $D = -25.2(2)\mu$eV and $E = -4.02(3)\mu$eV and to fit correctly all the measured peaks it was needed to include the quartic terms of the Hamiltonian giving the values $B_4^0 = 0.87(6)10^{-4}\mu$eV, $B_4^2 = 0.1(1)10^{-4}\mu$eV and $B_4^4 = 7.4(6)10^{-4}\mu$eV. These values produced an energy barrier $A/k_B = 32.8(1)$ K slightly higher than the one reported from ac susceptibility experiments and demonstrated the importance of the $\mathbb{O}_4^4$ operator, which is related to the transverse anisotropy, in the tunneling processes.

In Mn_{12}-acetate, Mirebeau *et al.* also measured the energy levels by using the INS techniques [144]. Their main result was the precise determination of the coefficient B_4^4 in the non diagonal transverse term (in Mn_{12} the tetragonal symmetry does not allow the presence of the term $\mathbb{O}_4^2$ in the Hamiltonian). The presence of the $\mathbb{O}_4^4$ term was searched for by many experimentalists, since only components that do not commute with S_z could induce tunneling with $\Delta M = \pm 4$, as observed experimentally in the magnetization experiments.

In the 2000's the extrinsic interactions, arising from disorder, were proposed as the dominant sources of QTM in Mn_{12} nanomagnets [145]. However, Carbonera *et al.* presented a detailed study of the effects that crystalline disorder has on the QTM of Mn_{12}-benzoate SMM. The authors were able to isolate the influence of long-range crystalline disorder thanks to the absence of interstitial molecules in the crystal structure of this molecular

compound. For this, they compared inelastic neutron scattering results obtained at IN5 under two extreme situations: a crystalline sample and a nearly amorphous material. Results showed that crystalline disorder weakly affects the anisotropy and other parameters in the spin Hamiltonian, and therefore has a little effect on the quantum tunnelling of these materials. It follows that disorder is not a necessary ingredient for the existence of QTM [146].

1.12 Other Neutron Scattering Techniques

This section is intended to briefly explain other neutron scattering techniques that are increasingly being employed to solve problems in magnetism. They give access to the very small energy transfers and therefore allows the study of slow dynamics. An example on the use of neutron reflectometry technique to characterize magnetic surfaces will be also illustrated.

1.12.1 Quasielastic Neutron Scattering

In the previous sections it has been explained that the Scattering Law can be split in coherent and incoherent parts. The first one is related to the correlations in time and in space of pair of scatterers whereas the second is about self correlations of scatterers. It means that the coherent part is related to the structure (elastic) and the collective movements or excitations (inelastic). However, the incoherent part gives information about the individual dynamics of nuclei (vibrations, rotations or translations) and magnetic moments.

Due to the large incoherent cross section of hydrogen, compared with other isotopes, the scattering cross sections measured in hydrogenated samples are dominated by the incoherent part and therefore neutron scattering techniques are ideal to characterize the individual movements of hydrogen in these samples. When the movement can be decoupled in vibrations, rotations and translations then it is possible gain access to the quasi-elastic scattering function whose width is related to the characteristic times of the movements in the range 10^{-10} to 10^{-12} seconds. The intensity of the elastic part of this incoherent signal gives information about the geometry of the movements. More detailed information on quasi-elastic neutron scattering can be found in [147]. Here a simple example on the use of these techniques, involving magnetic molecules, will be commented.

Rodríguez-Velamazán *et. al* [148] applied quasi-elastic neutron scattering techniques, together with solid state ^{2}H-NMR, to characterize, as a function of temperature, the rotational movement of the pyrazine rings in the spin crossover molecular compound {Fe(pyrazine)[Pt(CN)$_4$]}. In this compound, the Fe ion can switch between high and low spin states at temperatures ∼285 K and ∼309 K for decreasing or increasing the temperature

respectively. The structural studies at low temperatures, in the low spin state, showed some anomalous elongation at the Debye-Wallers factors at the hydrogen atoms of the pyrazine rings. This fact could be an indication of some structural or dynamical disorder present in the materials. In this sense, quasi-elastic neutron scattering techniques can help to elucidate the origen of the disorder.

They demonstrate experimentally that the bistability between rotation and blocking of the pyrazine rings connecting the Fe ions arranged in different planes is accompanied with the change between high and low spin state. The rotation in the high spin state is described as a 4-fold jump motion about the nitrogen axis coordinated with the Fe ion. In the low spin state, the rotation is suppressed. They also observed that when benzene molecules are incorporated in the system the pyrazine movements are restricted.

1.12.2 Neutron Spin Echo Techniques

In 1972 F. Mezei published his pioneering work establishing the grounds for the Neutron Spin Echo techniques [149]. The very basic idea behind these techniques is the Larmor precession of the polarization of the neutron beam when neutrons travel along a distance L with an uniform magnetic field perpendicular to the polarization. If the neutron travels again through a second region with the same length L but with opposite magnetic field, then the dephasing precession angle turned in the first region is deturned in the second one, giving a zero total dephasing precession angle. However, if a sample is put in between both opposite magnetic field regions, some neutrons will exchange energy with the sample and therefore will change their velocities before entering the second region producing a different dephasing precession angle. As a result, the sample could produce an easily measurable non zero dephasing angle for all neutrons.

It can be easily demonstrated that these techniques allow to measure directly the Intermediate scattering function $I(\vec{q}, t)$, defined in Eq. (1.58), which measures the time correlations of the sample. Typically, the accessible time ranges go from picoseconds to microseconds, which correspond to hundredths of μeV to several neV energy exchanges within the sample. Moreover, the energy transfer can be determined with very high precision (10^{-5}) without using severe conditions at the monochromator. Detailed descriptions of these techniques can be found in [150, 151].

In the previous paragraphs we assumed that the neutron spin does not change in the scattering process, which is true for non-magnetic nuclear interaction. When applying these ideas to magnetic materials, where the magnetic interactions can change the polarization state, we need to consider the magnetic field that the neutrons will feel when traveling through the sample, which is basically the *magnetic interaction vector* $\vec{M}_{\perp\vec{q}}$. It is also necessary to bear in mind how to control the effects of beam depolarization

by the different magnetic domain distributions.

The next example will illustrate one of the most employed applications of NSE in magnetism, which is the measurement of relaxation times in spin glasses. In fact, the time correlations of the magnetization close to the glassy transition (T_g) has been the object of discussions and controversy over the last few decades. This has often been characterized by a stretched exponential function $\sim \exp\{-(t/\tau)^{\beta}\}$, but when self similarity (i.e. fractal behaviour) occurs this function does not describe adequately the structural or magnetic relaxation. Then a modified function, which phenomenologically describes the Monte Carlo calculations by incorporating a power law, $q(t) = \langle S_i(0)S_i(t)\rangle \propto t^{-x}\exp\{-(t/\tau)^{\beta}\}$, is employed. The implications of such a non-exponential function opens the necessity of to think about global models that may lead to hierarchical relaxation. In this context Weron, [152] proposed a generalized function, $\varphi(t) = \{1 + k(t/\tau)^{\beta}\}^{-1/k}$, where k is a parameter accounting for effective interactions and β is related to the self similarity concept, that can be adapted easily to spin glass dynamics and, in the limit $k \to 0$, reduces to the exponential function.

The validity of the model based in the generalized relaxation function was investigated in the archetypal metallic spin glasses $Cu_{1-x}Mn_x$ (x=0.1, 0.16, 0.35) and $Au_{1-x}Fe_x$ (x=0.14) with Neutron Spin Echo experiments in [153] accessing to time scales from 0.002 to 1 ns . The authors measured the intermediate function ($I(\vec{q},t)$) at several temperatures and q values. All the spectra were independent of q and well described with the Weron function with consistent physically meaning parameters, for both samples. In turn, the k parameters obtained from the fits to the Weron function are related to the sub-extensivity parameter $\tilde{q}$ of models with non extensive entropy for complex and multifractal systems giving a $\tilde{q} \sim 5/3$ parameter at the spin glass transition temperature T_g. It seems that the spin glass system evolves from an extensive Boltzmann-Gibbs thermodynamics at high temperatures to a sub-extensive dynamics at T_g.

1.12.3 Neutron Reflectivity

Since the pioneering work of Felcher *et al.* in the early 1980s [154] about the neutron reflectivity grounds, these techniques have reached a mature state and nowadays neutron reflectometers are fundamental instruments in all types of neutron sources, pulsed and steady state sources. Due to their great power, these techniques are applied to the study and characterization of a wide range of phenomena and materials, mainly in soft matter and nanomagnetism areas. In fact, there are scientific topics in nanomagnetism that can only be addressed with neutron reflectivity; e.g. magnetization depth profiling, magnetic structures in multilayers and heterostructures, interdiffusion, magnetic domains, magnetic nanoparticles, study of patterned nanostructures, etc... In this section we will focus only on some applications

of these techniques in thin films. For a more extended review we refer to the nice chapter of Toperverg and Zabel in [155].

X-ray reflection by matter can be understood by means of the refractive index of the matter for X-rays photons. In electromagnetism theory the refractive index is related directly to the electron density of the material, which is at the origin of the interaction potential of the X-ray scattering, and the wavelength of the X-ray photons. The fact that this refractive index is less than unity imply that there exits a critical incidence angle below which there is total reflectivity. For larger angles, the X-rays partially penetrate the surface.

For neutron reflectivity the idea is similar. A refractive index for neutrons, related to the scattering length density, which is involved in the neutron-nuclei interaction, and with the magnetic moments distribution in the sample, also involved in the magnetic interaction with the neutron spin, can be built. However, the magnetic part of the refraction index can change its sign depending on the relative orientation of the magnetic moments of the material with the neutron beam polarization.

After the discovery of Giant Magneto Resistance effect, the neutron reflectivity techniques have been widely employed to study interlayer AF exchange coupling in magnetic superlattices, which are the base of different spintronic devices. Usually these multilayers are characterized from magnetic hysteresis measurements done with MOKE, SQUID, or VSM magnetometry experiments. However, these macroscopic characterization techniques do not unveil the angle between adjacent ferromagnetic layers nor the magnetic correlation in the perpendicular direction or the domain size distributions. These parameters are at the origin of poor transport properties in these systems and can be understood after Polarized Neutron Reflectivity (PNR) experiments [156].

As a pioneer work, V. Lauter *et al.* [157] studied with PNR techniques the archetypical Fe/Cr multilayers, which have a strong AF interlayer exchange coupling and in-plane uniaxial anisotropy, to shed light on the role of the different ingredients, such as, spin configurations in the flopped phase, role of the anisotropy, border effects, etc...

These authors determined unambiguously the magnetic structure of each ferromagnetic layer n (with $1 \leq n \leq 12$) in $[^{57}\mathrm{Fe}(67\ \text{Å})/\mathrm{Cr}(9\ \text{Å})]_{12}$, at the spin-flop phase by applying a magnetic field along the the easy axis. The magnetic structure broke down into lateral domains, with a mean size of 2800 Å, deviated each one an angle $\pm\phi_n$ respect the magnetic field direction. The sequence of angle deviations along each layer n fulfils $\pm\phi_n = \mp\phi_{13-n}$ and the angle at the end layers $\pm\phi_1 = \mp\phi_{12} = \pm 40^\circ$ is smaller than in the interior layers $\pm\phi_6 = \mp\phi_7 = \pm 63^\circ$, which is related to the fact that in the end layers there is one missing neighbor. The canting angle in the interior reaches the value of the canting angle in the bulk sample for the same magnetic field. The resulting configuration has no net perpendicular

component to the magnetic field and, therefore, it is stable. The splitting into lateral domains at each layer is interpreted as a minimization of the dipolar energy via demagnetization at each individual layer.

1.13 Conclusions

In this chapter, we showed the fundamentals of neutron scattering and discussed some contributions of neutron scattering to solve a huge variety of problems in the field of magnetism. After more than seventy years from the first neutron scattering experiment, these techniques are widely employed to characterize magnetic materials together with other complementary techniques. Moreover, after this long history, with new neutron sources, and in particular pulsed sources, one can expect that these techniques will experience a substantial improvement with the availability of higher neutron fluxes and lower backgrounds. The use of new optical systems, faster detectors, new techniques exploiting new physical phenomena, will allow all together the use of smaller samples, to design new experiments, or to do faster *in operando* experiments, etc...

In the majority of the neutron sources, the experiments related to magnetism are the most demanded by the scientist and often the diffraction techniques (powder, single crystal and small angle) are the most requested with the goal to determine the evolution of some magnetic structure as a function of one or several parameters (temperature, magnetic field, pressure, concentration, etc...).

1.14 Acknowledgements

Much of the work reported here was carried out during funding by the Spanish Ministry of Science and Innovation grant PGC-2018-099024-B-I00 or its equivalents before. JC is grateful for the hospitality received at the different neutron sources and in particular to the Institut Laue-Langevin and the Laboratoire Leon Brillouin. We are indebted to many discussions with our colleagues and coworkers, but in particular with Fernando Palacio, Javier Luzón, Garry McIntyre, José Alberto Rodríguez-Velamazán, Ángel Millán, Oscar Fabelo, Laura Cañadillas, Juan Rodríguez-Carvajal, Katsuya Inoue, Yusuke Kousaka, Yuko Hosokoshi, Kazuki Ohishi, Jun Kishine, Yoshiiko Togawa, Cristina Sáenz de Pipaón, Clara González, Clara Rodríguez, Miguel Pardo-Sáenz, Milagros Tomás and Larry Falvello.

1.15 References

[1] C. Abel et al. *Physical Review Letters*, 124:081803, 2020.

[2] R. G. Newton. *Scattering Theory of Waves and Particles*. Dover Publications, Inc., Mineloa, New York, 2002.

[3] A. Galindo and P. Pascual. *Quantum Mechanics II*. Springer-Verlag, 1990.

[4] E. Fermi. *Ric. Sci.*, 7:13, 1936.

[5] J. Schwinger and E. Teller. *Physical Review*, 52:286, 1937.

[6] F. Bloch. *Physical Review*, 50:259, 1936.

[7] F. Bloch. *Physical Review*, 51:994, 1937.

[8] J. Schwinger. *Physical Review*, 51:544, 1937.

[9] L. Van Hove. *Physical Review*, 95:249, 1954.

[10] N. H. March and M. P. Tosi. *Introduction to liquid state physics*. World Scientific, Singapore, 2002.

[11] N. W. Ashcroft and N. David Mermin. *Solid State Physics*. Harcourt, Inc., 1976.

[12] O. Halpern and M. H. Johnson. *Physical Review*, 55:898, 1939.

[13] E. U. Condon and H. Odabasi. *Atomic Structure*. Cambridge University Press, 1980.

[14] S. W. Lovesey. *Theory of Neutron Scattering from Condensed Matter*, volume 2. Oxford University Press, Clarendon, Oxford, 1984.

[15] D. F. Johnston. *Proceedings of the Physical Society*, 88:37, 1966.

[16] B. Fultz. *Progress in Materials Science*, 55:247–352, 2010.

[17] F. Bloch. *Z. Phys. A*, 61:206–219, 1939.

[18] T. Holstein and H. Primakoff. *Physical Review*, 58:1098, 1940.

[19] S. V. Maleev. *Zh. Eksperim. i Teor. Fiz.*, 33:129, 1958.

[20] S. V. Maleev. *Zh. Eksperim. i Teor. Fiz.*, 40:1224, 1961.

[21] A. W. Saenz. *Physical Review*, 119:1542, 1960.

[22] Yu. A. Izyumov and S. V. Maleev. *Zh. Eksperim. i Teor. Fiz.*, 41:1644, 1961.

[23] Yu.A. Izyumov. *Usp. Fiz. Nauk.*, 80:41, 1963.

[24] M. Blume. *Physical Review*, 130:1670, 1963.

[25] M. Blume. *Physical Review*, 133:A1366, 1964.

[26] M R. I. Schermer and M. Blume. *Physical Review*, 166:554, 1968.

[27] V.G. Baryaktar S.V. Maleev and P.A. Suris. *Soviet Physics Solid State*, 4:2533, 1963.

[28] V. E. Naish Yu. A. Izyumov and R. P. Ozerov. CRC Press, Taylor & Francis, New York, 1991.

[29] H. M. Rietveld. *Appl. Crystallogr.*, 2:65–71, 1969.

[30] R. A.Young, M.P. Eackie, and R. B. Von Dreele. *Applied Crystallography*, 10:262–9, 1977.

[31] G. Malmros and J.O. Thomas. *Applied Crystallography*, 10:7–11, 1977.

[32] J.B. Hastings D. E. Cox, W. Thomlinson, and C. T. Prewill. *Nuclear Instruments and Methods*, 208:573–8, 1983.

[33] R. A. Young, editor. *The Rietveld method*. Oxford University Press, 1993.

[34] W. I. F. David, K. Shankland, M. L. B, and B. CH, editors. *Structure Determination From Powder Diffraction Data*. Oxford Science Publication, 2002.

[35] J. A. Rodríguez-Velamazán, O. Fabelo, A. Millán, J. Campo, R. D. Johnson, and L. Chapon. *Scientific Reports*, 5:14475, 2015.

[36] L. Desgranges, G. Baldinozzi, G. Rousseau, J.C. Niepce, and G. Calvarin. *Inorganic Chemistry*, 48:7585–7592, 2009.

[37] M. T. Hutchings, P. J. Withers, T. M. Holden, and T. Lorentzen. CRC Press, Taylor & Francis, London, 2005.

[38] C. G. Shull and J. Samuel Smart. *Phys. Rev*, page 1257, 1949.

[39] R. L. Carlin and F. Palacio. *Coordination Chemistry Reviews*, 65:141, 1985.

[40] J.A. Puértolas, R. Navarro, F. Palacio, J. Bartolomé, D. González, and R.L. Carlin. *Physical Review B*, 31(1):516–526, 1985.

[41] F. Palacio, A. Paduan-Filho, and R.L. Carlin. *Physical Review B*, 21(1):296–298, 1980.

[42] Yoseph Imry and Shang-keng Ma. *Physical Review Letters*, 35:1399, 1975.

[43] S. Fishman and A. Aharony. *Journal of Physics C: Solid State Physics*, 12(18):L729–L733, 1979.

[44] F. Palacio, J. Campo, M. C. Morón, A. Paduan, and C. C. Becerra. *International Journal Of Modern Physics B*, 12(18):1781–1793, 1998.

[45] F. Palacio, M. Gabas, J. Campo, C.C. Becerra, A. Paduan-Filho, and V. B. Barbeta. *Physical Review B*, 56(6):3196, 1997.

[46] C.C. Becerra, V. B. Barbeta, A. Paduan-Filho, F. Palacio, J. Campo, and M. Gabás. *Physical Review B*, 56(6):3204, 1997.

[47] J. Campo, F. Palacio, M.C. Moron, C.C. Becerra, and A. Paduan. *Journal of Physics; Condensed Matter*, 11(22):4409–4425, 1999.

[48] C.C. Becerra, V.B. Barbeta, A. Paduan, F. Palacio, J. Campo, and M. Gabás. *Physical Review B*, 56(6):3204–3211, 1997.

[49] M. Gabas, F. Palacio, J. Rodríguez Carvajal, and D. Visser. *Journal of Physics Condensed Matter*, 7:4725, 1995.

[50] A. Jain, S. M. Yusuf, J. Campo, and L. Keller. *Physical Review B*, 79(18):184428, 2009.

[51] Gwenaëlle Rousse, Juan Rodríguez-Carvajal, Calin Wurm, and Christian Masquelier. *Physical Review B*, 88(21):214433, 2013.

[52] F. Hulligur and E. Pobitschka. *Journal of Solid State Chemistry*, 1:117, 1970.

[53] S. S. P. Parkin and R. H. Friend. *Philosophical Magazine B*, 41:65, 1980.

[54] S. S. P. Parkin and R. H. Friend. *Philosophical Magazine B*, 41:95, 1980.

[55] Y. Togawa, T. Koyama, K. Takayanagi, S. Mori, Y. Kousaka, J. Akimitsu, S. Nishihara, K. Inoue, A. Ovchinnikov, and J. Kishine. *Physical Review Letters*, 108(10):107202, 2012.

[56] Victor Laliena, Javier Campo, Jun-Ichiro Kishine, Alexander S Ovchinnikov, Yoshihiko Togawa, Yusuke Kousaka, and Katsuya Inoue. *Physical Review B*, 93(13):1420, 2016.

[57] Victor Laliena, Javier Campo, and Yusuke Kousaka. *Physical Review B*, 95(22):1420, 2017.

[58] Victor Laliena, Yusuke Kato, Germán Albalate, and Javier Campo. *Physical Review B*, 98(14):144445, 2018.

[59] Victor Laliena, Javier Campo, and Yusuke Kousaka. *Physical Review B*, 94(9):960, 2016.

[60] B. van Laar, H. M. Rietveld, and D. J. W. Ijdo. *Journal of Solid State Chemistry*, 3:154, 1971.

[61] Y. Kousaka, T. Ogura, J. Zhang, P. Miao, S. Lee, S. Torii, T. Kamiyama, J. Campo, K. Inoue, and J. Akimitsu. *Journal of Physics: Conference Series*, 746:012061, 2016.

[62] Curie P. *J. Physique*, 3(III):393–415, 1894.

[63] T. Kimura, T. Goto, H. Shintani, K. Ishizaka, T. Arima, and Y. Tokura. *Nature*, 426(6962):55–58, 2003.

[64] R. Kajimoto, H. Yoshizawa, H. Shintani, T. Kimura, and Y. Tokura. *Physical Review B*, 70(1):916, 2004.

[65] T. Kimura, G. Lawes, T. Goto, Y. Tokura, and A. P. Ramirez. *Physical Review B*, 71(22):415, 2005.

[66] M. Kenzelmann, A.B. Harris, S. Jonas, C. Broholm, J. Schefer, S.B. Kim, C.L. Zhang, S.W. Cheong, O.P. Vajk, and J.W. Lynn. *Physical Review Letters*, 95(8):87206, 2005.

[67] M. Ackermann, D. Brüning, T. Lorenz, P. Becker, and L. Bohat. *New Journal of Physics*, 15:123001, 2013.

[68] José Alberto Rodríguez-Velamazán, Oscar Fabelo, Angel Millan, Javier Campo, Roger D Johnson, and Laurent Chapon. *Scientific Reports*, 5:14475, 2015.

[69] W. Tian, H. Cao, J. Wang, F. Ye, M. Matsuda, J. Q. Yan, Y. Liu, V. O. Garlea, H. K. Agrawal, B. C. Chakoumakos, B. C. Sales, R. S. Fishman, and J. A. Fernández-Baca. *Physical Review B*, 94:214405, 2016.

[70] J. Campo, F. Palacio, A. Paduan-Filho, C. C. Becerra, M. T. Fernández Díaz, and J. Rodríguez Carvajal. *Physica B*, 234:622, 1997.

[71] J. A. Rodríguez-Velamazán, O. Fabelo, J. Campo, A. Millán, J. Rodríguez-Carvajal, and L. C. Chapon. *Physical Review B*, 95:174439, 2017.

[72] R. Sessoli, D. Gatteschi, A. Caneschi, and M. A. Novak. *Nature (london)*, 365:141, 1993.

[73] D. Gatteschi, A. Caneschi, L. Pardi, and R. Sessoli. *Science*, 265:1054, 1994.

[74] F. Luis, J. Bartolomé, J. Fernández, J. Tejada, J. Hernández, X. Zhang, and R. Ziolo. *Physical Review B*, 55:11449, 1997.

[75] J. Hernádez, X. Zhang, F. Luis, J. Bartolomé, J. Tejada, and R. Ziolo. *Europhysics Letters*, 35:301, 1996.

[76] L. Thomas, F. Lionti, R. Ballou, D. Gatteschi, R. Sessoli, and B. Barbara. *Nature (London)*, 383:145, 1996.

[77] J.R. Friedman, M.P. Sarachik, J. Tejada, and R. Ziolo. *Physical Review Letters*, 76:3830, 1996.

[78] T. Lis. *Acta Crystallographica. Section B*, 36:2042, 1980.

[79] R. A. Robinson, P. J. Brown, D. N. Argyriou, D. N. Hendrickson, and S. M. J. Aubin. *Journal of Physics: Condensed Matter*, 12(12):2805–2810, 2000.

[80] J. Fernández and J. Alonso. *Physical Review B*, 62:53, 2000.

[81] F. Luis, J. Campo, J. Gómez, G. J. McIntyre, J. Luzón, and D. Ruiz-Molina. *Physical Review Letters*, 95:227202, 2005.

[82] K. Inoue, K. Kikuchi, and M.Ohba. *Angewandte Chemie*, 42:4810–4813, 2003.

[83] H. Higashikawa, K. Okuda, J. Kishine, N. Masuhara, and K. Inoue. *Chemical Letters*, 36:1022–1023, 2007.

[84] C. González, J. Campo, F. Palacio, G.J. McIntyre, Y. Yoshida, K. Inoue, and K. Kikuchi. *submitted for publication*, 2020.

[85] Y. Yoshida, K. Inoue, K. Kikuchi, and M Kurmoo. *Chemistry of Materials*, 28:7029–7038, 2016.

[86] R. M. Moon, T. Riste, and W. C. Koehler. *Physical Review*, 181:920, 1969.

[87] E. Ressouche, J. X. Boucherle, B. Gillon, P. Rey, and J. Schweizer. *Journal of the American Chemistry Society*, 115:3610, 1993.

[88] P. J. Brown, A. Capiomont, B. Gillon, and J. Schweizer. *Journal of Magnetism and Magnetic Materials*, 14:289, 1979.

[89] J. M. Rawson, A. J. Banister, and I. Lavender. *Advances on Heterocycle Chemistry*, 62:137, 1995.

[90] M. Kinoshita, P. Turek, M. Tamura, K. Nozawa, D. Shiomi, Y. Nakazawa, M. Ishikawa, M. Takahashi, K. Awaga, T. Inabe, and Y. Maruyama. *Chemical Letters*, 7:1225, 1991.

[91] F. Palacio, G. Antorrena, M. Castro, R. Burriel, J. M. Rawson, J. N. B. Smith, N. Bricklebank, J. Novoa, and C. Ritter. *Physical Review Letters*, 79:2336, 1997.

[92] J. Luzón, J. Campo, F. Palacio, G. J. McIntyre, J. M. Rawson, R. J. Less, C. M. Pask, A. Alberola, R. D. Farley, D. M. Murphy, and A. E. Goeta. *Physical Review B*, 81:144429, 2010.

[93] R. L. Carlin and R. Burriel. *Physical Review B*, 27:3012, 1983.

[94] T. Smith and S. A. Friedberg. *Physical Review*, 177:1012, 1969.

[95] M. Gabás, F. Palacio, J. Rodríguez-Carvajal, and D. Visser. *Journal of Physics: Condensed Matter*, 7:4725, 1995.

[96] J. Luzón, J. Campo, F. Palacio, G. J. McIntyre, and A. Millan. *Physical Review B*, 78:L279, 2008.

[97] R. Papoular and B. Gillon. *Europhysics Letters*, 13:429, 1990.

[98] J. B. Forsyth. In P. Becker, editor, *Electron and Magnetization Densities in Molecules and Crystals*, pages 791–819. Plenum Press, New York, 1980.

[99] B.E.F. Fender, B.N. Figgis, J.B. Forsyth, P.A. Reynolds, and E. Stevens. *Proceedings of Royal Society. London A*, 404:127, 1986.

[100] B.E.F. Fender, B.N. Figgis, and J.B. Forsyth. *Proceedings of Royal Society. London A*, 404:139, 1986.

[101] R.J. Deeth, B.N. Figgis, J.B. Forsyth, E.S. Kucharski, and P.A. Reynolds. *Proceedings of Royal Society. London A*, 421:153, 1989.

[102] B.N. Figgis, J.B. Forsyth, E.S. Kucharski, P.A. Reynolds, and F. Tasset. *Proceedings of Royal Society. London A*, 428:113, 1990.

[103] R.J. Deeth, B.N. Figgis, J.B. Forsyth, E.S. Kucharski, and P.A. Reynolds. *Proceedings of Royal Society. London A*, 436:417, 1992.

[104] B.N. Figgis and P.A. Reynolds. *Molecular Physics*, 80:1377, 1993.

[105] G.S. Chandler, B.N. Figgis, R.A. Phillips, P.A. Reynolds, R. Mason, and G.A. Willians. *Proceedings of Royal Society. London A*, 384:31, 1982.

[106] B.N. Figgis, P.A. Reynolds, and R. Mason. *Proceedings of Royal Society. London A*, 384:49, 1982.

[107] F.A. Wedgwood. *Proceedings of Royal Society. London A*, 349:447, 1976.

[108] P.J. Brown, B.N. Figgis, and P.A. Reynolds. *Journal of Physics: Condensed Matter*, 2:5297, 1990.

[109] B.N. Figgis, P.A. Reynolds, and R. Mason. *Inorganic Chemistry*, 23:1149, 1984.

[110] A. Gukasov and P. J. Brown. *Journal of Physics: Condensed Matter*, 14:8831, 2002.

[111] A. Gukasov, P. Rogl, P. Brown, M. Mihalik, and A. Menovsky. *Journal of Physics: Condensed Matter*, 14:8841, 2002.

[112] M Th Rekveldt. *Journal of Physics Colloques. C1*, 32:579, 1971.

[113] G. M. Drabkin, A. I. Okorokov, V. Runov, and V. Pisḿa. *Zh. Eksp. Teor.Fiz.*, 15:458, 1972.

[114] A I Okorokov and et al. *Zh. Eksp. Teor. Fiz.*, 69:590, 1975.

[115] F. Tasset. *Physica B*, 156-157:627, 1989.

[116] F. Tasset, P. J. Brown, E. Lelievre-Berna, T. Roberts, S. Pujol, J. Allibon, and E. Bourgeat-Lami. *Physica B*, 267-268:69, 1999.

[117] P.J. Brown, J. B. Forsyth, and F. Tasset. *Proceedings of the Royal Society, London A*, 442:147, 1993.

[118] F. Tasset. *Physica B*, 297:1, 2001.

[119] P. J. Brown. *Physica B*, 297:198, 2001.

[120] P. J. Brown, J. Crangle, K.-U. Neumann, J. G. Smith, and K. R. A. Ziebeck. *Journal of Physics: Condensed Matter*, 9:4729, 1997.

[121] P. J. Brown. *Physica B*, 14, 1993.

[122] A. J. Clune, J. Nam, M. Lee, K. D. Hughey, W. Tian, J. A. Fernández-Baca, R. S. Fishman, J. Singleton, J. H. Lee, and J. L. Musfeldt. *Npj Quantum Materials*, 1, 2019.

[123] J. A. Rodríguez-Velamazán, O. Fabelo, J. Campo, J. Rodríguez Carvajal, N. Qureshi, and L. C. Chapon. *Scientific Reports*, 8:10665, 2018.

[124] S. W. Lovesey, J. Fernández-Rodríguez, J. A. Blanco, and P. J.Brown. *Physical Review B*, 70:172414, 2004.

[125] S. W. Lovesey, E. Balcar, K. S. Knight, and J. Fernández. *Physics. Reports*, 411:233, 2005.

[126] S. Ji, C. Song, J. Koo, K.-B. Lee, Y. J. Park, J. Y. Kim, J. H. Park, H. J. Shin, J. S. Rhyee, and B. H. Oh. *Physical Review Letters*, 91:257205, 2003.

[127] J. Blanco, P. Brown, A. Stunault, K. Katsumata, F. Iga, and S. Michimura. *Physical Review B*, 73:212411, 2006.

[128] J. Fernández-Rodríguez, J. A. Blanco, P. J. Brown, K. Katsumata, A. Kikkawa, F. Iga, and S. Michimura. *Physical Review B*, 72:52407, 2005.

[129] B. K. Cho, J.S. Rhyee, J. Y. Kim, M. Emilia, and O. C. Canfield. *Journal of Applied Physics*, 97:10923, 2005.

[130] S. Mühlbauer, D. Honecker, E. A. Périgo, F. Bergner, S. Disch, A. Heinemann, S. Erokhin, D. Berkov, C. Leighton, M. R. Eskildsen, and A. Michels. *Review of Modern Physics*, 91:1174, 2019.

[131] S. Mühlbauer, B. Binz, F. Jonietz, Ch. Pfleiderer, A. Rosch, A. Neubauer, R Georgii, and P. Böni. *Science*, 323:915, 2009.

[132] W. Münzer, A. Neubauer, T. Adams, S. Mühlbauer, C. Franz, F. Jonietz, R. Georgii, P. Böni, B. Pedersen, M. Schmidt, A. Rosch, and Ch. Pfleiderer. *Physical Review B*, 81:41203R, 2010.

[133] X.Z. Yu, Y. Onose, N. Kanazawa, J.H. Park, J.H. Han, Y. Matsui, N. Nagaosa, and Y. Tokura. *Nature*, 465:901, 2010.

[134] C. Pappas, E. Lelievre-Berna, P. Falus, P. M. Bentley, E. Moskvin, S. Grigoriev, P. Fouquet, and B. Farago. *Physical Review Letters*, 102:197202, 2009.

[135] S. Seki, X. Z. Yu, S. Ishiwata, and Y. Tokura. *Science*, 336:198–201, 2012.

[136] A. N. Bogdanov and A. Hubert. *Journal of Magnetism and Magnetic Materials*, 138:255, 1994.

[137] A. N. Bogdanov and D. A. Yablonskii. *Sov. Phys. JETP*, 68:101, 1989.

[138] A. N. Bogdanov and A. Hubert. *Journal of Magnetism and Magnetic Materials*, 195:182–192, 1999.

[139] V. Laliena and J. Campo. *Physical Review B*, 96:1420, 2017.

[140] T. Nakajima, H. Oike, A. Kikkawa, E. P. Gilbert, N. Booth, K. Kakurai, Y. Taguchi, Y. Tokura, F. Kagawa, and T. h. Arima. *Science Advances*, 3:e1602562, 2017.

[141] T. Nakajima, Y. Inamura, T. Ito, K. Ohishi, H. Oike, F. Kagawa, A. Kikkawa, Y. Taguchi, K. Kakurai, Y. Tokura, and T.-H. Arima. *Physical Review B*, 98:014424, 2018.

[142] Javier Campo, Javier Luzon, Fernando Palacio, Garry McIntyre, Angel Millan, and Andrew Wildes. *Physical Review B*, 78(5):054415, 2008.

[143] R. Caciuffo, G. Amoretti, A. Murani, R. Sessoli, A. Caneschi, and D. Gatteschi. *Physical Review Letters*, 81(21):4744–4747, 1998.

[144] I. Mirebeau, M. Hennion, H. Casalta, H. Andres, H. U. Güdel, A. V. Irodova, and A. Caneschi. *Physical Review Letters*, 83:628, 1999.

[145] E.M. Chudnovsky and D.A. Garanin. *Physical Review Letters*, 87(18):187203, 2001.

[146] C. Carbonera, F. Luis, J. Campo, J. Sánchez-Marcos, A. Camón, J. Chaboy, D. Ruiz-Molina, I. Imaz, J. van Slageren, S. Dengler, and M. González. *Physical Review B*, 81(1):014427, 2010.

[147] M. Bée. Principles and Applications in Solid State Chemistry, Biology and Materials Science. IOP PUBLISHING LTD, 2020.

[148] J. Alberto Rodríguez-Velamazán, Miguel A. González, José A. Real, Miguel Castro, M. Carmen Muñoz, Ana B. Gaspar, R. Ohtani, M. Ohba, K. Yoneda, Y. Hijikata, N. Yanai, M. Mizuno, H. Ando, and S. Kitagawa. *Journal Of The American Chemical Society*, 134(11):5083–5089, 2012.

[149] F. Mezei. *Zeitschrift für Physik A Hadrons and nuclei*, 255(2):146–160, 1972.

[150] F. Mezei. *The principles of neutron spin echo. In: Mezei F. (eds) Neutron Spin Echo. Lecture Notes in Physics,*, volume 128. Springer Berlin Heidelberg, 1980.

[151] F. Mezei, C. Pappas, and T. Gutberlet. *Neutron Spin Echo Spectroscopy: Basics, Trends and Applications*. Lecture Notes in Physics. Springer Berlin Heidelberg, 2002.

[152] K. Weron. *Journal of Physics: Condensed Matter*, 3(46):9151–9162, 1991.

[153] R.M. Pickup, R. Cywinski, C. Pappas, B. Farago, and P. Fouquet. *Physical Review Letters*, 102(9):97202, 2009.

[154] G. P. Felcher, R. O. Hilleke, R. K. Crawford, J. Haumann, R. Kleb, and G. Ostrowski. *Review of Scientific Instruments*, 58(4):609–619, 1987.

[155] David L. Price and F. Fernandez-Alonso. *Neutron scattering: magnetic and quantum phenomena*. Experimental methods in the physical sciences. Academic Press, London, 2015.

[156] Hartmut Zabel. *Materials Today*, 9(1-2):42–49, 2006.

[157] V. Lauter-Pasyuk, H. J. Lauter, B. P. Toperverg, L. Romashev, and V. Ustinov. *Physical Review Letters*, 89(16):309, 2002.